Ph.D Thesis

Diameter-Controlled Chemical Vapor Deposition Growth of Single-Wall Carbon Nanotubes using the Mist Flow Method

（直径のコントロール可能の単層カーボンナノチューブを合成する

霧化流動化学気相成長法）

Yun SUN

孙 陨

Graduate School of Science

Department of Chemistry

Nagoya University

2013

Contents

III

Chapter 1: General Introduction

1.1 Carbon [1]

Carbon has been considered as one of the most interesting and significant elements, not only because it is the fourth most abundant element in the universe by mass, after hydrogen, helium and oxygen, but also for its properties as a solid and subsequently as a material. Within the periodic table, it is represented by the symbol **C** and its atomic number is 6. It is also a non-metallic, tetravalent element that presents several allotropes (Figure 1).

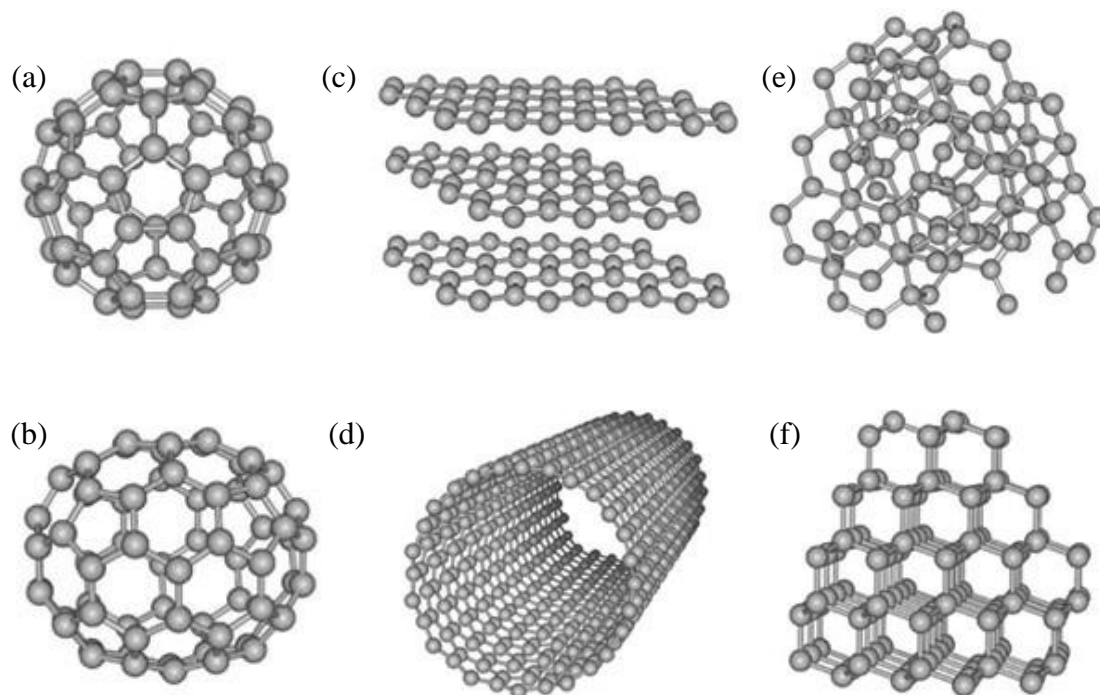Figure 1. Some allotropic structures of carbon: (a,b) fullerenes (C_{60} and C_{70}); (c) graphite; (d) carbon nanotube; (e) amorphous carbon; (f) nanodiamond [2].

What gives the abundant diversity of structural forms of solid carbon? Each carbon

atom has six electrons which occupy $1s^2$, $2s^2$ and $2p^2$ atomic orbitals. The $1s^2$ orbital contains two strongly bound electrons, and they are called core electrons. Four electrons occupy the $2s^2 2p^2$ orbitals, and they more weakly bound electrons are called valence electrons. In the crystalline phase the valence electrons give rise to $2s$, $2p_x$, $2p_y$ and $2p_z$ orbitals which are important in forming covalent bonds in carbon materials. In carbon, three possible hybridizations occur: sp, sp^2 and sp^3. Within sp^3 hybridization, four equivalent $2sp^3$ hybrid orbitals are tetrahedrally oriented around the atom (Figure 2a) and can form four equivalent σ bonds by an overlap with orbitals of other atoms. The carbon atom in methane (CH_4) provides a simple example of sp^3 hybridization through its tetragonal bonding to four nearest neighbor hydrogen atoms which have the maximum spatial separation from each other. In order to make elongated wavefunctions to these each direction, the $2s$ orbital and three $2p$ orbitals are mixed with each other resulting in the formation of an sp^3 hybridization.

Within sp^2 hybridization (Figure 2b), three equivalent $2sp^2$ orbitals are formed and one unhybridized $2p$ orbital is left. They are coplanar and oriented at $120\,°$ to each other and form σ bonds by an overlap with orbitals of neighbouring atoms as e.g. in ethane (C_2H_4). The remaining p orbitals on each carbon atom form a π bond by the overlap with the π orbital from the neighbouring carbon atom. Such bonds formed between two carbon atoms are represented as the double bond (C=C).

Within sp hybridization (Figure 2c), a linear combination of the $2s$ orbital and one of the $2p$ orbitals of a carbon atom is formed. For example, the acetylene is a simple carbon-based material showing sp hybridization. Linear σ bonds are formed by the overlap of the $2sp$ hydride orbitals of neighbouring atoms. Two π bonds are formed with the overlapping unhybridized π orbitals of the two carbon atoms. These bonds are

represented as the triple bond (C≡C), which is yielded by one σ bond and two π bonds.
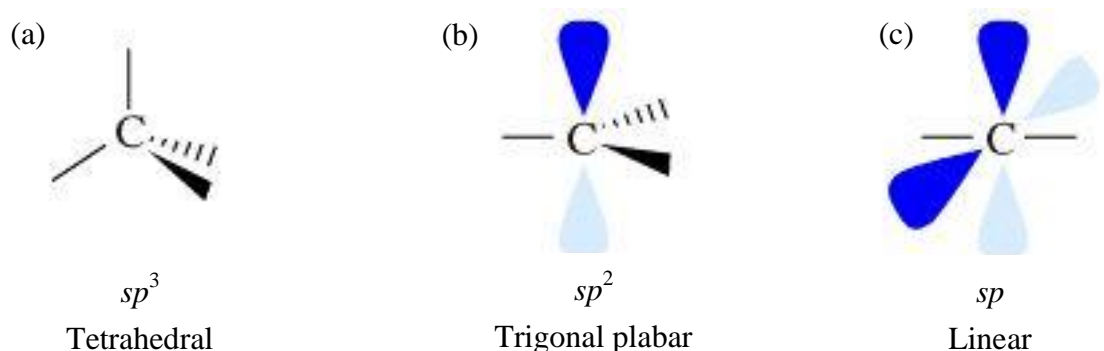
Figure 2. Three different hybridizations of carbon atom: (a) sp^3; (b) sp^2; (c) sp [3].

1.2 Diamond

Thanks to their gorgeous appearance and outstanding properties, the diamond being an attractive material is a metastable carbon polymorph at room temperature and atmospheric pressure and exists in a cubic and hexagonal form shown in Fig. 3. In the most frequent cubic form, each carbon atom is linked with four other carbon atoms by four sp^3 σ bonds in a tetrahedral array with a C–C bond length of 1.544 Å [4]. Its crystal structure is zinc blend type (fcc) with a diatomic basis, which is appropriately called the diamond cubic crystal structure. The second carbon atom is at position (¼, ¼, ¼) in the unit cell and the lattice constant is $a_0 = 3.567$ Å (Fig. 3a).
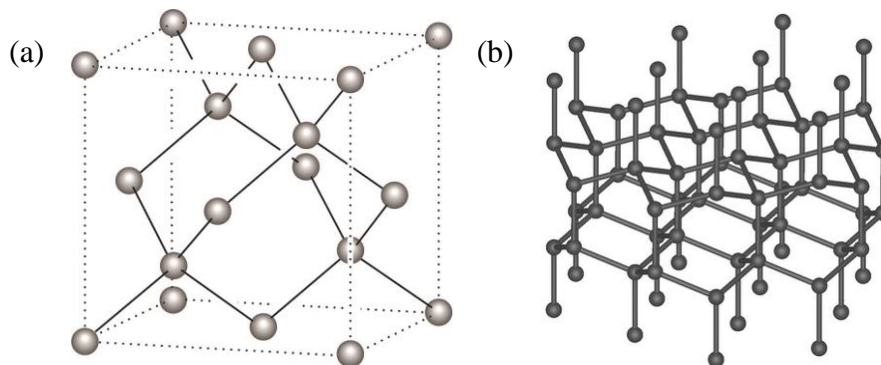
Figure 3. (a) Diamond in the cubic form and (b) the hexagonal Lonsdaleite [5].

The physical properties of diamond are dependent upon its structure. Diamond is a wide-gap semiconductor (5.47 eV), the hardest material in nature and has the highest atomic density. In addition, it has a quite low electrical conductivity and they were known as the best thermal conductors ($\sim$25 W cm^{-1} K^{-1}) before the discovery of CNTs. The hexagonal diamond (Lonsdaleite) has a wurtzite crystal structure and a C–C bond length of 1.52 Å [6]. The gravimetric density of both types of diamond is 3.52 g cm^{-3}.

1.3 Graphite

Another polymorph of carbon is graphite, whose crystal structure is distinctly different from that of diamond. In graphite the atoms are arranged in layers of a honeycomb network in which the carbon atoms are bonded with sp^2 σ bonds and a delocalized π bond. The weak interlayer bonding of graphite originates from the small overlap of the π-orbitals between atoms of adjacent layers and not to Van der Waals bonding [7]. Because of these weak inter-planar bonds, inter-planar cleavage is facile, which leads to the excellent lubricate properties of graphite. In addition, the electrical conductivity is relatively high in crystallographic directions parallel to the hexagonal sheets.

Graphite is commonly used as heating element for electric furnaces, electrode for arc welding, for high temperature crucibles, in casting molds for metal alloys and ceramics, for high temperature refractories and insulations in rocket nozzles, in chemical reactor vessels, for electrical contacts, brushes and resistors, as electrodes in the
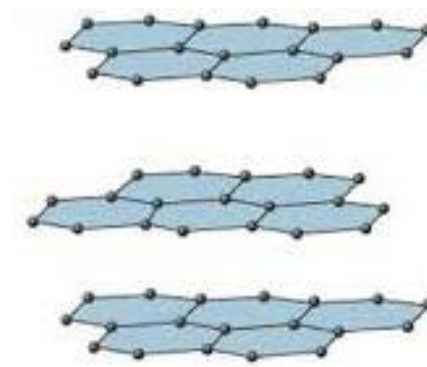
Figure 4. The structure of the graphite [8].

batteries and in air purification devices [9].

1.4 Fullerenes

Experimental and theoretical works have shown that the most stable form of carbon clusters form linear chains [10] up to about 10 atoms. For clusters that have 10 to 30 carbon atoms, the ring is the most stable structure [11]. Carbon clusters between 30 and 40 carbon atoms are unlikely and clusters above 40 atoms form cage structures, such as C_{60} (Figure 5), whose structure was identified by Kroto et al. in 1985 for the first time [12]. The carbon atoms are located at the 60 vertices of a truncated icosahedron that has 90 edges and 32 faces of which 12 are pentagons and 20 hexagons, consistent with Euler's theorem for polyhedra:

$$f + v = e + 2 \qquad (1)$$

where f, v and e are the number of faces, vertices, and edges of the polyhedra. The average distance of the nearest neighbouring C–C bond is 1.44 Å, almost equal to that in graphite. Each carbon atom is triangularly bonded to three other carbon atoms in an sp^2-derived bonding configuration. The curvature of the trigonal bonds in C_{60} leads to some admixture of sp^3 bonding, characteristic for tetrahedrally bonded diamond, but absent in graphite [13].
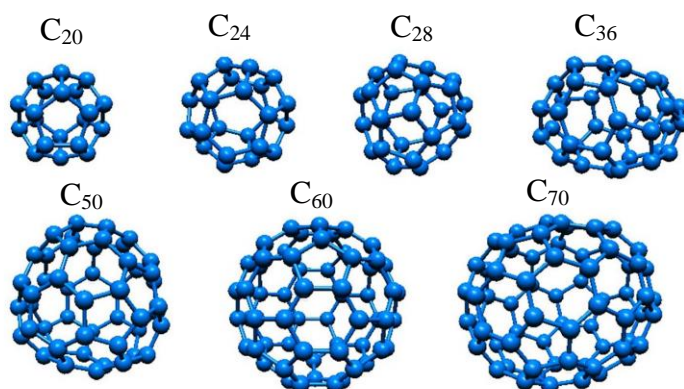
Figure 5. A series of fullerenes (C_{20}, C_{24}, C_{28}, C_{36}, C_{50}, C_{60} and C_{70}).

1.5 Carbon Nanotube

1.5.1 Discovery

Nowadays, as one of the most extraordinary carbon materials, carbon nanotubes (CNTs), one allotrope of carbon with cylindrical nanostructure, had made a great impact on the most areas of science and engineering due to their unprecedented physical and chemical properties since their discovery by Iijima [14] around 22 years ago. In 1991, some tiny tubes of pure carbon had been found in the soot when Iijima tried to fabricate high yield of C_{60} fullerenes with arc discharge. These tubular materials were hollow with many layers-tubes inside tubes and their ends were sealed with some conical caps.
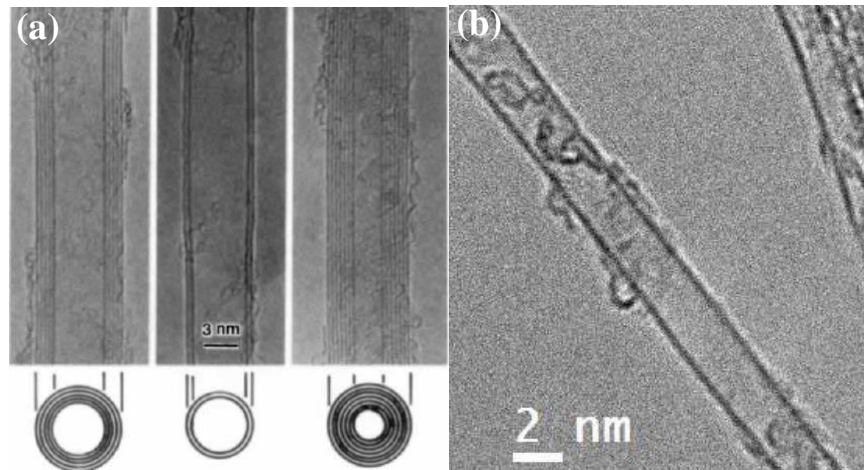
Figure 6. (a) High resolution transmission electron microscopy (HRTEM) images of the first observed MWCNTs by Iijima in 1991 [14] and (b) the individual SWCNT of my own sample.

These are the multi-walled carbon nanotubes (MWCNTs) we called right now (Figure 6a). Then in 1993, single-walled carbon nanotubes (SWCNTs) (Figure 6b) came out with the help of using the cobalt as the catalyst in an arc discharge system [15]. From that time, the family of CNTs had come into our sight officially. In addition, no previous

material has displayed the combination of superlative mechanical, thermal and electronic properties attributed to CNTs, which are available for nanotechnology, electronics, optics and other fields of material science and technology. These properties make nanotubes ideal, not only for a wide range of applications [16], but also as the tester for fundamental science [17]. CNTs can have diameters ranging from 1~100 nm and lengths up to millimeters [18]. Their densities can be as low as ~1.3 g/cm^3 and their Young's modulus are superior to all carbon fibers with values greater than 1 TPa [19].

1.5.2 Classification of Carbon Nanotube

Usually CNTs are categorized as single-walled, double-walled and multi-walled according to the number of concentric tubes. SWCNTs consist of a single sheet of graphene rolled up to form a cylinder with the diameter of 0.7~10 nm and length up to millimeters, though the diameter of most observed SWCNTs are less than 2 nm [1]. Double-walled carbon nanotubes (DWCNTs), formed by two concentric single-wall behave similarly to SWCNTs but they have unique properties and are suitable for some special applications. MWCNTs consist of an array of such cylinders formed concentrically and separated around 0.35 nm, a value similar to the basal plane separation in graphite [14]. The diameter of MWCNTs can distribute from 2 to 100 nm and lengths up to millimeters. Another way to classify CNTs is how the graphene sheet is rolled up. The rolling action breaks the symmetry of the planar system and imposes a distinct direction with respect to the hexagonal lattice and the axial direction. Depending on the relationship between this axial direction and the unit vectors describing the hexagonal lattice, CNTs can be metallic or semiconducting.

As shown in Fig. 7a, because an individual SWCNT can be considered as hollow

cylinders rolled up from one atomic-layer thick grapheme, each carbon atom in graphene can be identified with a pair of integers (n, m) and a pair of basis vectors ($\boldsymbol{a_1}$, $\boldsymbol{a_2}$), together with the initial and final carbon atoms, lead to the definition of a "chiral vector":

$$\boldsymbol{C}_h = n\boldsymbol{a_1} + m\boldsymbol{a_2} \tag{2}$$

When the graphene is rolled up, whether the resulting SWCNTs are metallic or semiconducting depends on the starting and end points of the chiral vector in the sp^2-bonded carbon atom lattice. SWCNTs with the chiral vector $\boldsymbol{C}_h = n\boldsymbol{a_1} + m\boldsymbol{a_2}$ are metallic when $|n - m| = 3j$, where j is an integer, otherwise semiconducting with geometry-dependent band gaps. Special classes of CNTs are the so-called "armchair" nanotubes (n, n) and the "zigzag" nanotubes $(n, 0)$. All the others are "chiral" nanotubes (n, m) with $n \neq m$ and $m \neq 0$ (Fig. 7b-c). Consequently, when CNTs are formed with random values of n and m, we would expect that two-thirds of them would be semiconducting, while the other third would be metallic [15]. As a matter of fact, a CNT can be also characterized by its diameter d_t and the chiral angle θ ($0 \leq |\theta| \leq 30°$), which is the angle between the chiral vector $\boldsymbol{C}_h$ and the zigzag direction $(n, 0)$. The integers (n, m) determine d_t and θ:

$$d_t = \frac{a}{\pi}\sqrt{n^2 + m^2 + nm}, \qquad \sin\theta = \frac{\sqrt{3}m}{2\sqrt{n^2 + m^2 + nm}} \tag{3}$$

In addition, SWCNTs are often found in bundles formed by a triangular arrangement of some individual SWCNTs, which are held together by week Van der Waals forces. The electronic structure of CNTs is intensively dependent on their diameter and chirality.
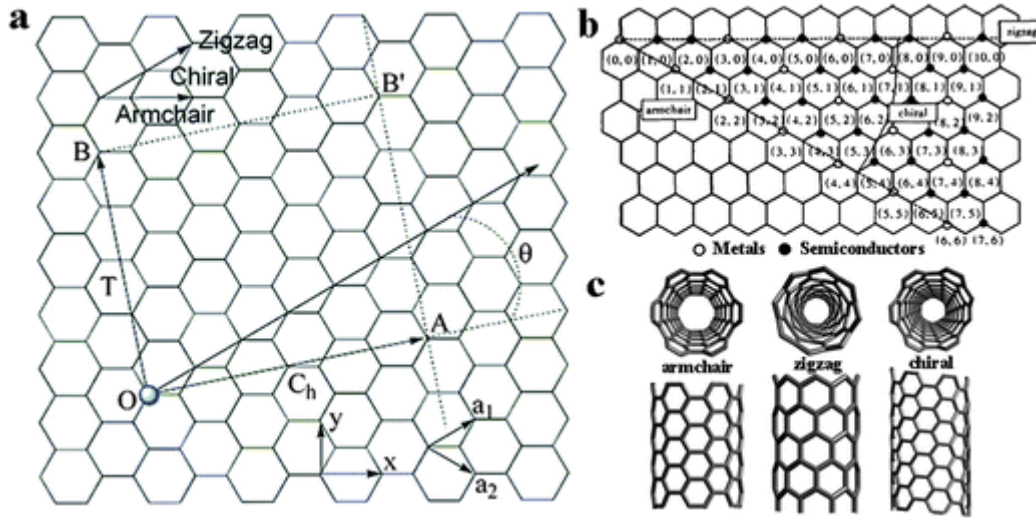
Figure 7. (a) Schematic plot of the chiral vector (C_h) in a graphene 2D lattice. (b) The relationship between integers (n, m) and the metallic or semiconducting nature of nanotubes. (c) The structure of "armchair", "zigzag" and "chiral" nanotubes [20].

1.5.3 Synthesis of Carbon Nanotubes

1.5.3.1 Arc discharge

The arc discharge method is historically the first one of synthesizing CNTs. In arc discharge system (Figure 8a), carbon atoms are evaporated by the plasma of helium gas ignited by high currents passed through opposing two graphitic rods: carbon anode and cathode. The temperature involved is close to the melting point of graphite: 3000 ~ 4000℃. The anode evaporates to form fullerenes and CNTs which are deposited in the form of soot all around the chamber walls. A small part of the evaporated material originating from the graphitic rods is also deposited in the cathode substrate which is composed of a variety of carbon products including soot, fullerenes and MWCNTs [21]. For the growth of SWCNTs, a kind of metal catalyst, such as Ni, Co and Fe, needs to be impregnated in the graphitic anode material but leaving the cathode as the pure graphite. A hydrocarbon gas introduced into the arc discharge is more favorable to yield CNTs

than fullerenes because of the high temperature and high activity of the formed hydrogen [22]. The first success in synthesizing high yield of SWCNTs by arc discharge was achieved by Bethune and co-workers in 1993. A carbon anode containing a small percentage of cobalt catalysts had been utilized in the arc discharge experiment and the abundant as-grown SWCNTs were found in the soot material [23]. MWCNTs can be obtained by tuning the parameters such as the pressure of inert gas in the discharge chamber and the acting current. The as-grown MWCNTs by arc discharge are very straight, indicative of their high crystallinity with few defects on the sidewalls of nanotubes.

1.5.3.2 High temperature laser ablation

In 1996, another method for producing CNTs called laser ablation was introduced (Figure 8b) [24]. It consists of a laser to ablate a block of pure graphite, and later graphite mixed with the metal catalysts [25], such as Co, Nb, Pt, Ni, Cu, or a binary combination thereof. The laser not only converts the composite solid material into small aggregates which can only recombine if placed in an external furnace [26] but also is used to form a carbon vapor from a graphite rod. During laser ablation, an inert carrier gas (helium or argon) carries the carbon vapor from the 1200℃ graphite rod to a water-cooled collector downstream where the carbon vapor recondenses to form predominant SWCNTs. The as-grown SWCNTs are almost in the form of ropes consisting of dozens of individual SWCNTs close-packed into hexagonal forms via Van der Waals interaction.

According to the difference of the applied laser, two kinds of methods were developed: a pulsed laser [27-28] and a continuous laser [29-30]. The main difference

between lasers is that the pulsed laser demands a much higher light intensity (100 kW/cm^2 compared with 12 W/cm^2). The pulsed laser method was originally developed by Smalley and co-workers for the production of fullerenes and CNTs [31-32]. The quantity of the materials formed in this method was so small that a structural identification by electron microscopy was not feasible unless the identification took place only by mass spectrometry [12]. But several advantages of the laser ablation method cannot be neglected including the easy formation of SWCNTs, diameter control, allowed research on the formation mechanism and the production of new material. The diameter of as-grown SWCNTs can be controlled by adjusting the temperature, catalyst composition and gas flow rate [33-34]. At higher temperatures, SWCNTs of larger diameters are produced. Equally, the introduction of a Ni-Y catalyst enlarges the nanotube diameter while applying a Rh-Pd catalyst reduces the diameter [35-36]. SWCNTs with minimal defects were synthesized using the PLV technique accompanied by purification processes [37-39]. Disadvantages of this method include the limited scale of SWCNT production. Although the structures are well crystallized, they often coexist with large amount of the contaminants, such as the catalytic particles and amorphous carbon.

The main differences compared to the arc discharge method are:

① The material is submitted to a laser ablation instead of an arc discharge;

② No tube of reasonable length has ever been synthesized without catalyzing particles. This implies that a certain local anisotropy is necessary to grow a nanotube;

③ Particles are collected through a carrier gas on a cool plate far from the target. A secondary heating is usually added.

In brief, the achievement in synthesizing SWCNTs by arc discharge and laser

ablation has led to the wide availability of samples used for studying fundamental physics in low dimensional materials and exploring their applications [40].
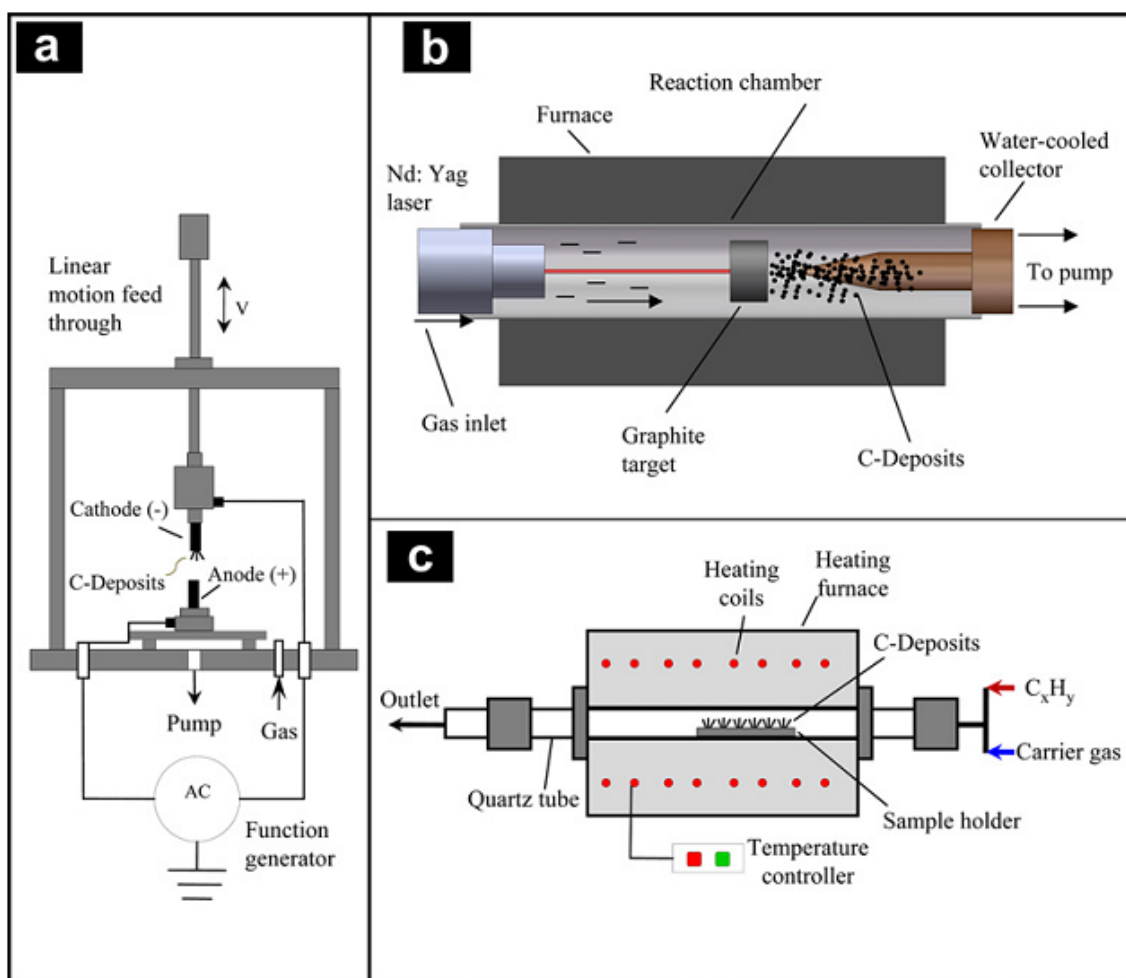
Figure 8. Methods currently applied for the synthesis of CNTs: (a) arc discharge; (b) high temperature laser ablation and (c) catalyst-supported CVD [21].

1.5.3.3 Chemical vapor deposition (CVD)

Chemical vapor deposition, usually called CVD for short, is the most popular for synthesizing CNTs with the high yield and high quality. The thermal decomposition of a hydrocarbon gas is achieved in the presence of the metal catalyst involved in the growth process. The type of hydrocarbon, the catalyst type and size and the reaction

temperature seem to be the key parameters in the CVD growth of CNTs. Compared with the arc discharge and laser ablation methods, CVD is a more simple and economic technique for synthesizing CNTs at low temperature and ambient pressure. Although the crystallinity of as-grown CNTs from arc discharge and laser ablation is superior to the as-grown ones from CVD, CVD is inevitably predominant in the yield and purity. Moreover, CVD is the best at the selective growth, such as diameter, chirality and structure. CVD is versatile in the sense that it offers harnessing plenty of hydrocarbons in any state (solid, liquid or gas), enables the use of various substrates and allows the growth of CNT in a variety of forms, such as powder, thin or thick films, aligned or entangled, straight or coiled nanotubes, or a desired architecture of nanotubes on the predefined sites of a patterned substrate. It also offers better control on the growth parameters.

Indeed, CVD synthesis of CNTs can be divided into two categories: one is using catalysts supported on substrates or embedded in porous inorganic materials and the other is a gas-phase growth (floating CVD) such as in HiPco, direct injection pyrolytic synthesis (DIPS) and aerosol process [41-42]. The former is suitable for the fabrication of on-tip devices such as nanotube transistors, while the latter is believed to be an ideal continuous process for the production of CNTs, especially SWCNTs on a commercial scale. Figure 8c shows a schematic of the experimental setup used for CNT growth by catalyst-supported CVD (CCVD) method. The process involves passing a hydrocarbon vapor (typically 15 ~ 60 min) through a reactor, where the substrate (silicon, silica, zeolite, etc.) coated with the catalysts was loaded, with the sufficiently desirable temperature (600 ~ 1200℃) to decompose the hydrocarbon and make the growth of CNTs. In the case of a liquid hydrocarbon (methanol, alcohol, etc.), the liquid is heated

or bubbled in a flask and one kind of carrier gas is introduced to carry the hydrocarbon vapor into the reactor to make CVD growth happen.

On the other hand, the gas-phase growth of SWCNTs is achieved by passing a mixed flow of organometallic catalyst precursors and carbon sources through a heated furnace reactor [43-46]. So it is a continuous process including both the formation of the catalyst particles and the subsequent growth of SWCNTs occurring in the same reactor. An actual picture and a scheme of the experimental apparatus of our own mist flow CVD are shown in Figure 9. Direct sampling of SWCNTs from the gaseous phase collected by any substrate loaded on the bottom of the quartz tube at room temperature eliminates the influence of the substrate.
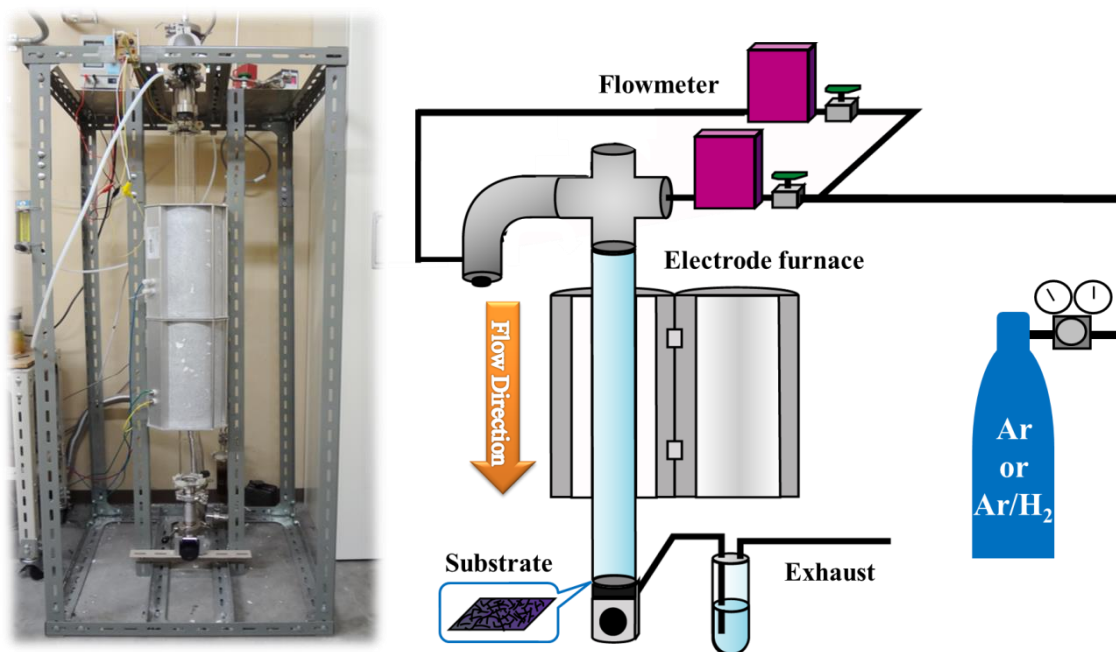
Figure 9. The actual picture of our own mist flow CVD apparatus (left) and the corresponding schematic diagram (right).

Nowadays, there have been a few theories about the accurate CVD growth

mechanism for CNTs and one of them is widely accepted. As shown in Fig. 10a [47], when the interaction between the catalyst and substrate is weak (the metal has an acute contact angle with the substrate), hydrocarbon decomposes on the top surface of the metal, carbon diffuses down through the metal, and CNT precipitates out across the metal bottom, pushing the whole metal particle off the substrate (described as step (i)). Since the top of the metal is open for the fresh hydrocarbon decomposition (the concentration gradient exists in the metal allowing carbon diffusion), CNT continues to grow longer and longer (ii). Once the metal is fully covered with the excess carbon, its catalytic activity ceases and the CNT growth is terminated (iii). This is known as "tip-growth mode" [48].

Figure 10. Widely accepted CVD growth mechanisms for CNTs: (a) tip-growth mode and (b) base-growth mode [47].

On the other hand (Fig. 10(b)), when the interaction between the catalyst and substrate is strong (the metal has an obtuse contact angle with the substrate), the initial

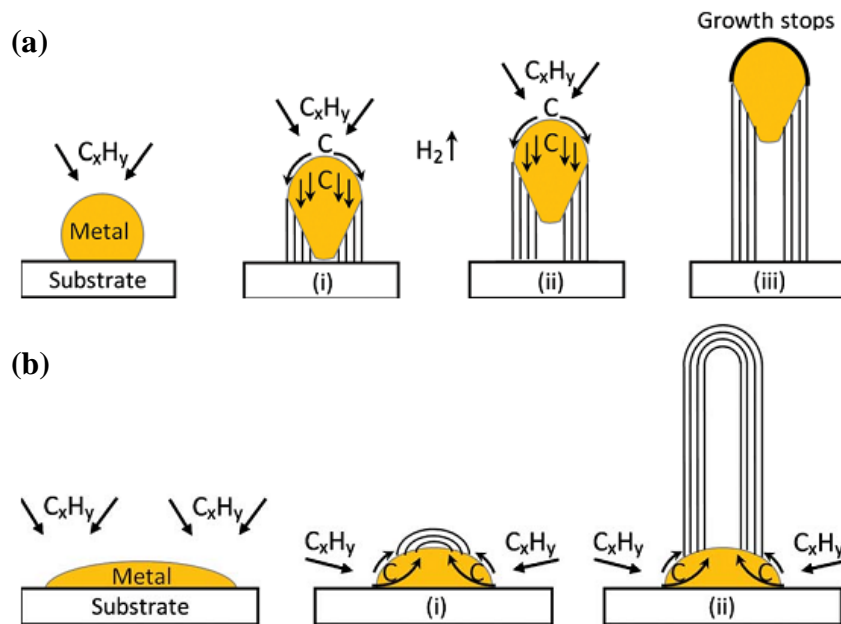hydrocarbon decomposition and carbon diffusion take place similar to that in the tip-growth case, but the precipitation of CNT fails to push the metal particle up so that the precipitation is compelled to emerge out from the metal's apex (farthest from the substrate, having minimum interaction with the substrate). Firstly, carbon crystallizes out as a hemispherical dome (the most favorable closed-carbon network on a spherical nanoparticle) which then extends up in the form of seamless graphitic cylinder. Subsequent hydrocarbon deposition takes place on the lower peripheral surface of the metal, and as dissolved carbon diffuses upward. Thus CNT grows up with the catalyst particle rooted on its base; hence, this is known as "base-growth model" [49]. Generally speaking, Fe, Ni and Co are usually selected as the catalyst precursor because of their phase diagrams for the metal and carbon. At high temperatures, carbon has fine solubility in these metals, which leads to the formation of metal-carbon solutions and therefore the aforementioned growth mechanism.

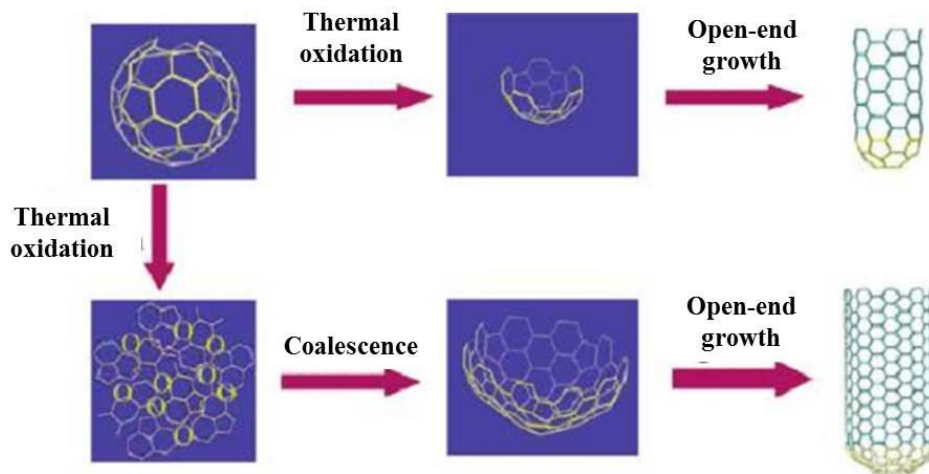Figure 11. Proposed mechanism of CVD growth of SWCNTs using thermally opened C_{60} caps [56].

Furthermore, there is another case. As the development of CVD technique, the catalyst-free synthesis of SWCNTs is very attractive because the catalyst particles

(metals or nonmetals) and the catalyst material can contaminate the tubes and affect their intrinsic properties [50-51]. To this end, various all-carbon routes have been developed, for example, SWCNTs grown from diamonds [52] and cloning open-ended SWCNT seed pieces [53-54]. At present, using opened fullerenes as nucleation sites for CVD growth of SCWNTs has been paid so much attention [55-56]. Its growth mechanism has pointed out an inspiration for CVD growth of all-carbon SWCNTs (Figure 11).

1.5.4 Properties and applications of carbon nanotubes

CNTs have exhibited remarkable properties which are associated with their unique structure, high aspect ratio, and quantum size effects. In recent years, a number of theoretical and experimental works have been devoted to study the properties of CNTs. The superior properties of CNTs classify them as the material of the 21st century.

① Mechanical properties. CNTs are the strongest and hardest materials yet discovered in terms of tensile strength and elastic modulus respectively. Their stiffness is comparable to that of diamond and they possess an estimated tensile strength of 200 GP, which is one hundred times higher than the value displayed by steel while weighing six times less. This strength results from the covalent sp^2 bonds formed between the individual carbon atoms. In addition, knowledge of the Young's modulus (E) of a material is the first step towards its use as a structural element for various applications [57]. CNTs also have a very large Young modulus in their axial direction. And even though Young's modulus decreases as the increase of disorders, their resistance can still remain very high.

② Thermal properties. CNTs have been considered to be the very good thermal

conductors along the tube, exhibiting a property known as "ballistic conduction", but good insulators laterally to the tube axis. It is predicted that carbon nanotubes will be able to transmit up to 6000 $W \cdot m^{-1} \cdot K^{-1}$ at room temperature. On the other hand, copper is a well-known metal for its good thermal conductivity but it can only transmit up to 385 $W \cdot m^{-1} \cdot K^{-1}$ by contrast [58]. The thermal stability of CNTs can be evaluated using thermal gravimetric analysis (TGA). CNTs are more stable to the oxidation than the activated carbon, but more reactive than graphite [59]. SWCNTs are found to be more stable than MWCNTs because of the changes associated with their surfaces [60].

③ The electrical properties of CNTs depend on how the hexagons are orientated along the axis of the tube. Because of the symmetry and unique electronic structure of graphene, the structure of a nanotube strongly affects its electrical properties. As previous discussed, a (n, m) nanotube is metallic when $n = m$ or $(n - m) = 3i$, where i is an integer; if $n - m$ is a multiple of 3, then the nanotube is semiconducting with a very small band gap. In theory, metallic nanotubes can carry an electric current density of 4×109 A/cm^2, which is more than a thousand times greater than those of metals such as copper [61].

④ Optical properties of CNTs derive from electronic transitions within one dimensional density of states (DOS). The sharp peaks found in one-dimensional materials are called Van Hove singularities (vHs). As a result, owing to the unique DOS, SWCNTs exhibit the unique optical properties. As shown in Figure 12, there are many sharp peaks at different energies (vHs of SWCNTs) within metallic and semiconducting SWCNTs, respectively. The optical properties of SWCNTs, such as absorption, resonance Raman spectroscopy and photoluminescence [62-65],

depend on the electronic transition between pairs of these vHs in the valence and conductance bands; the transition energy is described as E_{ii} (i = 1, 2, 3 …; vHs number from the Fermi level). Moreover, in 1999, Kataura *et al*. had introduced a plot of this E_{ii} as a function of d_t (the diameter of SWCNTs) – Kataura plot, from which some optical properties of SWCNTs have been well comprehended (Figure 13) [66].

Abundant potential applications of CNTs consist of nanoconductors and nanoswitches, nanomechanical devices, composites with unique mechanical and electromagnetic properties that can be used as field emission tips [68-71], storage of hydrogen and natural gas [4,13], electromechanical sensors [72], as electrodes in electrochemical capacitors [73-74], important components in batteries [75], fuel cell devices [76-77] and so on. CNTs have thermal, electrical, and mechanical properties that are extraordinarily high compared to those materials that were thought to have reached the limits of these properties.
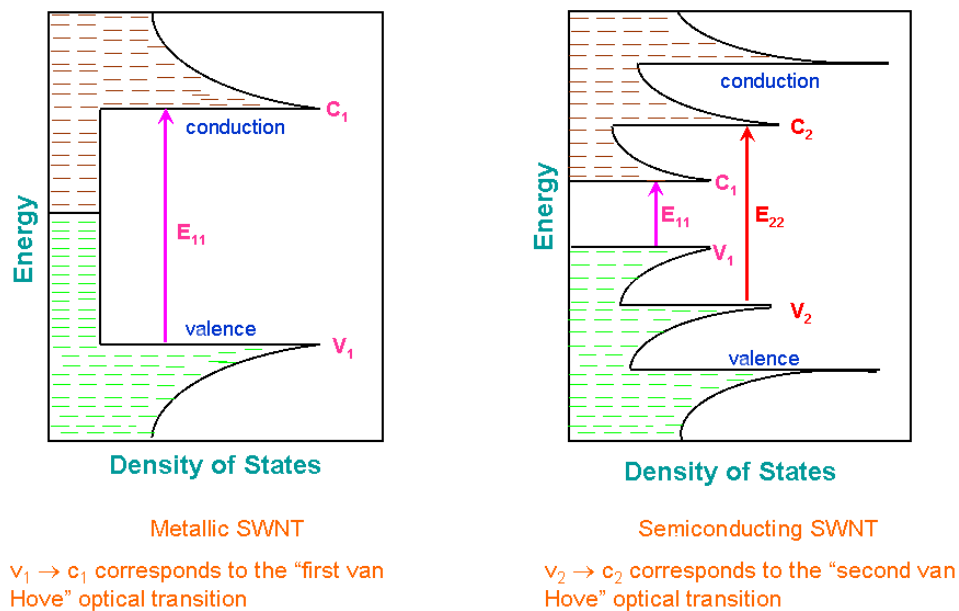

Figure 12. The DOS of metallic (left) and semiconducting (right) SWCNTs.
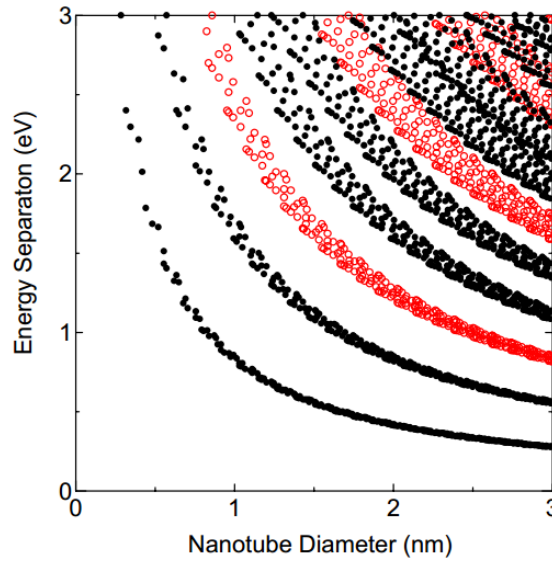
Figure 13. Relationship between the band-gap energy and the diameter of SWCNTs, called as Kataura plot. Red points are metallic SWCNTs and black points are semiconducting SWCNTs [67].

1.5.5 Characterization of Carbon Nanotubes

1.5.5.1 Raman spectroscopy [78]

Raman spectroscopy (the inelastic scattering of a photon) is one of the most useful and powerful techniques to characterize CNTs in order to obtain the initial information about their structure and chirality. The laser light interacts with molecular vibrations, phonons or other excitations in the system, resulting in the energy of the laser photons being shifted up or down. The shift in energy gives information about the vibrational modes in the system. Each part of the Raman spectrum, the radial breathing mode (RBM), the disorder mode (D mode) and the G mode (around 1500 ~ 1700 cm^{-1}), can be used to access different properties of SWCNTs.

The RBM features correspond to the coherent vibration of the C atoms in the radial direction, as if the tubes were "breathing". It can be used to study the nanotube diameter (d_t) through its frequency (ω_{RBM}) and to perform an (*n, m*) assignment of an individual

SWCNT. These features are unique to CNTs and occur with frequencies between 120 and 350 cm^{-1} for SWCNTs. These RBM frequencies are therefore very useful for identifying whether a given carbon material contains SWCNTs, through the presence of RBM modes and for characterizing the diameter distribution in the sample with the help of the relation: $d_t = 248/\omega_{RBM}$ for isolated SWCNTs on an oxidized Si substrate [79-80]. In addition, it is noticeable that the RBM features measured by only one laser line cannot supply an integrate characterization of the diameter distribution of the sample. Therefore, a good characterization of the diameter distribution in the samples can be obtained by applying many laser lines with Raman spectra as shown in Figure 14.
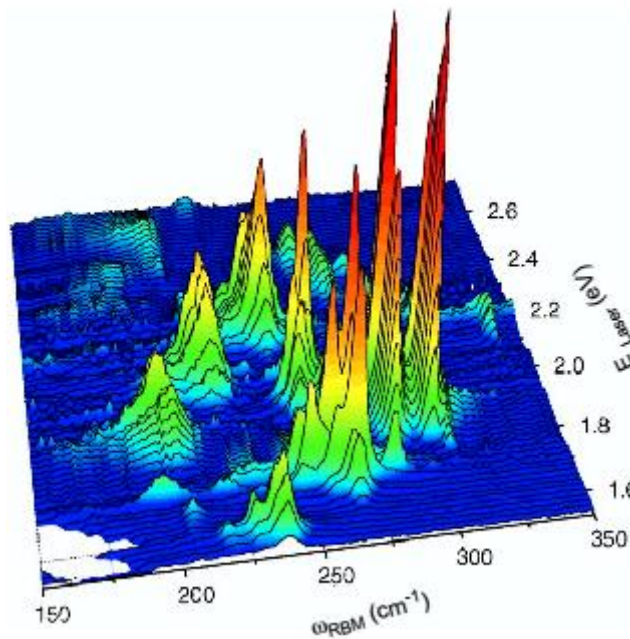

Figure 14. RBM resonance Raman measurement of HiPco CNTs wrapped in sodium dodecyl sulfate (SDS) and dispersed in an aqueous solution [81], measured with 76 different laser lines [82].

Another very important mode is the G mode (G from graphite). This mode corresponds to planar vibrations of carbon atoms and is present in most graphite-like

materials [83]. In SWCNTs, the G band is split into several peaks around 1580 cm^{-1}. The splitting pattern and intensity depend on the tube structure and excitation energy; not only can they be used for the diameter characterization of sample together with RBM mode within low frequency, but also to distinguish the tube is metallic or semiconducting according to the strong differences between the figuration of their Raman spectrum [84-85]. Moreover, the observed D mode is usually located between 1330 ~ 1360 cm^{-1} due to the defects involved in the tubes. So the ratio of the intensity of G and D modes (I_G/I_D) can be used to verify the quality of CNTs. This ratio gives an idea of the functionalization of a nanotube (Figure 15).
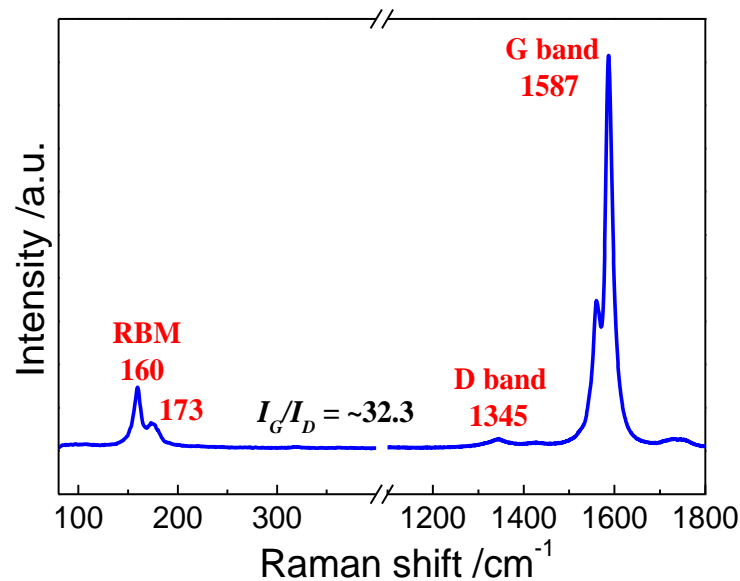
Figure 15. A typical Raman spectrum of as-grown SWCNTs from mist flow CVD.

1.5.5.2 Scanning electron microscopy (SEM)

As shown in Figure 16, the SEM is an instrument that produces a largely magnified image by using electrons instead of light to form an image of the morphology of a sample. A beam of electrons is produced at the top of the microscope by an electron gun.

The electron beam follows a vertical path through the microscope, which is held within a vacuum. The beam travels through electromagnetic fields and lenses, which focus the beam down toward the sample. Once the beam hits the sample, electrons and X-rays are ejected from the sample. Detectors collect these X-rays, backscattered electrons, and secondary electrons and convert them into a signal that is sent to a screen similar to a television screen producing the final image.

Figure 16. The actual picture (left) and schematic (right) of the SEM instrument [86].
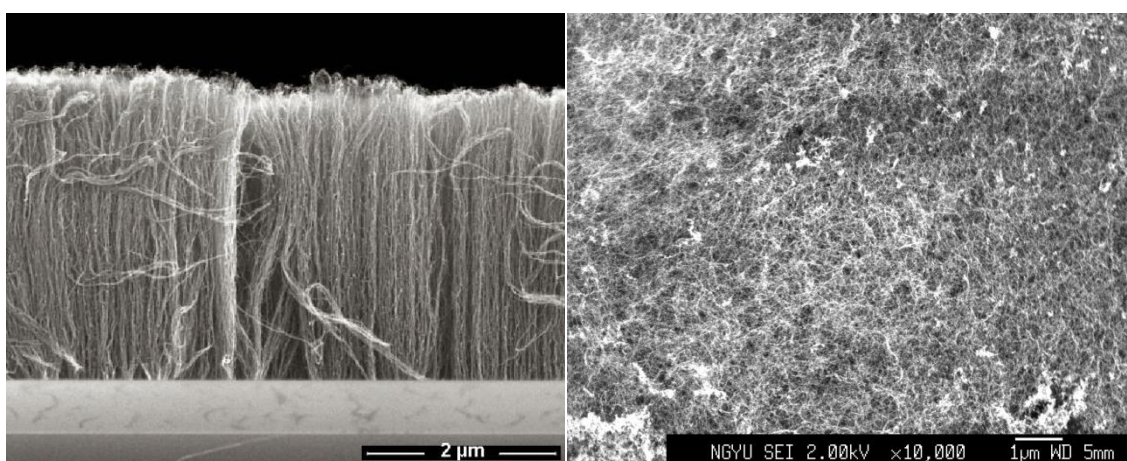
Figure 17. Typical SEM images of aligned CNTs arrays at the vertical orientation (left) [87] and the top morphology of my own sample (right).

With the help of SEM, it is possible to observe the external structures within a resolution better than 1 nm. In addition, we can achieve the SEM images of both the vertical orienta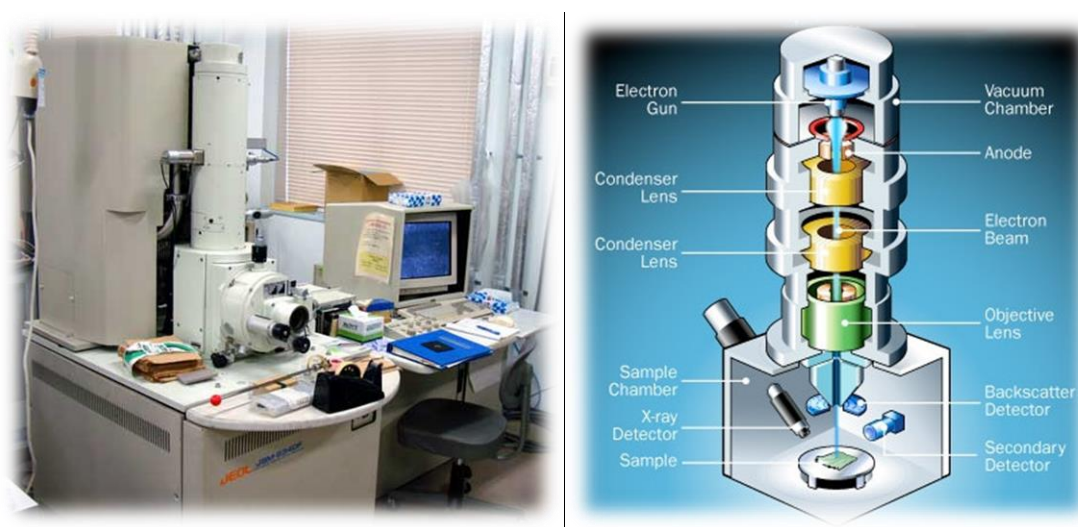tion and the top morphology of the sample (Figure 17). However, there is a bottleneck of SEM observation: it is difficult to distinguish that the sample consists of SWCNTs or MWCNTs. So at this time, some much more powerful instruments are necessary for obtaining the detail information about the style of the sample, such as the transmission electron microscopy.

1.5.5.3 Transmission electron microscopy (TEM)

As shown in Figure 18, although a TEM operates much like a light microscope, it uses the electrons instead of visible light likewise since the wavelength of electrons is much smaller than visible light and allows the visualization of thin slices of material with nanometer resolution. Electrons are collimated from the source, passed through the sample, and the resulting pattern of electron transmission and absorption is magnified onto a viewing screen (the image is typically recorded with a CCD camera).

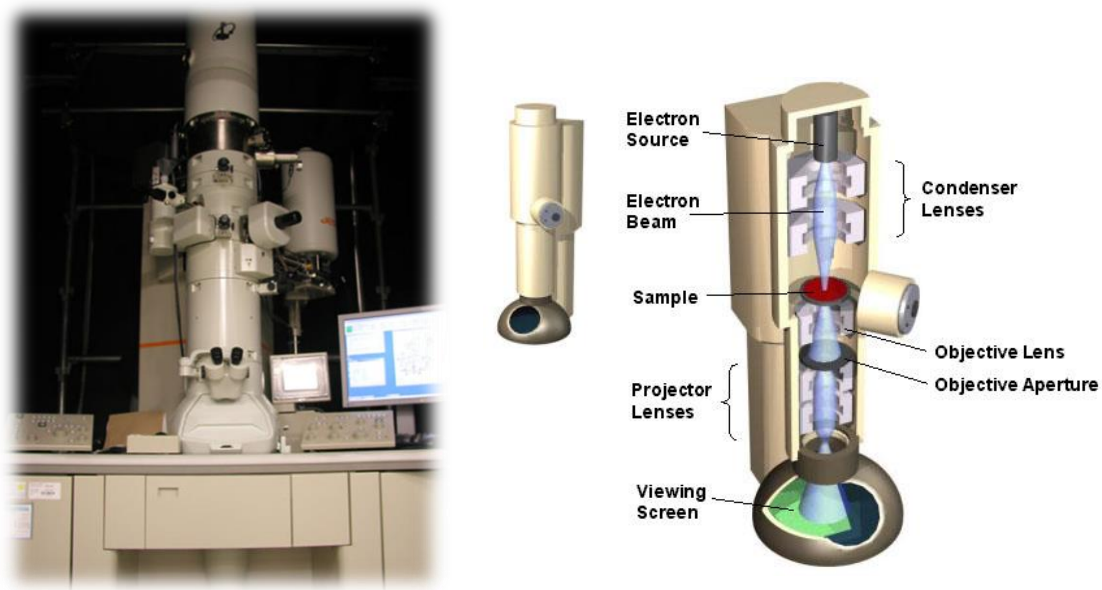Figure 18. The actual picture (left) and schematic (right) of the TEM instrument [88].

The operation of the objective lens allows the imaging of the object in the corresponding image plane by focusing of electrons starting with different directions from individual object points to the corresponding image points. Additionally in the objective aperture, all those electrons are focused to one point, which started in the same direction from any point in the object leading to the diffraction pattern of the object. A bright field image contrast can be obtained by arranging a contrast aperture in the objective aperture in order to eliminate all electrons, which are scattered and diffracted, respectively into large angles. Depending on the setting of the intermediate lens, one may image either the objective aperture or the image plane of the objective lens in the image plane of the projector lens. Furthermore, diffraction images can be easily obtained by changing the path of electrons. From the diffraction pattern, the detail information about crystal structure or chirality of a nanotube can be extracted with the help of Bragg's law [89-91].

To be honest, there are still a few drawbacks of the TEM technique. For example, TEM analysis is a relatively time consuming process according to the different goals of some certain experiments, such as the calculation of diameter distribution of as-grown SWCNTs and in *situ* TEM observation of fusion reaction. The former needs at least one hundred individual as-grown SWCNTs, sometimes even several hundreds, in order to assure the accuracy of the results and the latter usually takes couples of hours even several days to observe the prospective experimental phenomenon. Moreover, the structure of the sample (fullerene clusters) may also be changed during the preparation process of TEM grid or under the irradiation of electron beam, which also has a potential to destroy the sample [92].

1.5.5.4 Thermal gravimetric analysis

Thermal gravimetric analysis (TGA) is an analytical technique used to determine a material's thermal stability and its fraction of volatile components by monitoring the weight change that occurs as a specimen is heated. The measurement is normally carried out in air or in an inert atmosphere, such as N_2, He and Ar, and the weight is recorded as a function of increasing temperature (with constant heating rate), or as a function of time (with constant temperature and/or constant mass loss) [93]. It can provide the information about the either physical or chemical phenomena. In addition, TGA is commonly used to determine the selected characteristics of materials that exhibit either mass loss or gain due to decomposition, oxidation or loss of volatiles (such as moisture).

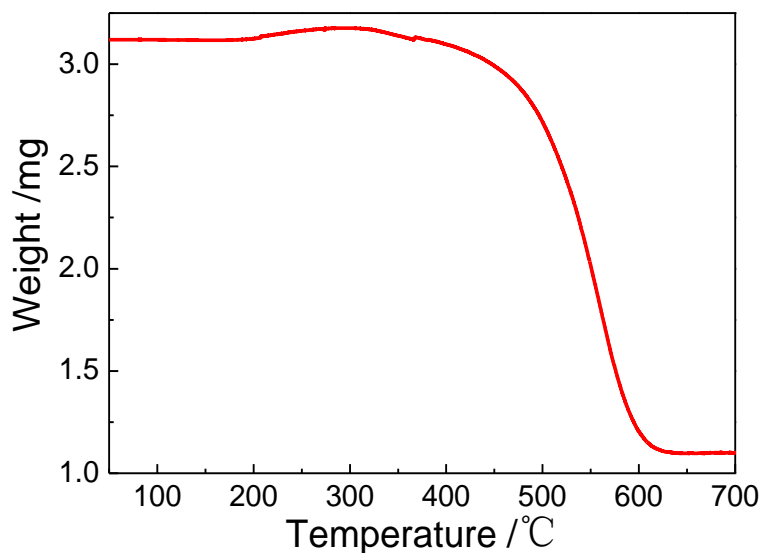Figure 19. TGA profile of the as-grown products synthesized by mist flow CVD using the ferrocene as the catalyst (at a heating rate 2 ℃/min in air with 10 mL/min).

This technique is also very useful to estimate the quality of carbon nanotubes. For

example the metal content of CNTs by evaluating the residual wt % at the end of the

thermal-oxidative curve [94-95] and also the start temperature of the oxidative process

can be correlated with presence of lattice defects (i.e. the less defects, the higher the

temperature) [96]. Also the shape of weight derivate (wt %/℃) curve throughout the

analysis can give some information about the presence of carbon by products, such as

amorphous carbon [97]. Figure 19 is an example of thermal oxidation experiment on the

as-grown products with mist flow CVD choosing the ferrocene as the catalyst.

1.5.5.5 Photoluminescence (PL)

As already described, the SCWNTs could be considered either as metallic or

semiconducting type. The gap energy of the semiconducting tubes is related to the

chirality [98-99] and is approximately proportional to the inverse of the tube diameter

[100]. Photoluminescence from the recombination electron–hole pairs at the band gap

has to be expected. The photoluminescence emission is then only possible with E_{11}

transition while a wide range of wavelength is useful for the photoluminescence

excitation. Thus, different (n, m) SWCNTs in a sample will show various superpositions

of distinct E_{xx} transitions which will appear with different wavelengths [101]. As a

consequence, the nature (semiconducting or not), the geometries and the diameters

could be accessible using the photoluminescence technique. However, the SWCNTs are

preferable to be grouped in bundles, where nanotubes interact between each other with

Van der Waals force so that photoluminescence signal cannot be detected because of this

interaction between semiconducting and metallic nanotubes. As a result, the bundles

must be separated into individual tubes. One of the most popular techniques is the

ultrasonication treatment of the nanotubes with surfactants in water suspension such as

sodium dodecyl sulfate (SDS) [102–105]. This process could be done using various CNTs samples. The photoluminescence is also observed using individual nanotubes grown in channels of zeolite [106].

Nevertheless, no excitonic luminescence can be produced in metallic tubes because electron can be excited, thus resulting in optical absorption, but the hole is immediately filled by another electron out of many available in metal so that no exciton is produced (Figure 20).
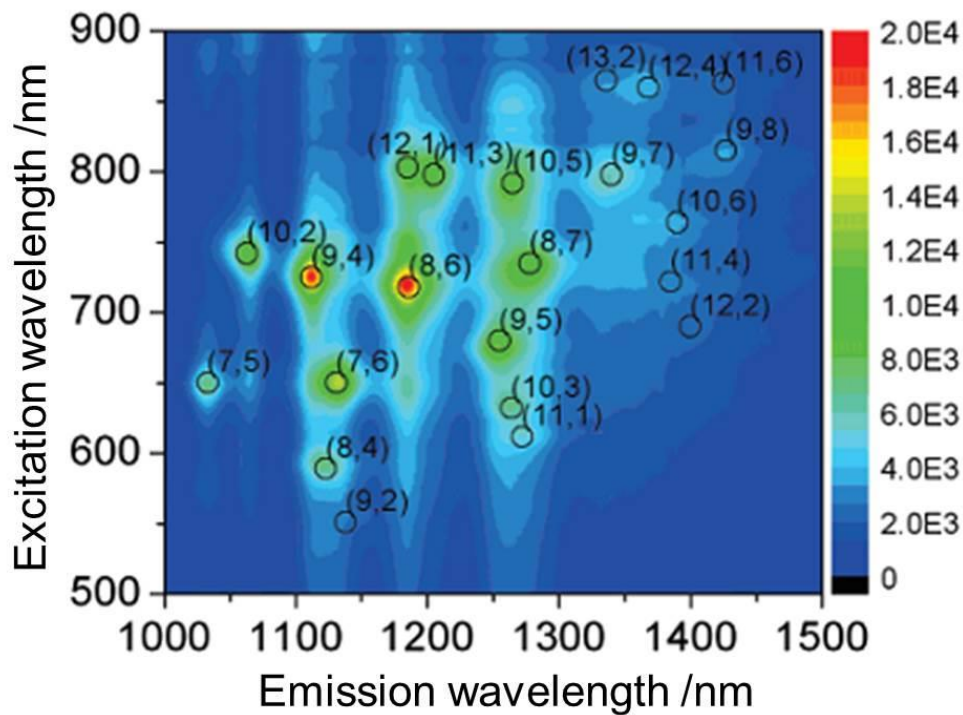

Figure 20. Photoluminescence map from SWCNTs. (n, m) indexes identify certain semiconducting nanotubes. Note that PL measurements do not detect nanotubes with $n = m$ or $m = 0$ [107].

1.6 Overview

A fundamental description of carbon nanotubes, including their diversity, classification, properties, characterizations, applications and synthesis method, has been given in Chapter 1. Through the demonstration of the properties of CNTs, it is worthwhile to note that there a deep connection between the chirality and the diameter of SWCNTs. Therefore, the invention of a novel method to synthesize SWCNTs with the prospective diameter or chirality (controllable/selective growth of SWCNTs) is extremely necessary. In Chapter 2, a novel mist flow CVD has been developed. Through the study on the influence of various parameters on the mean diameter and diameter distribution of as-grown SWCNTs, we can prove that this mist flow CVD is feasible and effective for the controllable growth of SWCNTs. Subsequently, a one-step catalyst-free mist flow CVD growth of SWCNTs with C_{60} fullerenes has been investigated with the help of an aqueous colloidal C_{60} solution consisting of the water and C_{60} fullerenes in Chapter 3. As a result, uniform SWCNTs can be synthesized due to the uniform size of C_{60} molecules. Finally in Chapter 4, a metal cluster (Fe_{18}) has been tried to synthesize thin SWCNTs (0.8 nm) using the CCVD and mist flow CVD. Different carbon source (used for dissolving Fe_{18} clusters) can lead to the different types of as-grown CNTs.

References

1. R. Saito, G. Dresselhaus, M. S. Dresselhaus, Physical properties of carbon nanotubes, Imperial college press, London, 1998.

2. Fullerenes and Cosmic Carbon. Science 329, 1159 (2010).

3. "Valence Shell Electron Pair Repulsion", The Chemogenesis web book.

4. T. W. Ebbesen, Carbon Nanotubes, Edited by T.W. Ebbesen, CRC Press (Boca Raton, New York, London, Tokyo) 1997, Chapter I.

5. http://hyperphysics.phy-astr.gsu.edu/hbase/minerals/diamond.html
   http://nextbigfuture.com/2009/02/lonsdaleite-also-called-hexagonal.html

6. B. McEnaney, Carbon Materials for Advanced Technologies, Edited by T. D. Burchell, Pergamon (Amsterdam, Lausanne, New York, Oxford, Shannon, Singapore, Tokyo) 1999, Chapter I.

7. P. Ruffieux, Thesis: Interaction of hydrogen with sp^2-bonded carbon: Effects on the local electronic structure, University of Fribourg, Switzerland (2002).

8. T. S. V. Satyanarayana, R. Rai. Journal of Interdisciplinary Density 1, 93 (2011).

9. D. William, Jr. Callister, Materials Science and Engineering: An Introduction, New York, John Wiley & Sons, 2002.

10. E. A. Rohlfing, D. M. Cox, A. Kaldor, J. Chem. Phys. 81, 3322 (1984).

11. H. S. Carman Jr., R. N. Compton, J. Chem. Phys. 98, 2473 (1993).

12. H. W. Kroto, J. R. Heath, S. C. O'Brien, R. F. Curl, R. E. Smalley, Nature 318, 162 (1985).

13. M. S. Dresselhaus, G. Dresselhaus, P.C. Eklund, Science of Fullerenes and Carbon Nanotubes, Academic Press (San Diego, Boston, New York, London, Sydney, Tokyo, Toronto) 1996, Chapter XIX.

14. S. Iijima, Nature 354, 56 (1991).

15. S. Iijima, T. Ichihashi, Nature 363, 603 (1993).

16. R. H. Baughman, A. A. Zakhidov, W. A. de Heer, Science 297, 787 (2002).

17. J. Cao, Q. Wang, M. Rolandi, H. Dai, Phys. Rev. Lett. 93, 216803 (2004).

18. K. Hata, D. N. Futaba, K. Mizuno, T. Namai, M. Yumura, S. Iijima, Science 306, 1362 (2004).

19. E. W. Wong, P. E. Sheehan, C. M. Lieber, Science 277, 1971 (1997).

20. H. L. Zhang, B. Wu, W. P. Hu, Y. Q. Liu. Chem. Sov. Rev. 40, 1324 (2011).

21. W. M. Merchan, A. V. Saveliev, L. Kennedy, W. C.Jimenez, Progress in Energy and Combusion Science 36, 696 (2010).

22. Y. Ando, Fullerenes Sci. Technol. 173, 173 (1994).

23. D. S. Bethune, C. H. Klang, M. S. De Vries, G. Gorman, R. Savoy, J. Vazquez, R.

Beyers, Nature 363, 605 (1993).

24. A. Thess, R. Lee, P. Nikolaev, Science 273, 483 (1996).

25. Guo et al, Chem. Phys. Lett. 243, 49.

26. S. Bandow, A. Asaka, Y. Saito, A.M. Rao, L. Grigorian, E. Richter, P.C. Ecklund: Phys. Rev. Lett. 80, 3779 (1998)

27. T. Guo, P. Nikolaev, A.G. Rinzler, D. Tomanek, D. T. Colbert, R. E. Smalley: J. Phys. Chem. 99, 10694 (1995).

28. A. Thess, R. Lee, P. Nikolaev, H. Dai, P. Petit, J. Robert, C. Xu, Y. Hee, S. G. Kim, A. G. Rinzler, D. T. Colbert, G. E. Scuseria, D. Tomnek, J. E. Fischer, R. Smalley, Science 273, 483 (1996).

29. W. K. Maser, E. Munoz, R. E. Smalley, A. M. Benito, M. T. Martinez, G. F. de la Fuente, Y. Maniette, E. Anglaret, J. L. Sauvajol, Chem. Phys. Lett. 292, 587 (1998).

30. E. Munoz, W. Maser, A. M. Benito, M. T. Martinez, G. F. de la Fuente, A. Righi, J. L. Sauvajol, E. Anglaret, Y. Maniette, Appl. Phys. A 70, 145 (2000).

31. T. Guo, M. D. Diener, Y. Chai, M. J. Alford, R. E. Haufler, S. M. McClure *et al.,* Science 257, 1661 (1992).

32. Y. Ando, X. Zhao, T. Sugai, M. Kumar, Mater. Today 7, 22 (2004).

33. R. Sen, Y. Ohtsuka, T. Ishigaki, D. Kasuya, S. Suzuki, H. Kataura *et al.*, Chem. Phys. Lett. 332, 467 (2000).

34. H. Kataura, Y. Kumazawa, Y. Maniwa, Y. Ohtsuka, R. Sen, S. Suzuki *et al.*, Carbon 38, 1691 (2000).

35. H. Kataura, A. Kimura, Y. Ohtsuka, S. Suzuki, Y. Maniwa, T. Hanyu *et al.*, J. Appl. Phys. 37 616 (1998).

36. Y. Avigal, R. Kalish, Appl. Phys. Lett. 78, 2291 (2001).

37. S. Bandow, A. M. Rao, K. A. Williams, A. Thess, R. E. Smalley, P. C. Eklund, J. Phys. Chem. B 101, 8839 (1997).

38. I. W. Chiang, B. E. Brinson, A. Y. Huang, P. A. Willis, M. J. Bronikowski, J. L. Margrave *et al.*, Phys. Chem. B 105, 8297 (2001).

39. H. Ishii, H. Kataura, H. Shiozawa, H. Yoshioka, H. Otsubo, Y. Takayama *et al.*, Nature 426, 540 (2003).

40. M. S. Dresselhaus, G. Dresselhaus, P. H. Avouris, Topics in Applied Physics, Springer, New York, 2001.

41. P. Nikolaev, M. J. Bronikowski, K. Bradley, F. Rohmund, D. T. Colbert, K. A. Smith, R. E. Smalley, Chem. Phys. Lett. 313, 91 (1999).

42. M. J. Bronikowski, P. A. Williams, D. T. Colbert, K. A. Smith, R. E. Smalley, J. Vac. Sci. Technol., A 19, 1800 (2001).

43. H. M. Cheng, F. Li, X. Sun, S. D. M. Brown, M. A. Pimenta, A. Marucci, G. Dresselhaus, M. S. Dresselhaus, Chem. Phys. Lett. 289, 602 (1998).

44. M. Endo, CHEMTECH 18, 568 (1988), 18.

45. G. G. Tibbetts, C. A. Bernardo, D. W. Gorkiewicz, R. L. Alig, Carbon 32, 569 (1994).

46. B. C. Satishkumar, A. Govindaraj, R. Sen, C. N. R. Rao, Chem. Phys. Lett. 293, 47 (1998).

47. M. Kumar, Y. Ando, J. Nanosci. Nanotechnol. 10, 3739 (2010).

48. R. T. K. Baker, M. A. Barber, P. S. Harris, F. S. Feates, and R. J. Waite, J. Catalysis 26, 51(1972).

49. R. T. K. Baker and R. J. Waite, J. Catalysis 37, 101(1975).

50. R. Brukh, O. Sae-Khow, S. Mitra. Chem. Phys. Lett. 459, 149 (2008).

51. A. Nel, T. Xia, L. Mädler, N. Li. Science 311, 622 (2006).

52. D. Takagi, Y. Kobayashi, Y. Homma. J. Am. Chem. Soc. 131, 6922 (2009).

53. Y. Yao, C. Feng, J. Zhang, Z. Liu. Nano Lett. 9, 1673 (2009).

54. J. Liu, C. Wang, X. M. Tu, B. L. Liu, L. Chen, M. Zheng, C. W. Zhou. Nat. Commun. 3, 1 (2012).

55. I. Ibahim, A. Bachmatiuk, D. Grimm, A. Popov, S. Makharza, M. Knupfer, B. Büchner, G. Cuniberti, M. H. Rümmeli. ACS Nano 6, 10825 (2012).

56. X. C. Yu, J. Zhang, W. M. Choi, J. Y. Choi, J. M. Kim, L. B. Gan, Z. F. Liu. Nano Lett. 10, 3343 (2010).

57. J. P. Salvetat, J. M. Bonard, N. H. Thomson, A. J. Kulik, L. Forró, W. Benoit, L. Zuppiroli, Appl. Phys. A 69, 255 (1999).

58. Wikipedia, Carbon nanotube.

59. P. Serp, M. Corrias, P. Kalck, Appl. Catal. A 253, 337 (2003).

60. J. M. Moon, K. H. An, Y. H. Lee, Y. S. Park, D. J. Bae, D. S. Park, J. Phys. Chem. B 105, 5677 (2001).

61. S. H. Hong, S. Myung, Nature Nanotechnology 2, 207 (2007).

62. S. M. Bachilo *et al.*, Science 298, 2361 (2002).

63. M. J. O'connell *et al.*, Science 297, 593 (2002).

64. J. Lefebvre, J. Fraster, P. Finnie, Y. Homma, Phys. Rev. B 69, 075403 (2004).

65. H. Harutyunyan *et al.*, Nano Lett. 9, 2010 (2009).

66. H. Kataura, Y. Kumazawa, Y. Maniwa, I. Umezu, S. Suzuki, Y. Ohtsuka, Y. Achiba, Synth. Met. 103, 2555 (1999).

67. http://www.photon.t.u-tokyo.ac.jp/~maruyama/kataura/kataura.html

68. W. I. Milne, T. B. K. Teo, G. A. J. Amaratunga, P. Legagneuz, L. Gangloff, J. P.

Schnell et al., J. Mater. Chem. 14, 933 (2004).

69. W. B. Choi, D. S. Chung, J. H. Kang, H. Y. Kim, Y. W. Jin, I. T. Han *et al.*, Appl. Phys. Lett. 75, 3129 (1999).

70. Y. H. Lee, Y. T. Jang, D. H. Kim, J. H. Ahn, B. K. Ju, Adv. Mater. 13, 479 (2001).

71. W. B. Choi, Y. W. Jin, H. Y. Kim, S. J. Lee, M. J. Yun, J. H. Kang *et al.*, Appl. Phys. Lett. 78, 1547 (2001).

72. T. W. Tombler, C. W. Zhou, L. Alexseyev, J. Kong, H. J. Dai, L. Lei *et al.*, Nature 405, 769 (2000).

73. E. Frackowiak, K. Metenier, V. Bertagna, F. Beguin, Appl. Phys. Lett. 77, 2421 (2000).

74. M. Hughes, G. Z. Chen, M. S. P. Shaffer, D. J. Fray, A. H. Windle, Chem. Mater. 14, 1610 (2002).

75. E. Frackowiak, F. Beguin, Carbon 40, 1775 (2002).

76. A. C. Dillon, K. M. Jones, T. A. Bekkedahl, C. H. Kiang, D. S. Bethune, M. J. Heben, Nature 386, 377 (1997).

77. C. Park, P. E. Anderson, A. Chambers, C. D. Tan, R. Hidalgo, N. M. Rodriguez, J. Phys. Chem. B 103, 10572.

78. M. S. Dresselhaus, G. Dresselhaus, R. Saito, A. Jorio, Physics Reports 409, 47 (2005).

79. A. Jorio, R. Saito, J. H. Hafner, C. M. Lieber, M. Hunter, T. McClure, G. Dresselhaus, M. S. Dresselhaus, Phys. Rev. Lett. 86, 1118 (2001).

80. M. Milnera, J. Kürti, M. Hulman, H. Kuzmany, Phys. Rev. Lett. 84, 1324 (2000).

81. M. J. O'Connell, S. M. Bachilo, X. B. Huffman, V. C. Moore, M. S. Strano, E. H. Haroz, K. L. Rialon, P. J. Boul, W. H. Noon, C. Kittrell, J. Ma, R. H. Hauge, R. B. Weisman, R. E. Smalley, Science 297, 593 (2002).

82. C. Fantini, *et al.*, Phys. Rev. Lett. 93, 147406 (2004).

83. P. C. Eklund *et al.*, Carbon 33, 959 (1995).

84. A. Jorio, M. A. Pimenta, A. G. Souza Filho, R. Saito, G. Dresselhaus, M. S. Dresselhaus, New J. Phys. 5, 1.1 (2003).

85. M. S. Dresselhaus, G. Dresselhaus, A. Jorio, A. G. Souza Filho, Ge. G. Samsonidze, R. Saito, J. Nanosci. Nanotechnol. 3 19 (2003).

86. http://ahshonorschemistry.wikispaces.com/K-Scanning+Electron+Microscopy

87. http://www.ikts.fraunhofer.de/en/research_fields/smartmicrosystems/functionallayer smicoreletrwearprotect/alignedcarbinnanotubes.html

88. http://barrett-group.mcgill.ca/tutorials/nanotechnology/nano02.htm

89. K. Takayanagi, Y. Tanishiro, M. Takahashi, S. Takahashi, J. Vac. Sci. Technol. A 3,

1502 (1985).

90. J. F. Colomer, L. Henrard, P. Lambin, G. Van Tendeloo, Phys. Rev. B 64, 125425 (2001).

91. M. Gao *et al.*, Appl. Phys. Lett. 82, 2703 (2003).

92. Wikipedia, transmission electron microscopy.

93. A. W. Coats, J. P. Redfern, Analyst 88, 906 (1963).

94. S. Musso *et al.*, Diam. Relate. Mater. 15, 385 (2006).

95. C. M. Chen *et a*l., Diam. Relate. Mater. 14, 798 (2005).

96. S. Porro, S. Musso, M. Vinante, L. Lanzetti, M. Anderle, F. Trotta, A. Tagliaferro, Physica E 37, 58 (2007).

97. K. L. Strong *et al*., Carbon 41, 1477 (2003).

98. M. Ouyang, J. L. Huang, C. L. Cheung, C. M. Lieber, Science 292, 702 (2001).

99. J. S. Lauret, C. Voisin, G. Cassabois, P. Roussignol, C. Delalande, A. Filoramo, L. Capes, E. Valentin, O. Jost, Physica E 21, 1057 (2004).

100. X. Liu, T. Pichler, M. Knupfer, M. S. Golden, J. Fink, H. Kataura, Y. Achiba, Phys. Rev. B 66, 045411 (2002).

101. Y. Miyauchi, S. Chiashi, Y. Murakami, Y. Hayashida, S. Maruyama, Chem. Phys. Lett. 387, 198 (2004).

102. J. Lefebvre, J. M. Fraser, Y. Homma, P. Finnie, Appl. Phys. A 78, 1107 (2004). R. B. Weisman, S. M. Bachilo, D. Tsyboulski, Appl. Phys. A 78, 1111 (2004).

103. M. J. O'Connell, S. M. Bachilo, C. B. Huffman, V. C. Moore, M. S. Strano, E. H. Haroz, K. L. Rialon, P. J. Boul, W. H. Noon, C. Kittrell, J. Ma, R. H. Hauge, R. B. Weisman, R. E. Smalley, Science 297, 503 (2003).

104. S. Lebedkin, F. Hennrich, T. Skipa, M. M. Kappes, J. Phys. Chem. B 107, 1949 (2003).

105. J. Guo, C. Yang, Z. M. Li, M. Bai, H. J. Liu, G. D. Li, E. G. Wang, C. T. Chan, Z.

106. K. Tang, W. K. Ge, X. Xiao, Phys. Rev. Lett. 93, 017402-1 (2004).

107. Y. Miyata, T. Kawai, Y. Miyamoto, K. Yanagi, Y. Maniwa, H. Kataura. J. Phys. Chem. C 111, 9671 (2007).

Chapter 2

Parametric Influences on the Controllable CVD Growth of Single-Wall Carbon Nanotubes using Mist Flow Method

2.1 Introduction

Since their discovery in 1991 by Iijima [1], carbon nanotubes (CNTs), especially single-wall carbon nanotubes (SWCNTs), have attracted tremendous attentions due to their prominent mechanical, thermal, electronic properties and potential applications in a wide range of fields, such as composites and electronic devices [2-5]. It is well-known that the properties of SWCNTs are significantly dependent upon their diameter and chirality, and therefore a development of structure-controllable growth techniques of SWCNTs is essential; chemical vapor deposition (CVD) has been considered as one of the most promising method to achieve the controllable growth of SWCNTs [6-12].

The gas-phase growth of SWCNTs is achieved by passing mixed flow of organometallic catalyst precursors and carbon sources through a heated furnace reactor [7]. Therefore, the floating catalyst CVD [13], such as direct injection pyrolytic synthesis (DIPS), HiPco and aerosol methods [14-19], has the potential to achieve the large scale controllable growth of SWCNTs because it is a continuous process including both catalyst particle formation and subsequent SWCNTs growth occurring in the same reactor [20-22]. In addition, no need to deposit catalyst on the substrate can lead to a simple and low-cost production of SWCNTs. It is still an imperative issue to develop a

controllable SWCNTs growth based on floating catalyst CVD.

Here, we propose an improved floating catalyst CVD synthesis of SWCNTs using a continuous flow of ferrocene-ethanol mist to control the mean diameter and diameter distribution of as-grown SWCNTs. The experimental setup is simple and basically a mist generator (HM-2412 Vibrator, Honda Electronics Co., Ltd) that can generate fine ferrocene-ethanol droplets with average diameter of 3 μm. The influence of various parameters (CVD reaction temperature, total flow rate and ferrocene concentration in ethanol) on controlling the mean diameter and diameter distribution of as-grown SWCNTs has been investigated by Raman spectroscopy, scanning electron microscopy (SEM), transmission electron microscopy (TEM). Hopefully, the results of this study could be useful to promote the comprehension of the controllable growth of SWCNTs in a floating CVD system.

2.2 Experimental Section

In all our CVD experiments, ethanol (C_2H_5OH, 99.8%, Wako) and ferrocene (Fe ($C_5H_5)_2$, Wako) are used as carbon source and the catalyst precursor, respectively. A vertical tubular furnace of 35 cm long and a quartz tube of 75 cm long (3 cm outer diameter) have been equipped as shown in Fig. 1. There are two separate flowmeters connected with two separate lines. One is connected with the ferrocene-ethanol container to carry the mist as the carrier gas and the other one is used for controlling the flow rate of the buffer gas (also pure Ar). These two kinds of gases are mixed at the top of the quartz tube and fed into the furnace. So in this experiment, the flow rate means the total flow rate, which consists of Ar flow rate of the carrier gas and buffer gas.
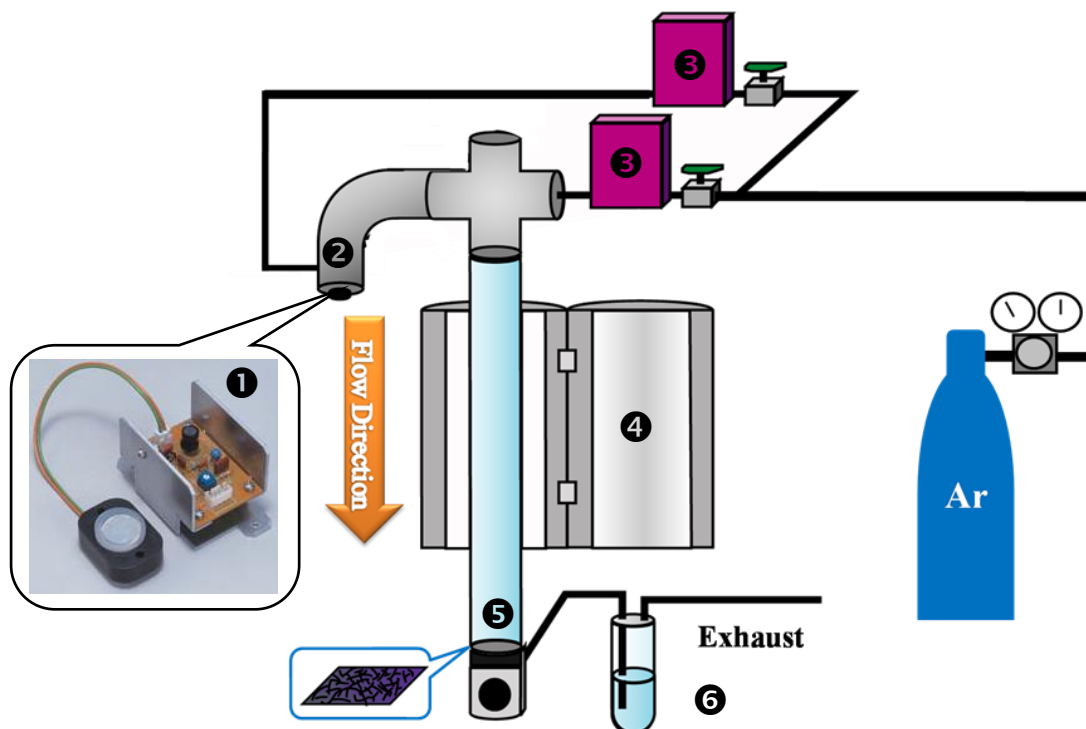
Figure 1.　The schematic diagram of mist flow CVD system: ❶ Mist generator ❷ Ferrocene-ethanol container ❸ Flowmeter ❹ Electrode furnace ❺ Substrate ❻ Water trap

Different amount of ferrocene was dissolved into 100 mL ethanol to prepare the starting solution of different concentration. A constant amount (15 mL) of the prepared solution was then transferred into the container attached with a mist generator and used for each CVD experiment. The substrate was loaded at the bottom of the quartz tube in order to collect the deposited products. Prior to heating, pure Ar at 1000 standard cubic centimeter per minute (sccm) total flow rate was fed into the system for 15 min to eliminate all the air in the whole CVD setup. When the CVD temperature was stabilized (the range is from 900℃ to 1050℃), the mist generator was turned on to generate a small amount of mist containing the droplets of ferrocene-ethanol with an average diameter of 3 μm. The total flow rate was controlled at the range from 400 to 1200 sccm.

After 15 min reaction time, the mist generator was shut down and the furnace was cooled gradually to room temperature under Ar atmosphere. The supply rate of the ferrocene-ethanol solution is ca. 1 mL per minute. After 15 min deposition time, the mist generator was shut down and the furnace cooled down gradually to room temperature under argon atmosphere. The whole CVD experimental process was performed at atmospheric pressure. In order to study the effects of a particular parameter, all other variables were kept constant while varying the given certain parameter. The SWCNTs collected on the substrate were characterized by Raman spectroscopy, SEM and TEM.

2.3 Results and discussion

2.3.1 Effects of CVD reaction temperature

To study the influence of CVD reaction temperature on the controllable growth of SWCNTs, a series of samples was synthesized at 900, 950 and 1050℃, while maintaining the other parameters kept constant: total flow rate of 1000 sccm and ferrocene concentration in ethanol of 1.0 wt%.

As demonstrated clearly in Fig. 2, as the reaction temperature increases, the impurities attaching at the outer surface of as-grown products also increase. In fact, high temperature can accelerate the decomposition rate of EtOH in the mist droplets, which may produce excessive carbons leading to amorphous impurities on the surface of products. The ratio of G and D band intensities (I_G/I_D) has been used as a reflection of the quality of as-grown SWCNTs. The inset in Fig. 3a is the ratio of I_G/I_D as a function of CVD reaction temperature. This result shows that the minimum I_G/I_D was observed at reaction temperature of 1050℃, which is consistent with the SEM and TEM
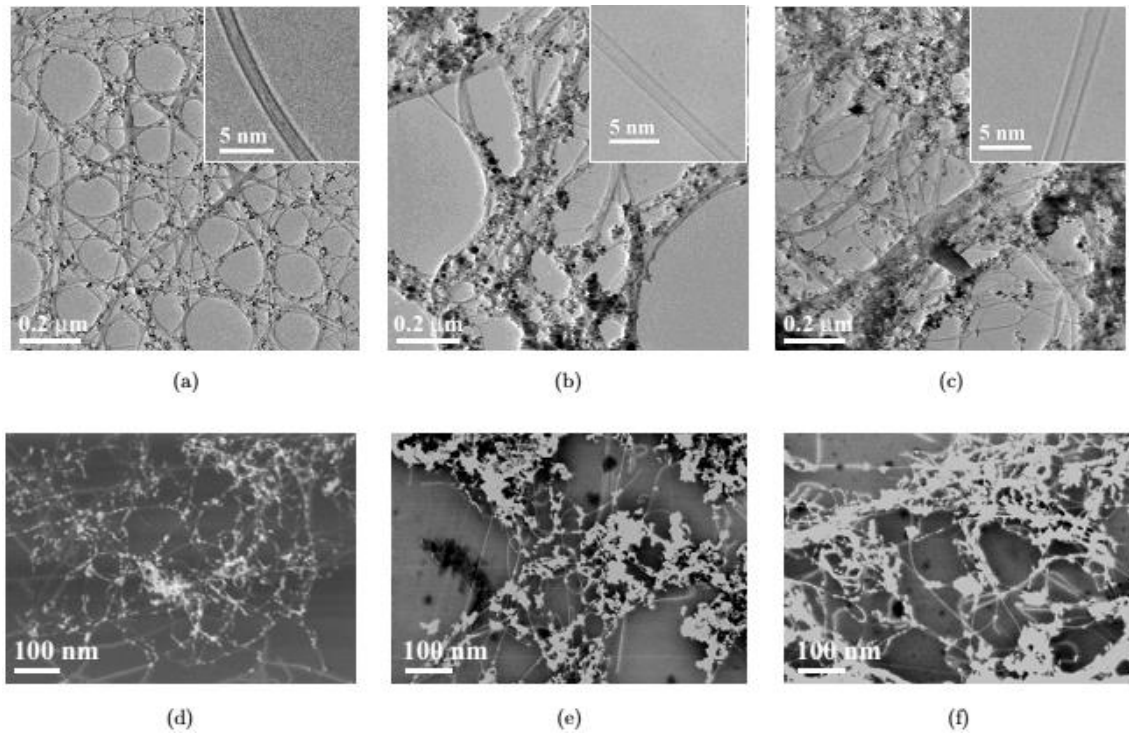
observations.

Figure 2. Low magnification TEM and SEM images of as-grown SWCNTs synthesized under different CVD reaction temperature: (a,d) 900℃, (b,e) 950℃, (c,f) 1050℃. The insets in (a-c) are the corresponding typical HRTEM images showing the main products are all SWCNTs.

On the basis of the observed RBM peaks, we can estimate the diameter of SWCNTs from an empirical relationship: $d = 248/\omega_{RBM}$ [23], where ω_{RBM} is the RBM frequency measured and d is the diameter of SWCNTs. Based on this relationship, we can speculate the change of the diameter of as-grown SWCNTs through comparing the movement and intensity of RBM peaks with each other. Resonance effect is generally prominent in Raman spectroscopy of SWCNTs. Hence, to evaluate diameter distribution correctly, we employed three different excitation laser wavelengths at 633, 514 and 488 nm to measure Raman spectra of as-grown SWCNTs. As shown in Fig. 3b, the relative

intensity of RBM peaks at the high frequency region (200 cm^{-1}~) decreases as the CVD reaction temperatures increase, which is observed under all excitation laser wavelengths. Apparently, the observed alternation of the spectral feature of RBM peaks results from the increase of relative abundance of larger diameter as-grown SWCNTs. Figure 3c is the corresponding diameter distribution of as-grown SWCNTs of three different CVD reaction temperatures, where the diameter distribution was measured based on TEM images of as-grown SWCNTs. As shown clearly, there is a tendency that the abundance of smaller diameter tubes decreases gradually, whereas the larger diameter tubes start to appear correspondingly, which is consistent with the results of the Raman spectroscopy results. The mean diameter of as-grown SWCNTs increases from 1.2 to 1.5 nm as the growth temperature increases. There might be the enlargement of the catalyst particles leading to the formation of larger nuclei for SWCNTs [24]. Furthermore, higher temperatures accelerate the decomposition rate of the ferrocene, which results in the formation of the larger catalyst particles. As a result, the size of the catalyst particles becomes larger and larger, which is suitable for the growth of the larger diameter SWCNTs [25-27].

As a matter of fact, the influence of low temperature on the diameter of as-grown SWCNTs had also been investigated. Another three samples were synthesized at 700, 750 and 800℃, while keeping the other parameters constant: total flow rate of 1000 sccm and ferrocene concentration in ethanol of 1.0 wt%. From the Raman spectra within RBM range measured by 488, 514 and 633 nm laser excitation wavelength, we can see that there is no regular shift of RBM peaks. This should be because lower temperature would lead to the inadequate decomposition of the catalyst particles so that
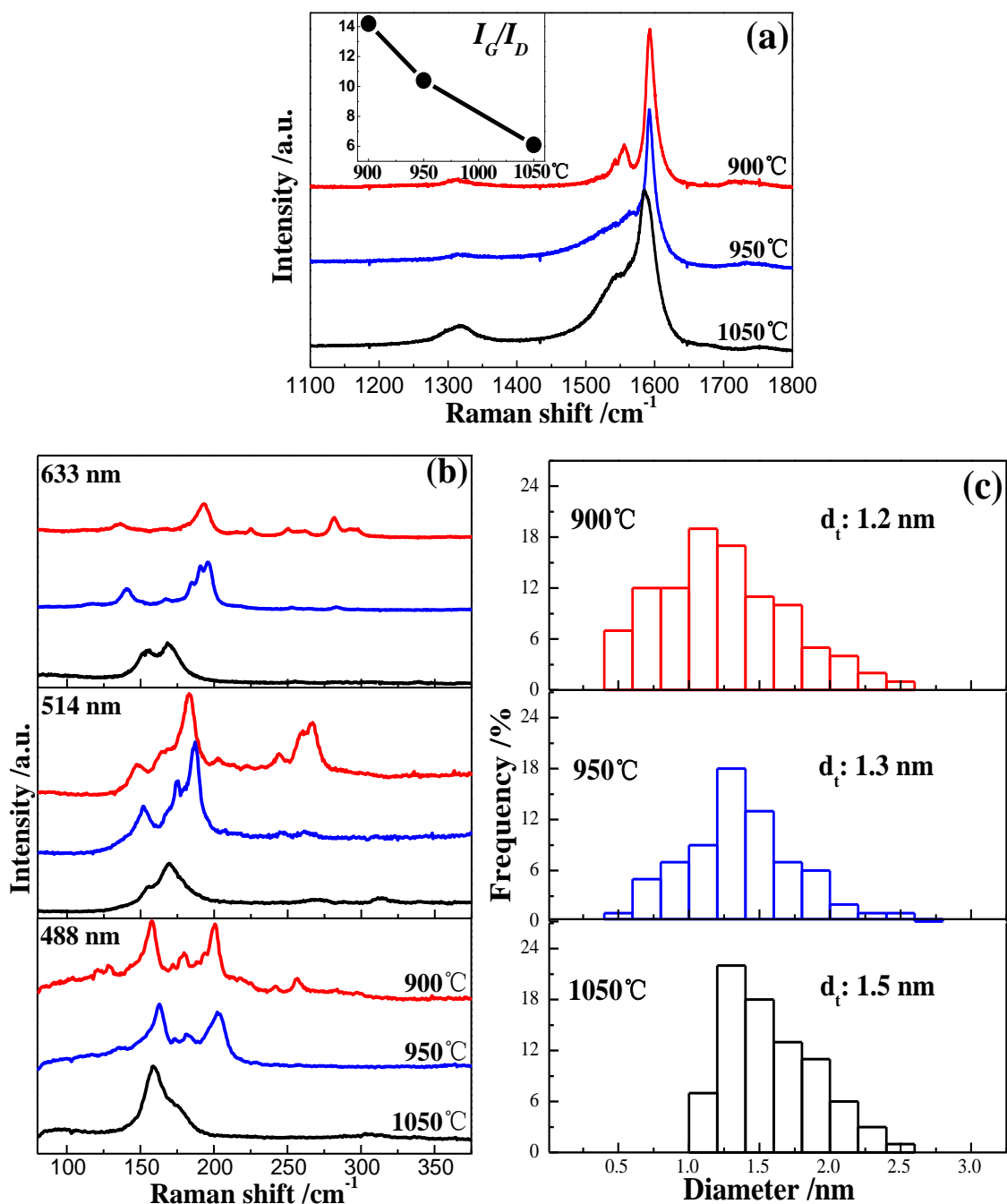
Figure 3. (a-b) Raman spectra of as-grown SWCNTs synthesized under different CVD reaction temperatures measured by three different laser excitation wavelengths respectively. The inset in (a) is the corresponding I_G/I_D ratio graph. (c) The statistical diameter distribution histograms of as-grown individual SWCNTs at different temperatures with 100 individual SWCNTs from HRTEM images, respectively.

there could be so many larger particles formed and the diversity of catalyst particle size during CVD process within the short residence time, which would result in the formation of DWCNTs or MWCNTs in order to cause the irregular variation of the diameter of as-grown SWCNTs.
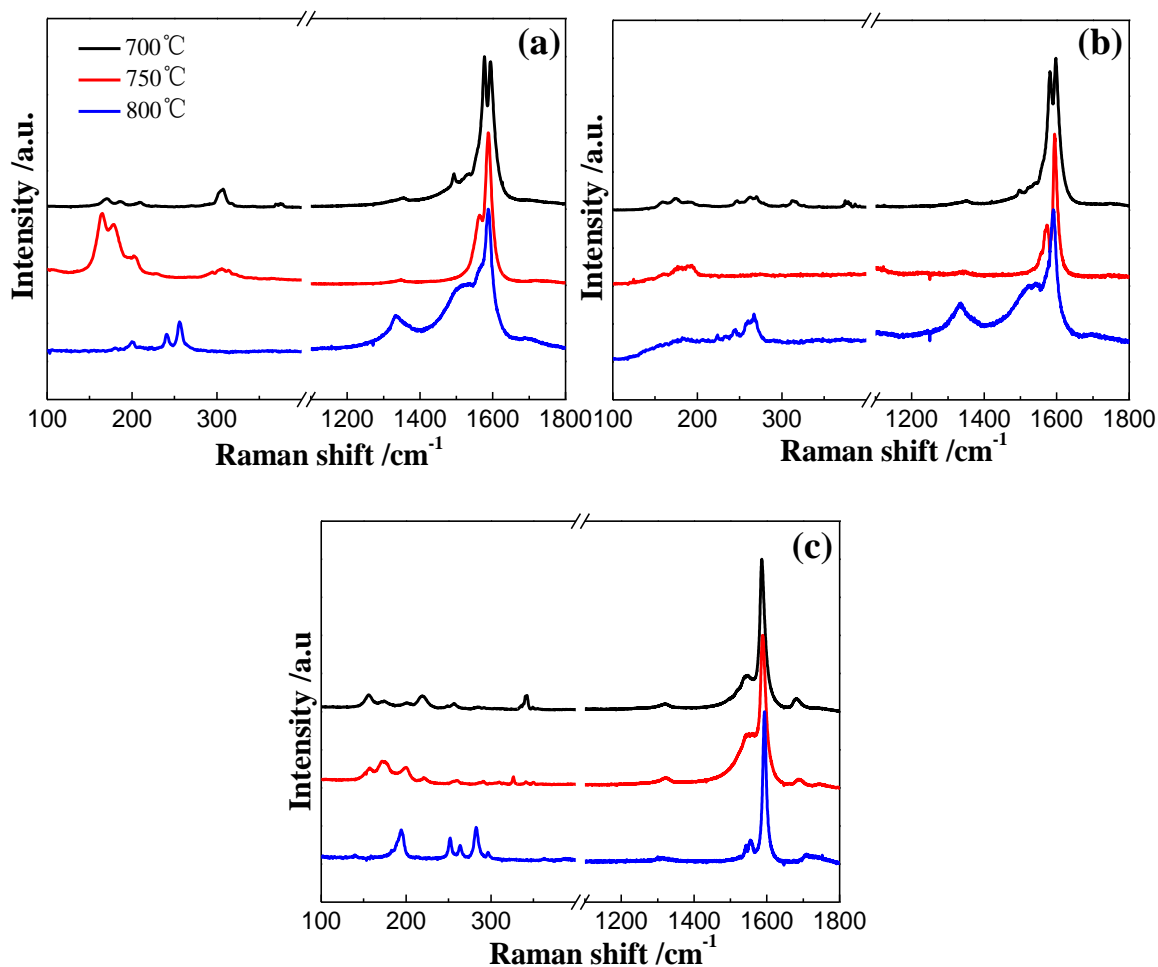

Figure 4. Raman spectra of as-grown SWCNTs synthesized at three lower CVD reaction temperatures measured by three different laser excitation wavelengths: (a) 488 nm, (b) 514 nm and (c) 633 nm.
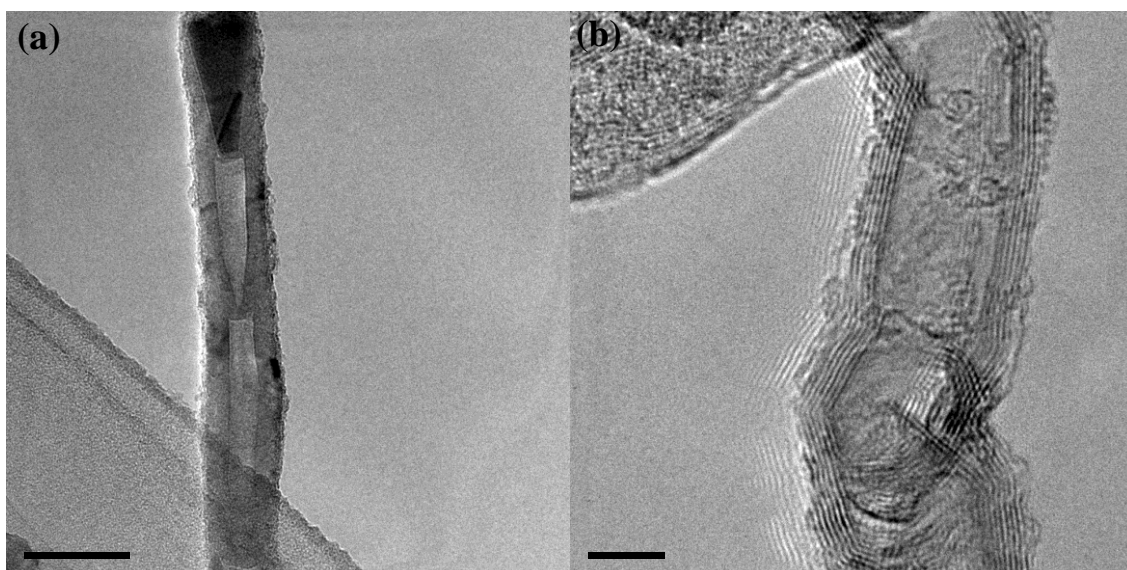
Figure 5. HRTEM images of MWCNTs synthesized at (a) 700℃ and (b) 800℃, respectively.

2.3.2 Effects of total flow rate

In the present floating CVD system, the function of the carrier gas is to feed the catalysts and carbon source into the CVD reactor. And the total flow rate can be varied by controlling the flow rate of buffer gas without changing the other parameters. SWCNTs samples have been synthesized under four different total flow rates of 400, 800, 1000 and 1200 sccm (300 sccm of carrier gas and 100, 500, 700, 900 sccm of buffer gas, respectively) , while maintaining the other parameters (CVD reaction temperature of 900℃ and ferrocene concentration in ethanol of 1.0 wt%) constant.

As shown in Figs. 6a-d, the amount of impurities decreases as the increase of total flow rate, which can be also confirmed by SEM observation (Fig. 6e-h). To further characterize the as-grown SWCNTs samples, Raman spectroscopy with three different excitation laser wavelengths at 633, 514 and 488 nm was utilized. As shown in Fig. 7a, increasing the total flow rate results in the decrease of the intensity of D band so that the

highest I_G/I_D ratio was obtained at 1200 sccm (inset in Fig. 7a). Figures 7b shows the RBM features of as-grown SWCNTs observed by three different excitation laser wavelengths at 633, 514 and 488 nm. The relative intensity of RBM peaks located at higher frequency decreases with increasing the total flow rate: the relative abundance of larger diameter SWCNTs increases with the increase of the total flow rate. The mean diameter and diameter distribution estimated by TEM observation is consistent with the results of Raman spectroscopy. The mean diameter and the diameter of prominent tubes increase gradually as the total flow rate increases, whereas the amount of smaller diameter tubes decreases and some larger diameter tubes appear when the total flow rate has reached at 1200 sccm (Fig. 7c).
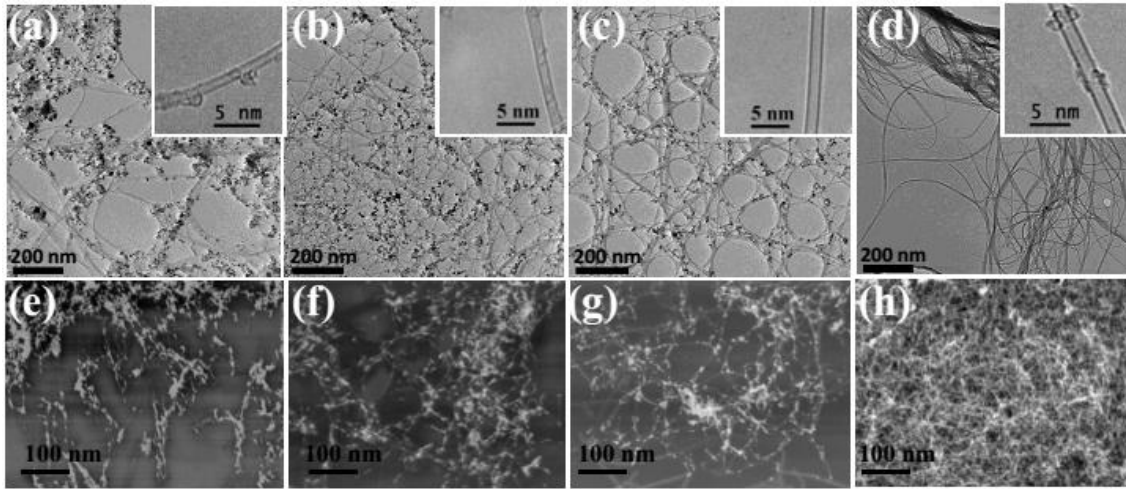

Figure 6. Low magnification TEM and SEM images of as-grown SWCNTs synthesized at different total flow rate: (a,e) 400 sccm, (b,f) 800 sccm, (c,g) 1000 sccm, (d,h) 1200 sccm. The insets in (a-d) are the corresponding typical HRTEM images showing the main products are all SWCNTs.

In general, the diameter of as-grown SWCNTs decreases as the flow rate increases. This is because of the fact that increasing flow rate may reduce the residence time of

catalyst particles; there is no sufficient time for catalyst particles to grow to larger ones, which leads to the growth of smaller diameter SWCNTs. In the current mist flow CVD system, however, an opposite trend has been observed. According to a theoretical study by Fan *et al*. [28-29], the diameter of as-grown SWCNTs is determined not only by catalyst particle size but also by kinetics factors. In the initial stage of the growth of CNTs, it has been known that the so-called SWCNT cap structures should be formed on the surface of catalyst particles. The growth of the cap structure can be kinetically governed by the carbon supply during the CVD synthesis.

In the normal catalyst-supported CVD synthesis of SWCNTs [30], where the average diameter distribution of metal catalyst particles is small (ca. 1-2 nm), the average tube diameter is mainly proportional to CVD temperature and not so sensitive to carbon source (such as ethanol) and gas flow rate.

However, in the present mist flow CVD synthesis, the feeding of the carbon source into the CVD chamber is strongly dependent on the total flow rate, where the rate and total amount of evaporation of the mist (ethanol) particles limit the carbon supply to catalyst metal particles. Also, the growth of the Fe catalyst during the CVD reaction within the mist particles determines the average diameter of SWCNTs produced. Although the details of the present mist flow CVD mechanism have not been clarified yet, these mutually relating growth kinetics play a crucial role in producing the observed diameter distribution of SWCNTs.
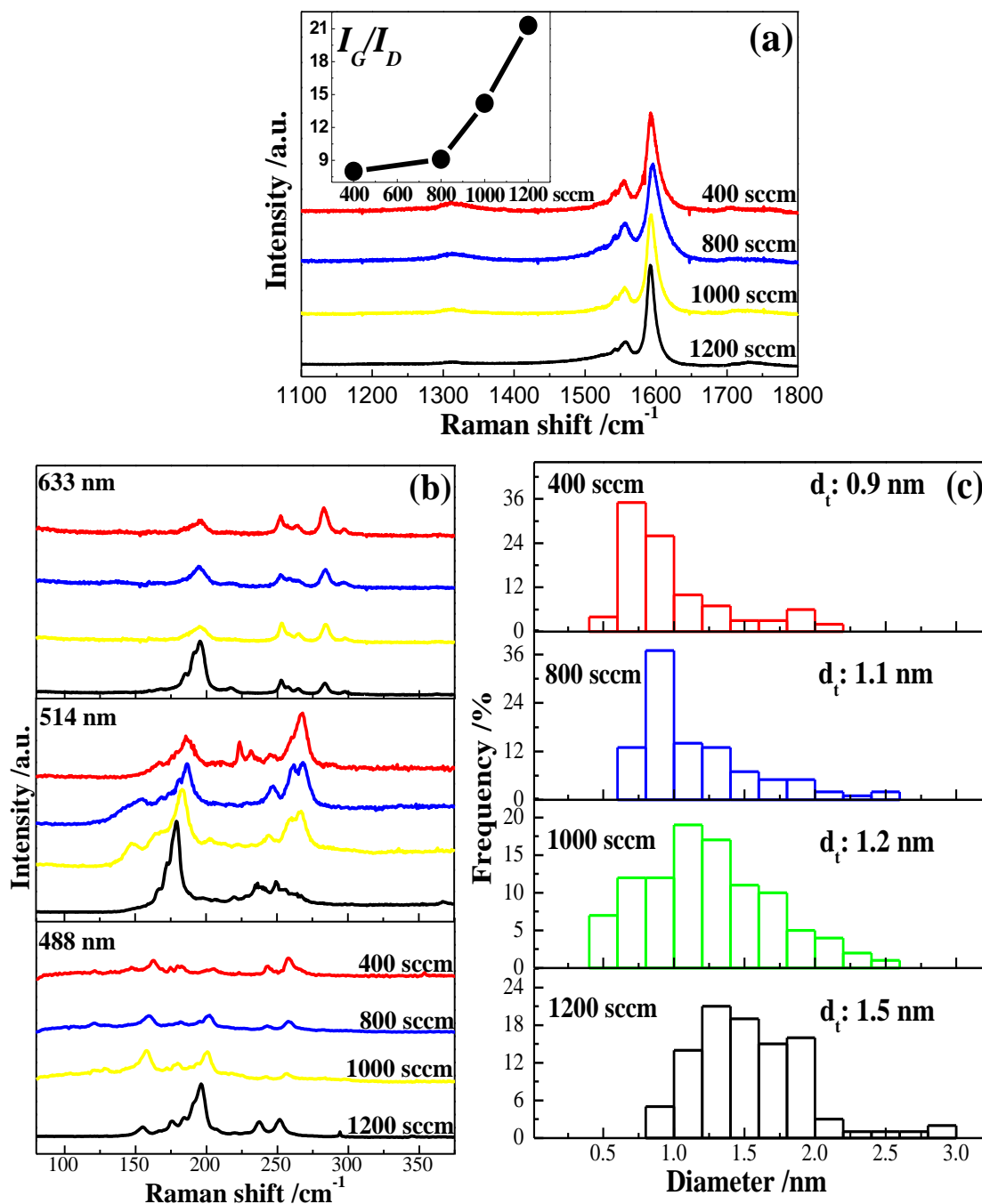
Figure 7. (a-b) Raman spectra of as-grown SWCNTs synthesized at different total flow rate measured by three different excitation laser wavelengths respectively. The inset into (a) is the corresponding I_G/I_D ratio graph. (c) The statistical diameter distribution histograms of as-grown SWCNTs at different total flow rates with 100 individual SWCNTs from HRTEM images, respectively.

2.3.3 Effects of the ferrocene concentration in ethanol and the growth mechanism for mist flow CVD

To study the influences of the ferrocene concentration in ethanol on the controllable growth of SWCNTs, a series of samples was synthesized at the ferrocene concentration of 0.1, 0.5 and 1.0 wt% while keeping other parameters constant: CVD reaction temperature of $900℃$ and the total flow rate of 1000 sccm. Interestingly, the quality, mean diameter and diameter distribution of the SWCNTs produced are almost the same regardless of the ferrocene concentration in ethanol (Fig. 8 and 9), suggesting that the average diameter of the Fe catalyst formed during the evaporation of ethanol from mist particles does not vary significantly.
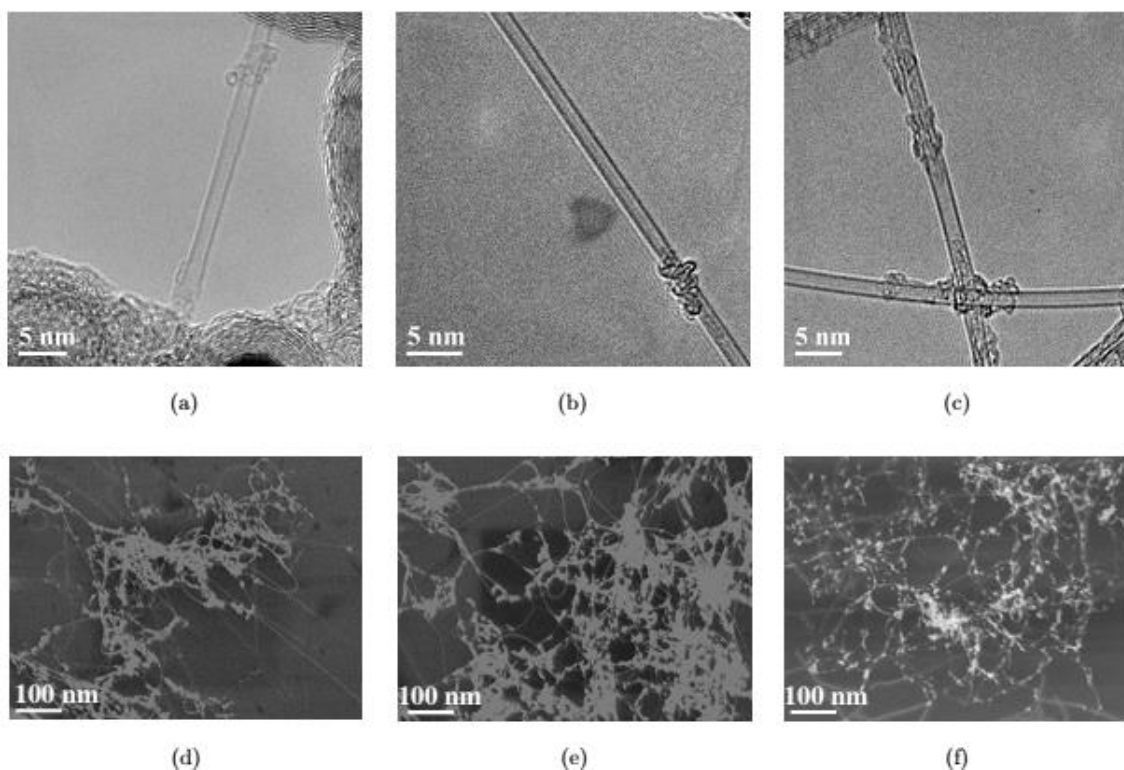

Figure 8. Typical HRTEM and SEM images of as-grown SWCNTs synthesized under different ferrocene in ethanol: (a,d) 0.1wt%, (b,e) 0.5wt%, (c,f) 1.0wt%, respectively.

In general, higher catalyst concentration results in the formation of larger catalyst particle, which leads to the growth of larger diameter SWCNTs [31]. Figure 10 and Figure 11 show TEM images of SWCNTs grown from Fe metal particles. Obviously, the diameter of the SWCNTs is much smaller than those of the metal catalyst particles. Figure 10a, in particular, exhibits that two SWCNTs are grown from the exactly same metal catalyst.

A similar growth mechanism has been reported in the so-called "sea urchin" growth mechanism found in arc-discharged synthesis of SWCNTs using Gd, Y and La metal catalysts [32-34]. The arc-discharge synthesis of SWCNTs using lanthanides catalysts is much different from the normal catalyst-support CVD synthesis employing Fe, Co or Ni catalyst. In the normal CVD synthesis, one metal catalyst particle can provide only a single SWCNT. It has been known that there are two types of the sea urchin growth of SWCNTs: in the La catalyst case [32], the SWCNTs are grown directly from the La metal particles, whereas in the Gd [33] and Y [34] cases, these metal catalysts are covered with thin graphitic layers from which SWCNTs are grown. A close observation of Figs. 10 (a) and (b) suggests that the SWCNTs are grown from thin graphitic layers as in the sea urchin growth with Gd and Y metal catalysts.

Based on these similarities in the growth of SWCNTs, we presume that the present Fe metal catalyst particles are in the form of Fe-C carbide rather than pure Fe state. In fact, the sea urchin growth of SWCNTs has been known to emerge from the carbide states of the La, Y and Gd catalysts.
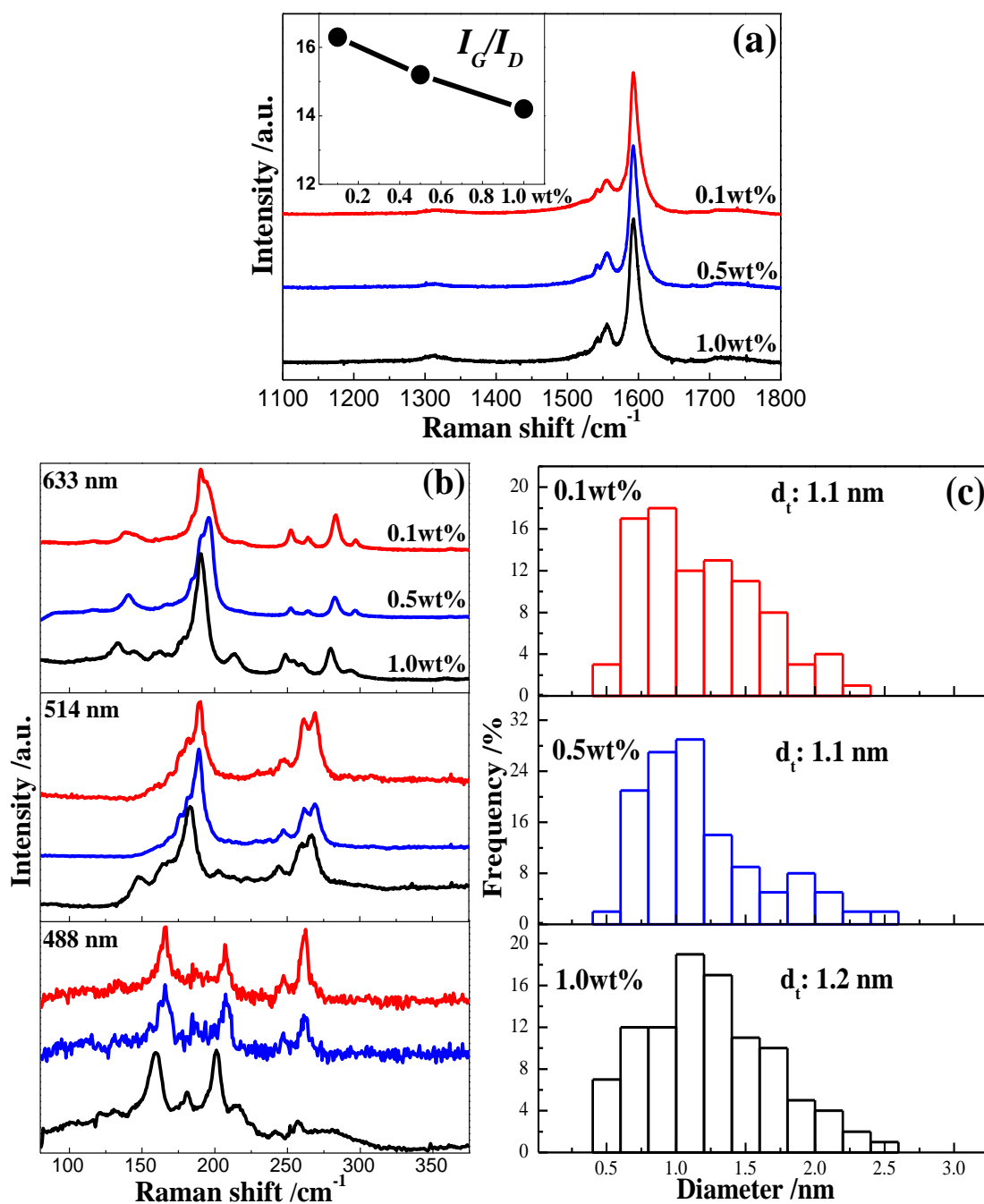
Figure 9. (a-b) Raman spectra of as-grown SWCNTs synthesized at different concentrations measured by three different excitation laser wavelengths respectively. The inset into (a) is the corresponding I_G/I_D ratio graph. (c) The statistical diameter distribution histograms of as-grown SWCNTs at different concentrations with 100 individual SWCNTs from HRTEM images, respectively.
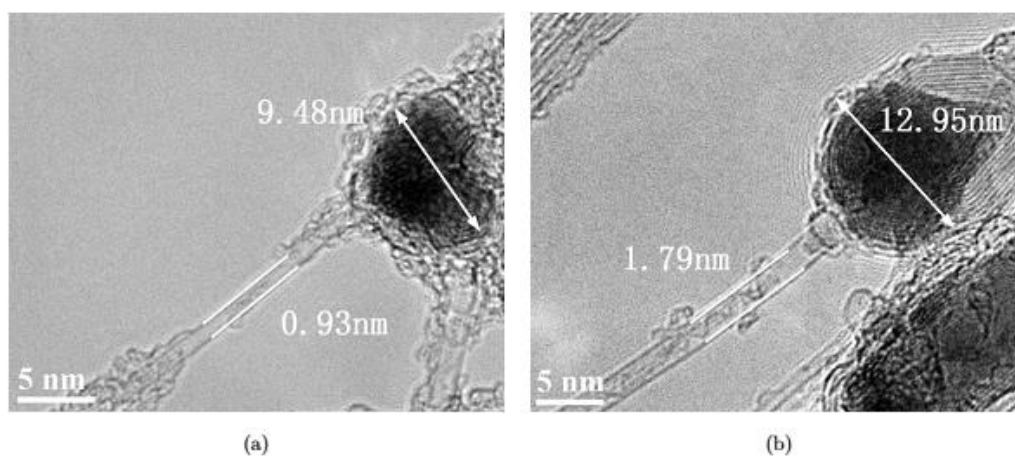
Figure 10. (a-b) Typical HRTEM images of the end of an individual as-grown SWCNT attached by a Fe nanoparticle.
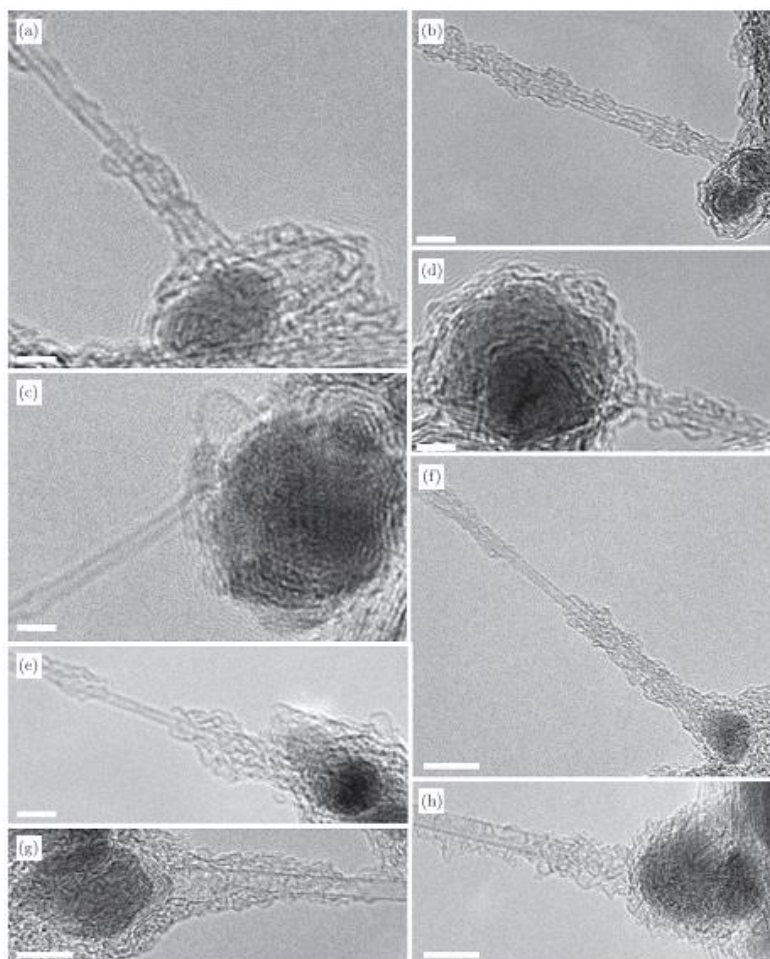

Figure 11. Typical HRTEM images of the end of an individual SWCNT attached by a Fe nanoparticle. The scale bar is 2 nm ((a) ~ (e)) and 5 nm ((f) ~ (h)), respectively.

2.4 Conclusions

A new floating catalyst CVD system for SWCNTs synthesis is reported and characterized by a combined research of Raman spectroscopy, SEM and TEM. Depending on the different combination of various experimental parameters such as ferrocene concentration in ethanol, CVD reaction temperature and total flow rate, the mean diameter of as-grown SWCNTs can be varied from 0.9 to 1.5 nm. In addition, we found that the carbon supply kinetics can be the dominant factor to determine the diameter of as-grown SWCNTs in the present mist flow method, which indicates that control of supply kinetics is significant to achieve structure-selective growth of SWCNTs using the floating catalyst CVD method.

References

1. S. Iijima and T. Ichihashi, Nature 363, 603 (1993).

2. K. Edgar and J. L. Spencer, Curr. Appl. Phys. 4, 121 (2004).

3. D. M. Sun, M. Y. Timmermans and E. I. Kauppinen, Nature Nanotechnol. 10, 1038 (2011).

4. R. Bhowmick, B. M. Clemens and B. A. Cruden, Carbon 46, 907 (2008).

5. G. Gruner, J. Mater. Chem. 16, 3533 (2006).

6. Y. G. Yao, C. Q. Feng, J. Zhang and Z. F. Liu, Nano Lett. 9, 1673 (2009).

7. X. C. Yu, J. Zhang, W. M. Choi, J. Y. Choi, J. M. Kim, L. B. Gan and Z. F. Liu, Nano Lett. 10, 3343 (2010).

8. D. Takagi, Y. Kobayashi and Y. Homma, J. Am. Chem. Soc. 131, 6922 (2009).

9. Y. Homma, H. P. Liu, D. Takagi and Y. Kobayashi, Nano Res. 2, 793 (2009).

10. X. L. Li, X. M. Tu, S. Zaric, K. Welsher, W. S. Seo, W. Zhao and H. J. Dai, J. Am. Chem. Soc. 129, 15770 (2007).

11. G. Y. Zhang, P. F. Qi, X. R. Wang, Y. R. Lu, X. L. Li, R. Tu, S. Bangsaruntip, D. Mann, L. Zhang and H. J. Dai, Science 314, 974 (2006).

12. A. Okamoto and H. Shinohara, Carbon 43, 431 (2005).

13. H. M. Cheng, F. Li, G. Su, H. Y. Pan, L. L. He, X. Sun and M. S. Dresselhaus, Appl. Phys. Lett. 72, 3282 (1998).

14. H. Ago, S. Ohshima, K. Uchida and M. Yumura, J. Phys. Chem. B 105, 10453 (2001)

15. T. Saito, W. C. Xu, S. Ohshima, H. Ago, M. Yumura and S. Iijima, J. Phys. Chem. B 110, 5849 (2006).

16. T. Saito, S. Ohshima, W. C. Xu, H. Ago, M. Yumura and S. Iijima, J. Phys. Chem. B 109, 10647 (2005).

17. P. Nikolaev, M. J. Bronikowski, K. Bradley, F. Rohmund, D. T. Colbert, K. A. Smith and R. E. Smalley, Chem. Phys. Lett. 313, 91 (1999).

18. A. Moisala, A. G. Nasibulin, S. D. Shandakov, H. Jiang, L. Khriachtchev and E. I. Kauppinen, Chem. Eng. Sci. 61, 4393 (2006).

19. A. Moisala, A. G. Nasibulin, D. P. Brown, H. Jiang, L. Khriachtchev and E. I. Kauppinen, Carbon 43, 2006 (2005).

20. T. Hiraoka, S. Bandow, H. Shinohara and S. Iijima, Carbon 44, 1853 (2006).

21. G. Hong, Y. B. Chen, P. Li and J. Zhang, Carbon 50, 2067 (2012).

22. Y. Tian, M. Y. Timmermans, M. Partanen, A. G. Nasibulin, H. Jiang, Z. Zhu and E. I. Kauppinen, Carbon 49, 4636 (2011).

23. A. Jorio, R. Saito, J. H. Hafner, C. M. Lieber, M. Hunter, T. McClure, G. Dresselhaus and M. S. Dresselhaus, Phys. Rev. Lett. 86, 1118 (2001).

24. A. G. Nasibulin, P. V. Pikhitsa, H. Jiang and E. I. Kauppinen, Carbon 43, 2251 (2005).

25. Y. Tian, A. G. Nasibulin, B. Aitchison, T. Nikitin, J. Pfaler, H. Jiang, Z. Zhu, L. Khriachtchev, D. P. Brown and E. I. Kauppinen, J. Phys. Chem. C 115, 7309 (2011).

26. S. Hofmann, R. Sharma, C. Ducati, G. Du, C. Mattevi, C. Cepek, M. Cantoro, S. Pisana, A. Parvez, F. Cervantes-Sodi, A. C. Ferrari, R. Dunin-Borkowski, S. Lizzit, L. Petaccia, A. Goldoni and J. Robertson, Nano. Lett. 7, 602 (2007).

27. G. Lolli, L. Zhang, L. Balzano, N. Sakulchaicharoen, Y. Tan and D. E. Resasco, J. Phys. Chem. B 110, 2108 (2006).

28. X. Fan, R. Buczko, A. A. Puretzky, D. B. Geohegan, J. Y. Howe, S. T. Pantelides and S. Pennycook, J. Phys. Rev. Lett. 90, 145501-1 (2003).

29. J. M. Kieran, M. D. Oscar, T. H. Andrew, Ind. Eng. Chem. Res. 49, 5323 (2010).

30. K. Mukhopadhyay, A. Koshio, T. Sugai, N. Tanaka, H. Shinohara, Z. Konya and J. B. Nagy, Chem. Phys. Lett. 303, 117 (1999).

31. R. Bhowmick, B. M. Clemens and B. A. Cruden, Carbon 46, 907 (2008).

32. Y. Saito, M. Okuda, M. Tomita and T. Hayashi, Chem. Phys. Lett. 236, 419 (1995).

33. S. Subramoney, R. S. Ruoff, D. C. Lorents and R. Malhotra, Nature 366, 637 (1993).

34. D. Zhou, S. Seraphin and S. Wang, Appl. Phys. Lett. 65, 1593 (1994).

Chapter 3

One-step Catalyst-Free Mist Flow CVD Growth of Single-Wall Carbon Nanotubes with C_{60} Fullerenes

3.1 Introduction

Owing to their extraordinary mechanical, electrical and optical properties, single-walled carbon nanotubes (SWCNTs) have been considered as one of the most excellent candidates for the potential applications such as micro-electromechanical devices, sensors, transparent metal electrodes, field-effect transistors and capacitors [1-5]. Although significant efforts have been hitherto devoted for the synthesis of SWCNTs [6-8], most of them are centered on the metal-catalysts-supported chemical vapor deposition (CVD), which can lead to the concomitant complicated purification processes to remove metal catalysts. This purification processes cause degradation of SWCNTs (shortening and defects formation) that can alter the intrinsic properties of as-grown SWCNTs [9-10]. Hence, catalyst-free growth of SWCNTs has been developed during the past decade [11-17]; growth of SWCNTs from diamonds and cloning SWCNTs from open-end SWCNT seeds, for example [18-20]. In light of the previous studies, the growth of SWCNTs via opened fullerenes is feasible [21-22].

Due to the uniform size of C_{60} molecules, the growth of CNTs from C_{60} fullerene is a promising method to achieve all-carbon and diameter-selective growth of CNTs. However, up to now, a research on growth of CNTs from C_{60} has been limited; one is

growth from exohedrally functionalized C_{60} [21] and the other is from C_{60} cluster [22]. In addition, both reports have been performed based on supported CVD, which needs a pretreatment such as high-temperature annealing under various condition (air, H_2O and H_2). Further investigation of the CNTs growth from C_{60}, in particular, direct, facile and controllable growth is needed. In contrast to the catalysts-supported CVD, the floating catalyst CVD is capable of continuously synthesizing SWCNTs from the gas phase onto a substrate by simultaneously supplying the catalyst precursor and carbon source [23-26]. Thus low-cost, facile and scalable production of SWCNTs can be realized by taking advantage of floating CVD method. We report here a one-step feasible catalyst-free floating CVD growth of SWCNTs by means of the colloidal aqueous C_{60} solution directly on the basis of the mist flow method.

3.2 Experimental section

3.2.1 Preparation of colloidal aqueous C_{60} solution

Ethanol (EtOH) is one of the most common and useful carbon sources to grow high quality CNTs. Because of the extremely low solubility of C_{60} in the ethanol, we focused on colloidal aqueous/EtOH solution of C_{60} as carbon source. We have prepared the colloidal solution according to the precious papers [27-28]. Shortly 18 mg C_{60} powders were dissolved into 10 ml toluene and then pure water was added to the toluene solution according to the different toluene/water (t/w) ratios; t/w ratio of 1:3, 1:4 and 1:5 were selected in this work. Next the layered solution of toluene and pure water were sonicated at room temperature for two days until the evaporation of toluene was complete. Finally, the certain amount of ethanol was fed into each vial until total volume was 100 ml. The obtained yellow clear solution was used for CNTs growth by
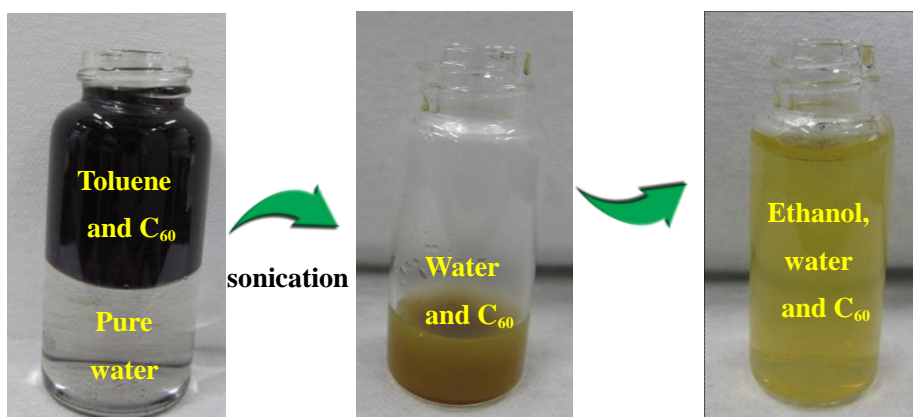
mist flow method (Figure 1).

Figure 1. The fabrication process of an aqueous colloidal C_{60} solution.

3.2.2 Synthesis of SWCNTs with mist flow CVD method

The mist flow CVD synthesis of SWCNTs has been described in the previous chapter [29]. Briefly 15 ml modified C_{60} solution was transferred into a container attached with a mist generator. Prior to CVD, pure Ar of 1000 sccm was introduced into the CVD system for 15 min to eliminate all the air in the chamber. After the temperature became stable, the mist generator was switched on and CVD reaction lasted for 15 min. The as-grown products were collected by the Si substrate loaded at the bottom of the chamber and characterized by various measurements (Raman spectroscopy, TEM, SEM, etc.).

3.3 Results and Discussion

3.3.1 Confirmation of the synthesis of SWCNTs from C_{60}

Figure 2 shows Raman spectra of samples synthesized using C_{60} solution with t/w ratio of 1:3 at different temperatures (850℃, 900℃, 950℃ and 1000℃). As shown in

the figure, Raman spectra of samples prepared at 900 and 950 ℃ shows the characteristic RBM peaks at the frequency range of 150 ~ 300 cm^{-1}, which indicates the successful synthesis of CNTs; in contrast, no RBM signals were observed in the case of sample prepared at 850 and 1000℃. Figure 3a-d show Raman spectrum, SEM and HRTEM images of the sample prepared at 950℃, which clearly demonstrates the formation of SWCNTs using the present mist flow method. To investigate the diameter distribution in detail, we carried out Raman mapping with excitation wavelength of 633 nm. Figure 4b shows Raman spectra obtained at different position marked in the corresponding SEM image shown in Figure 4a (beam size is ca. 1 μm). All RBM peaks locate within 150 ~ 180 cm^{-1}, which indicates a relatively narrow diameter distribution of synthesized SWCNTs. Figure 4c-d displays the results of detailed Raman mapping of G band and RBM peaks, where the different colors respectively represent the different integrated intensity of G band (1585 ~ 1600 cm^{-1}) and RBM peaks (150 ~ 180 cm^{-1}). The color distribution of the G-band map is almost identical to that of the RBM map. Actually, after normalization with G band intensity, the RBM map exhibits almost the unique color (blue) showing a relatively homogeneous diameter distribution in this area.
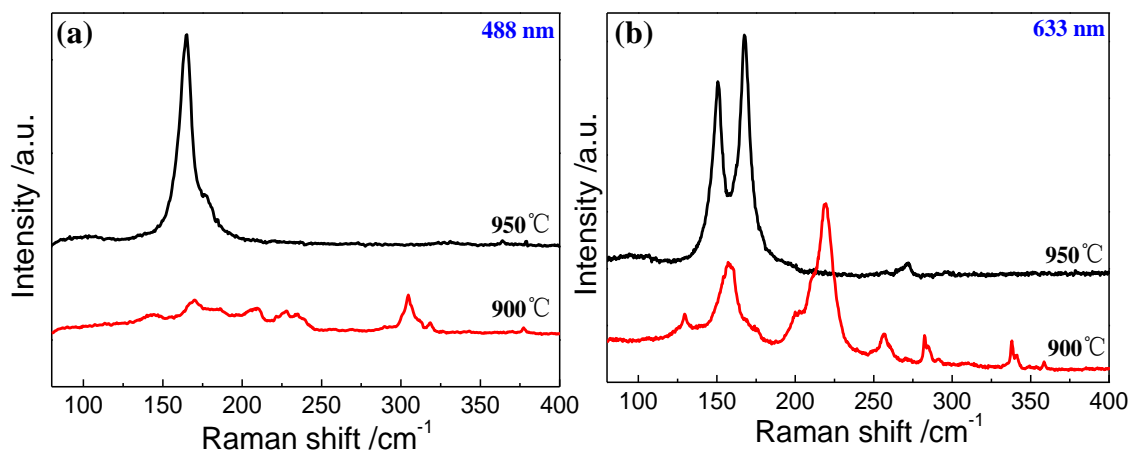

Figure 2. Raman spectra measured by (a) 488 and (b) 633 nm excitation laser wavelength of as-grown products synthesized at different temperature, respectively.

Raman mapping measured at the same location with 488 nm excitation laser wavelength (RBM region is from 165 to 175 cm^{-1}) shows almost the identical results (Figure 5). The diameter distribution was also confirmed by TEM observations. Figure 4f shows histogram representing the diameter distribution of synthesized SWCNTs, which is consistent with the results of Raman spectroscopy. The average diameter is 1.28 nm that is comparable to that of an individual C_{60}. Compared with the size distribution of C_{60} clusters (Figure 6), it can be interpreted as the larger C_{60} clusters providing numerous C_{60} that can potentially be opened and provide a nucleation cap for CNTs. Fragments unavailable for nucleation could coalesce into a larger nucleation cap for the formation of larger diameter SWCNTs under high temperature [21-22].

In order to investigate the effect of amount of water during CVD, another two samples have been prepared at 950℃ with the t/w ratio of colloidal aqueous C_{60} solution of 1:4 and 1:5, respectively. As shown in Figure 7, it is explicit that CNTs can be synthesized under both conditions. As the amount of water increases, the RBM peaks shows blue shift slightly and the diameter becomes inhomogeneous, in particular, when the t/w ratio has reached to 1:5. Indeed the oxygen-based groups have been proved to be considerably significant for both catalyst and catalyst-free growth of CNTs [30-34]. During thermal oxidation, oxygen can be inserted in the C_{60} layer to bridge C_{60} molecules together, which would make C_{60} broken into either individual caps or oxygen-bridged cap/fragment aggregates [32]. At the CVD reaction temperature, oxygen atoms can be removed so that the bridged caps/fragments can coalesce into larger carbon caps for the formation of large-diameter SWCNTs [18]. Moreover, their results have demonstrated that more large-diameter SWCNTs were formed in the case of lower-temperature oxidation treatment compared with higher-temperature oxidation

treatment. That is, more powerful oxidation could lead to the decrease of the diameter of
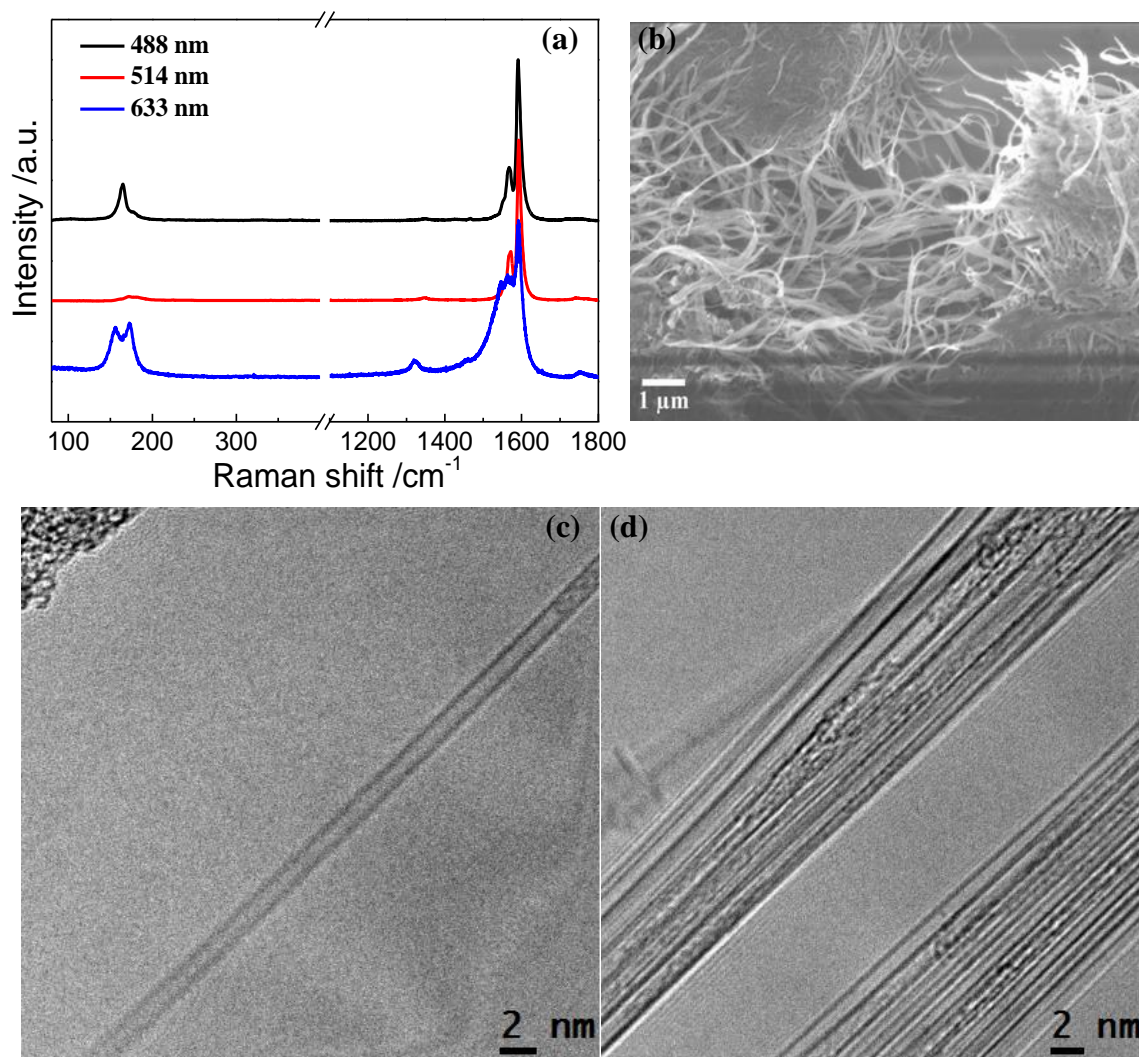

Figure 3. (a) Raman spectrum under three excitation laser wavelengths, corresponding (b) SEM and (c-d) HRTEM images of as-grown products.

as-grown SWCNTs. In our case, it seems that the thermal oxidation and the growth of CNTs should happen together in the CVD chamber and the oxygen should come from water. So as the increase of the amount of water, more oxygen should be formed leading to the more powerful oxidation, which could result in the decrease of the diameter of SWCNTs.
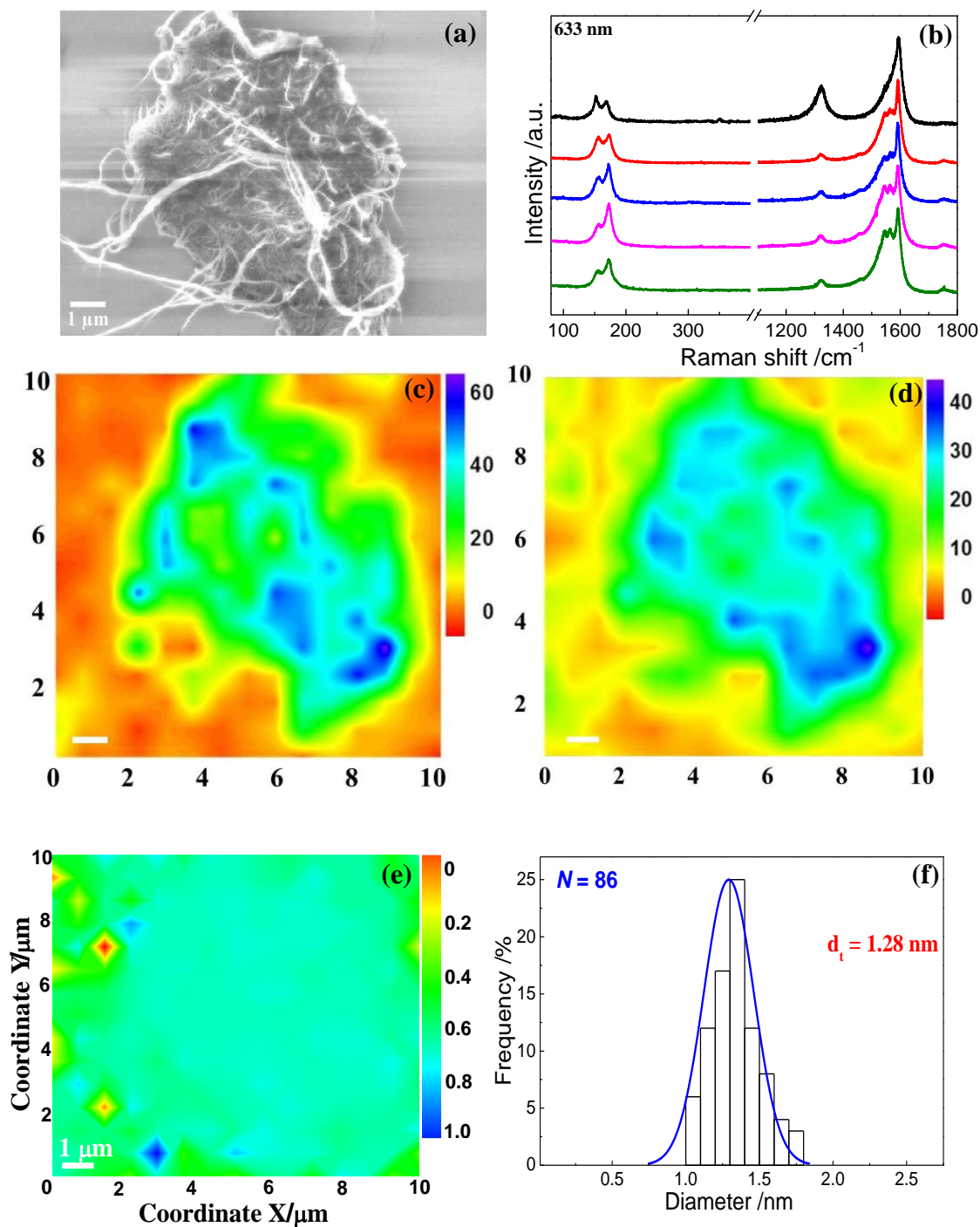
Figure 4. (a) Typical SEM image of as-grown SWCNTs synthesized under the optimum CVD reaction condition and corresponding (b) Raman spectra measured in several marked locations. (c,d) Raman mapping of G-band and RBM measured by 633 nm excitation laser wavelength, respectively. (e) The related normalized RBM Raman mapping and (f) diameter distribution of as-grown SWCNTs. The scale bar of (c-e) is 1 μm and the X, Y axis represents the coordinate x and y, respectively.
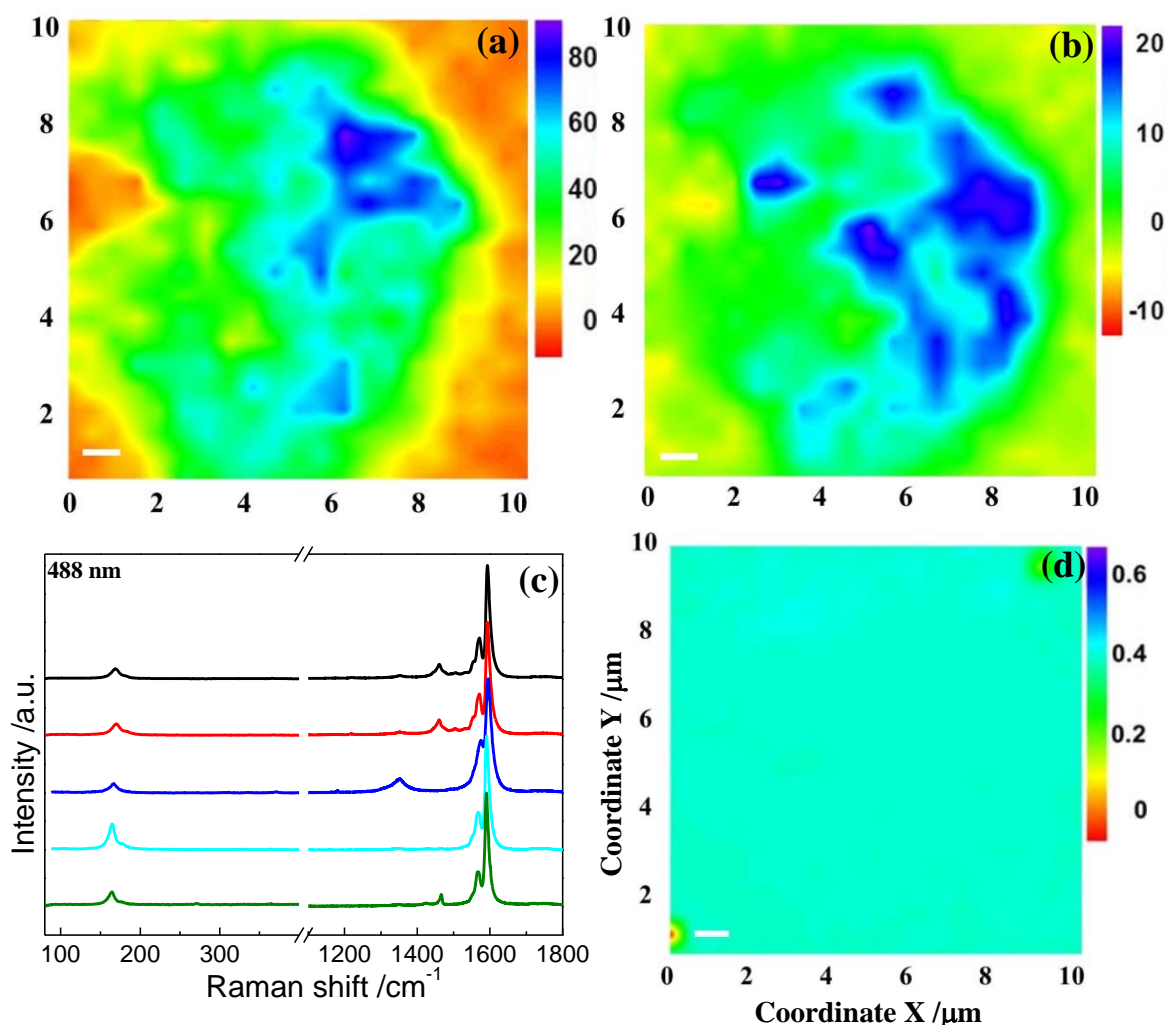
Figure 5. Raman mapping measured by 488 nm excitation laser wavelength of (a) G band (1585 ~ 1600 cm^{-1}) and (b) RBM region (165 ~ 175 cm^{-1}), respectively; (c) corresponding Raman spectrum of different position; (d) RBM Raman mapping after normalization. The scale bar of (a-b and d) is 1 μm and the X, Y axis represents the coordinate x and y, respectively.

And this can also interpret why the diameter of most individual as-grown SWCNTs is bigger than that of an individual C_{60}. In addition, compared with the size distribution of C_{60} clusters (Figure 6b), we can assume that the larger C_{60} clusters can provide a larger number of C_{60} that can potentially be opened and coalesce into a larger nucleation cap for the formation of larger diameter SWCNTs under high temperature.
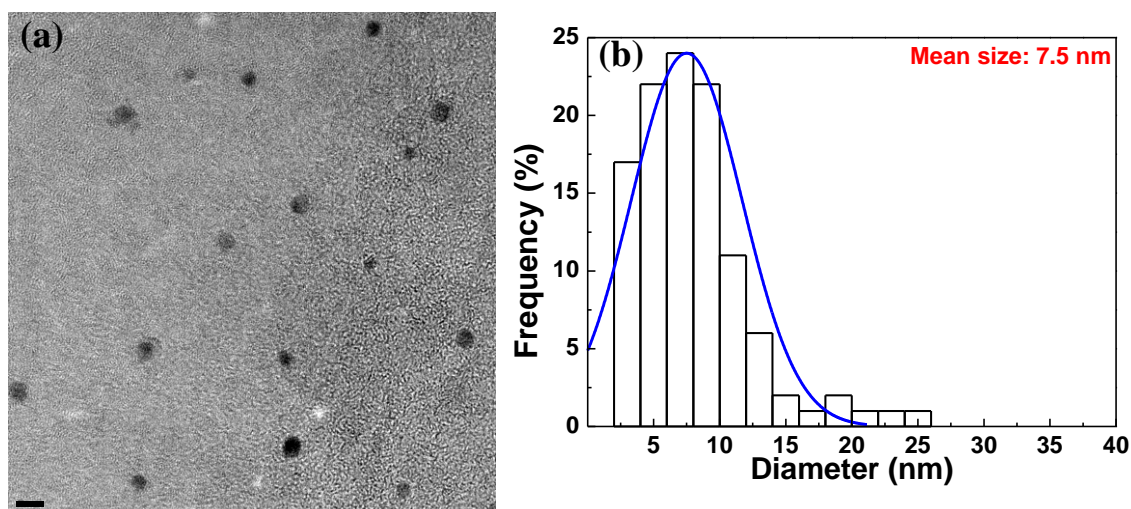
Figure 6. (a) TEM images of C_{60} clusters and (b) relevant size distribution.

In conclusion, an optimum CVD reaction condition has been confirmed: 950℃ with a t/w ratio of 1:3 within the fabrication procedure of colloidal aqueous C_{60} solution because of the uniformity of as-grown SWCNTs.

Because the present CVD is metal-catalyst free process, we can expect metal-impurity free products. Figure 8 shows TGA curve of as-grown sample synthesized at 950℃ with colloidal C_{60} solution of t/w = 1:3. As shown in the figure, the TGA curve shows steep decrease at ca. 500℃ and reaches zero at ca. 575℃, which explicitly demonstrates that the sample contains no metal residue. In addition, we have performed elemental analysis using energy dispersive X-ray analysis (EDX) and electron energy loss spectroscopy (EELS). Figure 9a shows a TEM image of as-grown sample, where many CNT bundles coming from a bulk black object can be seen. The corresponding EDX spectrum (Fig. 9b) shows peaks originating only from C, N, O, Cl and Si; O, Cl, N and Si mainly arise from H_2O/EtOH, 1,2-dichroloethane used to disperse the sample and Si_3N_4 TEM grid, respectively. Figure 9c-d show corresponding EELS spectra, where core-loss peaks originating from C is dominant. Peaks arising

from transition metal is negligible that is consistent to EDX results. The TGA, EDX and EELS results shown here clearly demonstrate that the products synthesized using the present C_{60}-mist-flow method is metal-free SWCNTs. Identical results can be also obtained using copper TEM grid of same sample (Figure 10).
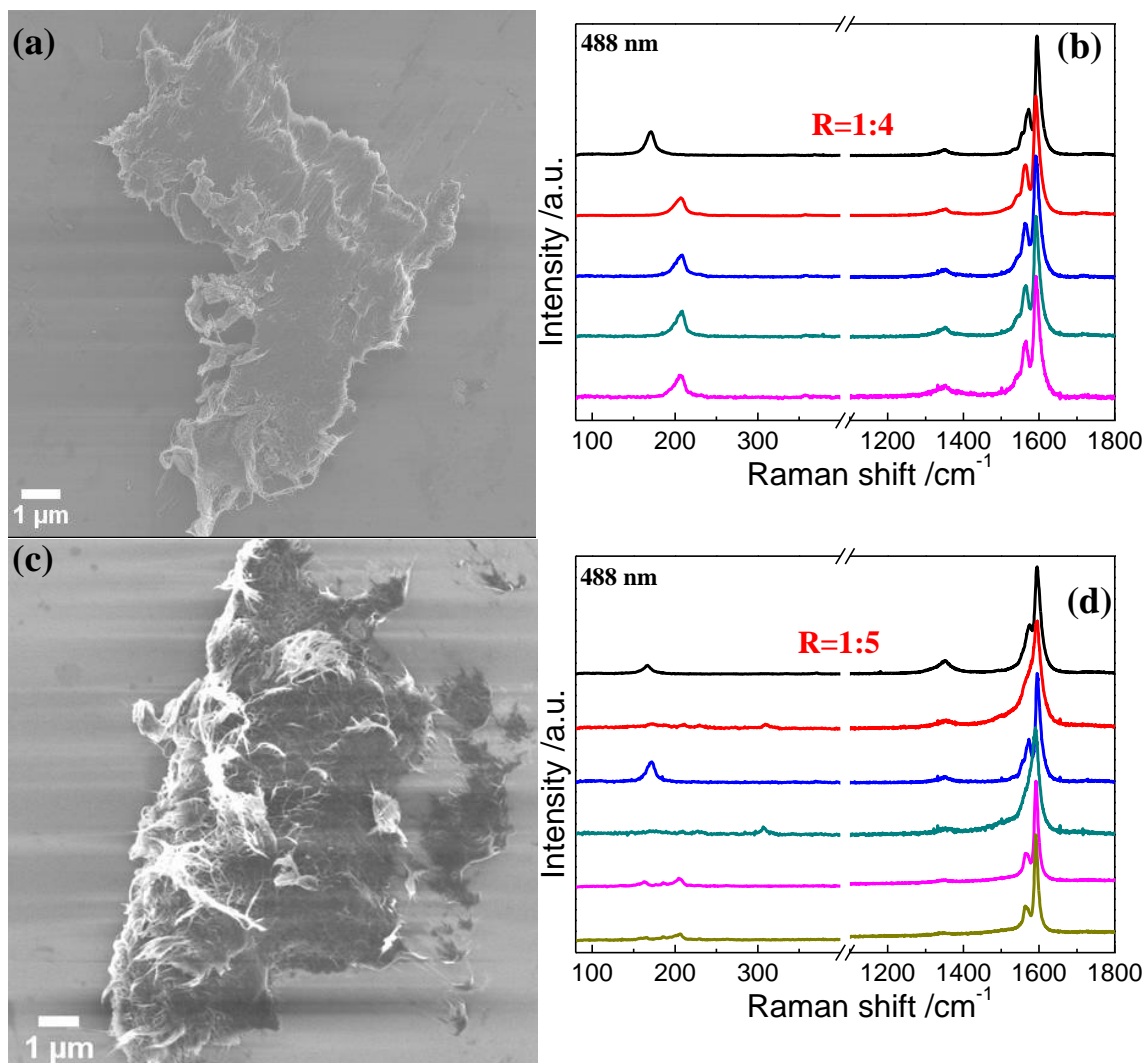

Figure 7. SEM images and corresponding Raman spectra measured by 488 nm excitation laser wavelength with (a,b) *t/w* ratio = 1:4 and (c,d) *t/w* ratio = 1:5, respectively.
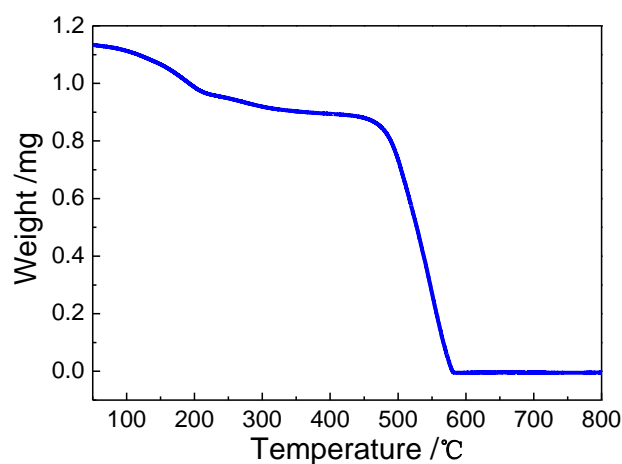
Figure 8. TGA profile of as-grown products at a heating rate 2 ℃/min in air (10 mL/min) investigates that as-grown products consist of only carbon material.
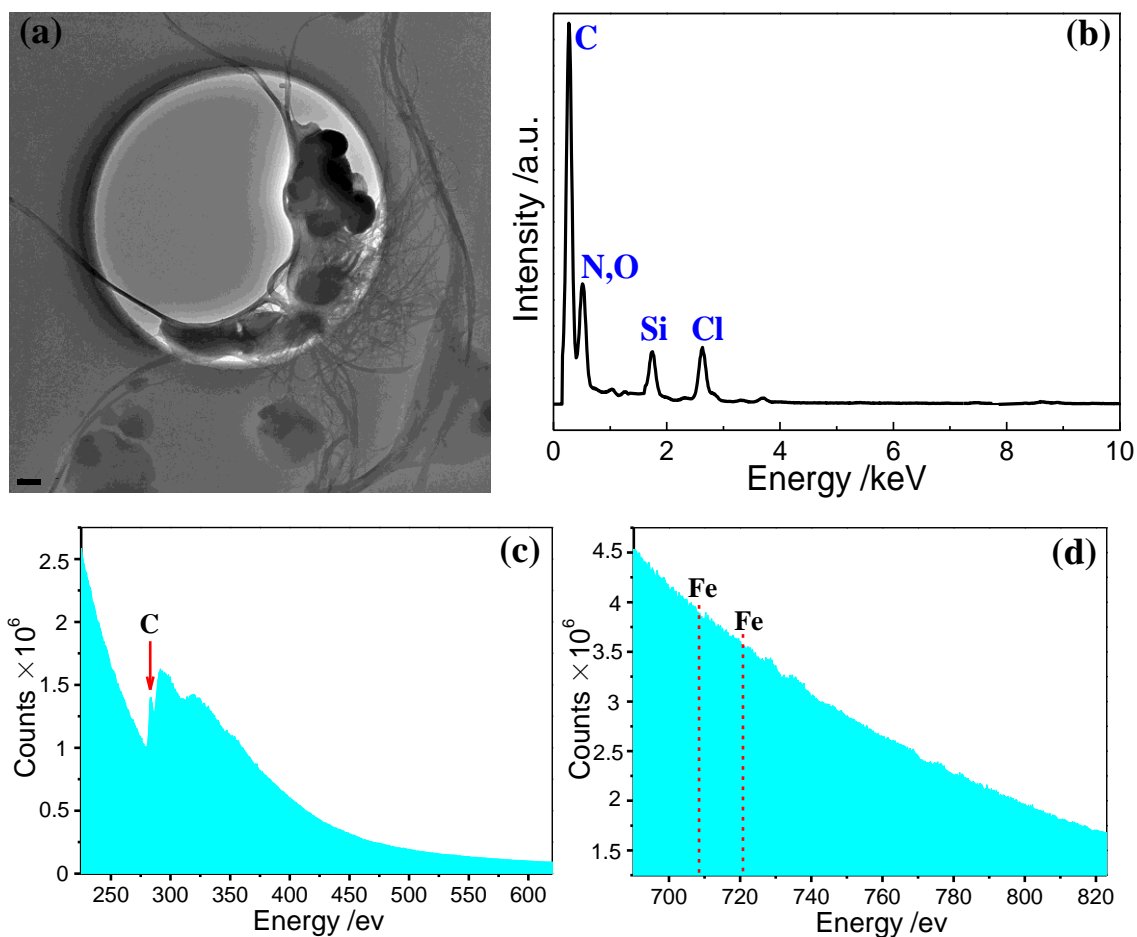

Figure 9. (a) Representative TEM image of a bulk black object in a Si₃N₄ TEM grid; (b) corresponding EDX profile measured in the center and (c,d) EELS spectrum within different energy.
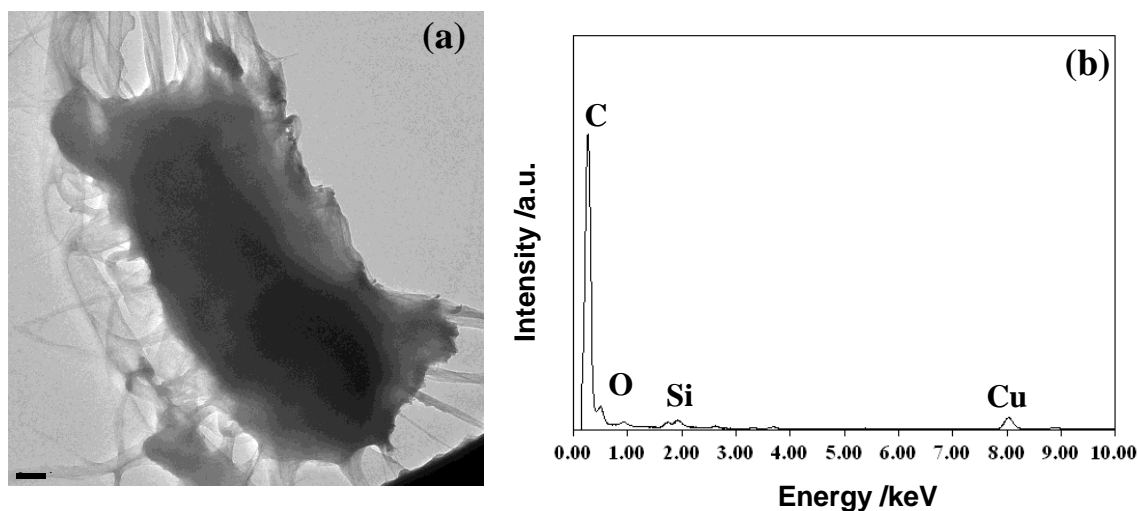
Figure 10. (a) Representative TEM image of a bulk black object in a copper TEM grid and (b) corresponding EDX profile measured in the center: Si arises from the Si substrate for collecting the as-grown products and Cu arises from the copper TEM grid.

3.3.2 The role of C_{60} and H_2O within the potential growth mechanism

In order to find out what is the role of C_{60} fullerenes during CVD, a blank experiment (no C_{60} used in the original solution) has been carried out under the same optimum CVD reaction condition. Although EtOH was used as a carbon source in this blank experiment, no CNTs were detected in Raman spectra and SEM images of resulting samples, which demonstrates that C_{60} plays an essential role in the growth of CNTs. Because of the decomposition of H_2O and ethanol molecules at high temperature, there are large amount of radicals in the CVD chamber, such as O-H and C-OH, during the CVD reactions. These kinds of reactive species can etch the C_{60} molecules to form open capped structures; for example, theoretical works have suggested that OH radicals attack C_{60} molecules to introduce epoxy groups leading to opening and activating C_{60} molecules into cap structures [22]. It is reported that open-cap structures can be a seed to grow CNTs, and the open caps formed by the etching reaction thus leads to the formation of CNTs. Because open-cap-mediate growth of CNTs is a metal-catalyst free

process, we can expect a metal-free product, which is consistent with the results shown in Figure 9. Frankly, what is the exact structure of this bulk black object is unknown, but we are sure it belongs to some kind of carbon material according to the aforementioned results of TGA, EDX and EELS (Figure 9b-d). Furthermore, due to the relatively low yield of as-grown products, large amount of amorphous carbon and other kind of carbon materials could have been also formed accompanied with the formation of active C_{60} caps during CVD process covering those "seed" C_{60} caps resulting in the formation of this black object.

If the open-cap-mediate growth occurs, synthesized SWCNTs are expected to possess closed-cap structures. Figure 11 and 12 show typical HRTEM images of tip structures of as-grown individual SWCNTs and bundles. As clearly shown in the images, tips of SWCNTs are closed by cap structures, which is consistent with the open-cap-mediate growth mechanism. In addition, we can see that the edge of each individual SWCNT within a bundle as shown in figures is almost close-end. According to the works of E. I. Kauppinen *et al*. [36], it is quite easy for the individual SWCNTs to form bundles due to their spontaneous charging in a gas-phase CVD synthesis. They found the CNTs were approximately equally positively and negatively charged during floating CVD process. So in our case, after the growth termination caused by the coalescence of cap structures with the edge of each individual SWCNT, these close-end SWCNTs will have an inter-attraction with each other to form bundles and at the same time their roots in the other edges should also aggregate together.

Indeed, there could be another situation. As shown in Figure 11c, it seems that the edge of this bundle is enveloped with a big cap. Because of the thermal oxidation and the growth of CNTs happening together in the CVD chamber within a very short
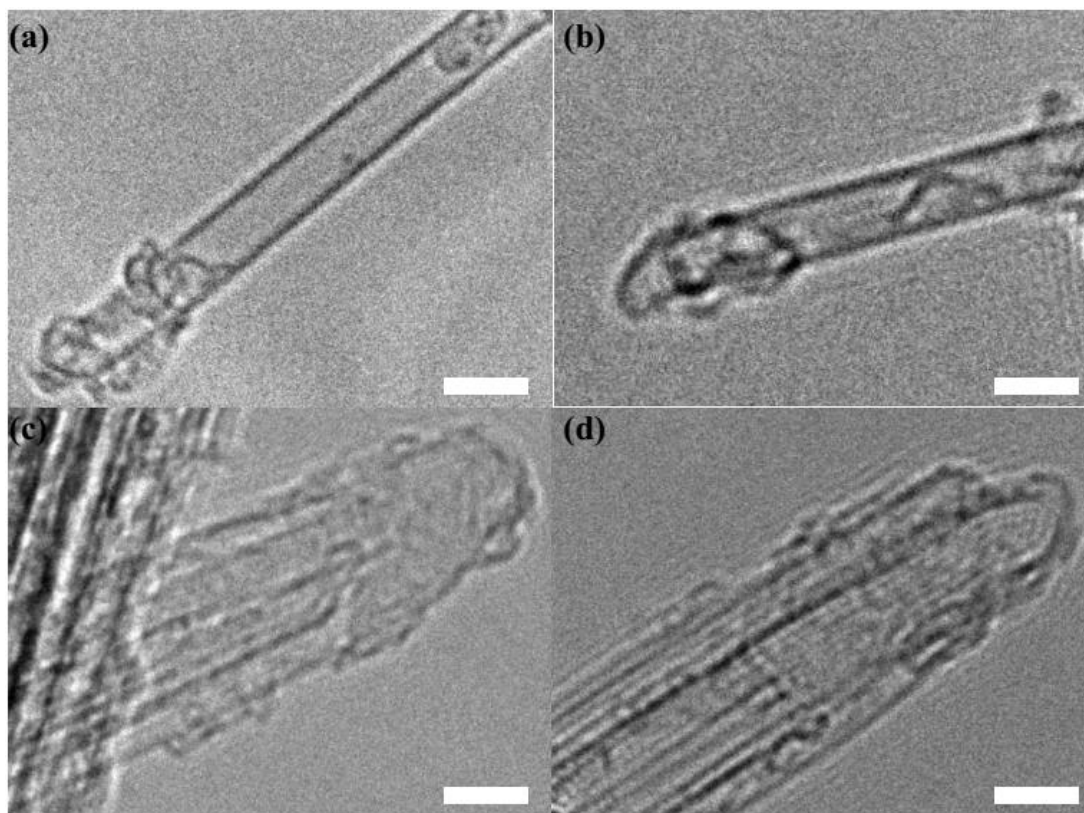
Figure 11. HRTEM images of as-grown (a.b) individual SWCNTs and (c,d) bundles have revealed the potential growth mechanism. The scale bar is 2 nm.

residence time, perhaps it is too late for some different size C_{60} caps to coalesce into an integral cap (the coalescence is not complete) so that it seems that there are several "roots" inside a big cap leading to the formation of bundles. Of course, this is statistically less favorable and explains why the most bundles consist of a few individual close-end SWCNTs. Figure 13 and 14 provides a schematic illustrating the potential growth mechanism involved in the C_{60} cap formation and subsequent SWCNT/bundle growth.

In addition, due to the almost same diameter and structure with C_{60} indeed, we have also tried to utilize C_{70} aqueous colloidal solution (the same procedure of
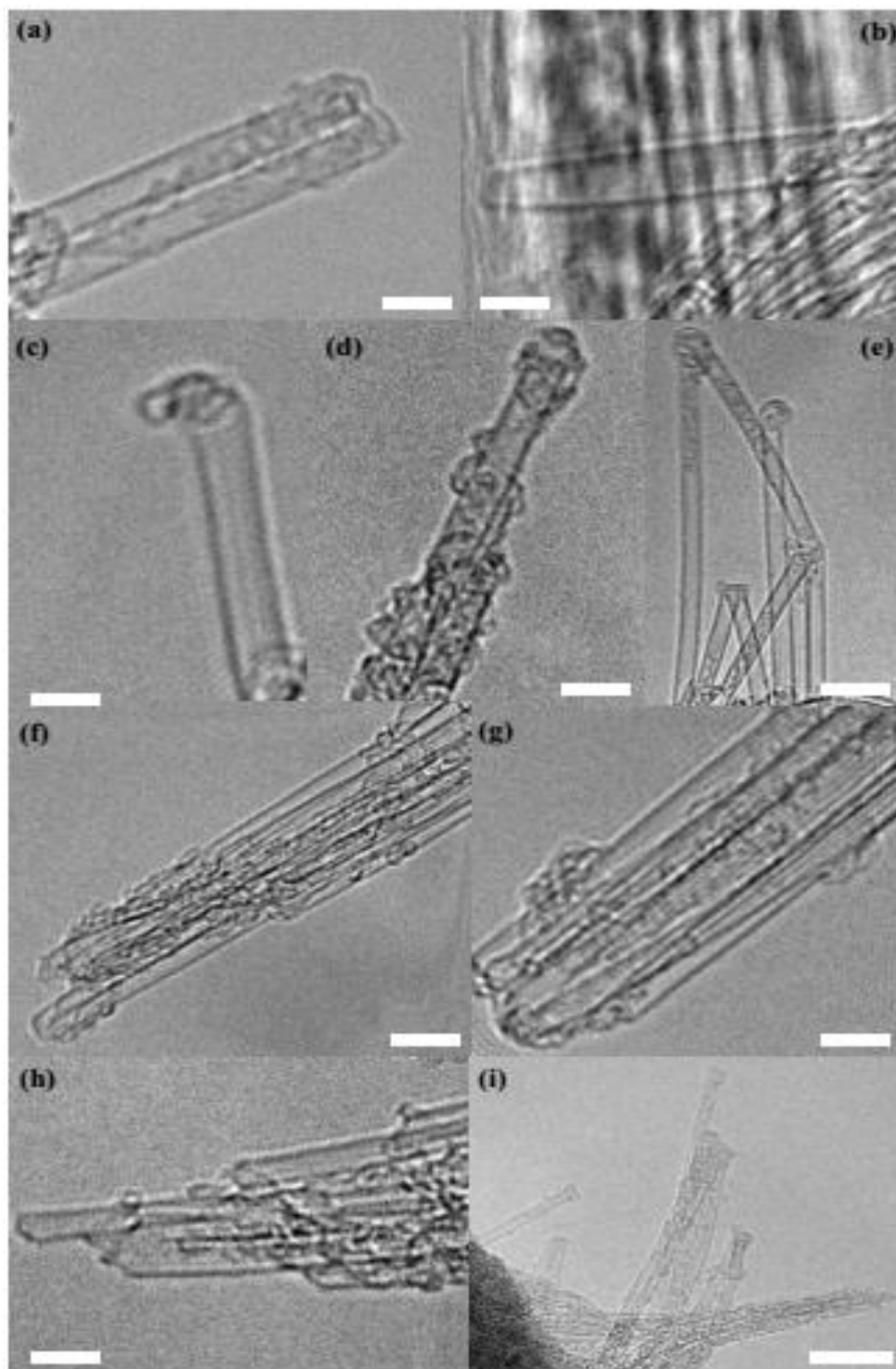
Figure 12. Some other relevant HRTEM images of as-grown individual SWCNTs and bundles on the tip section exposed the potential growth mechanism. The scale bar of (a) ~ (h) is 2 nm and (i) is 5 nm, respectively.
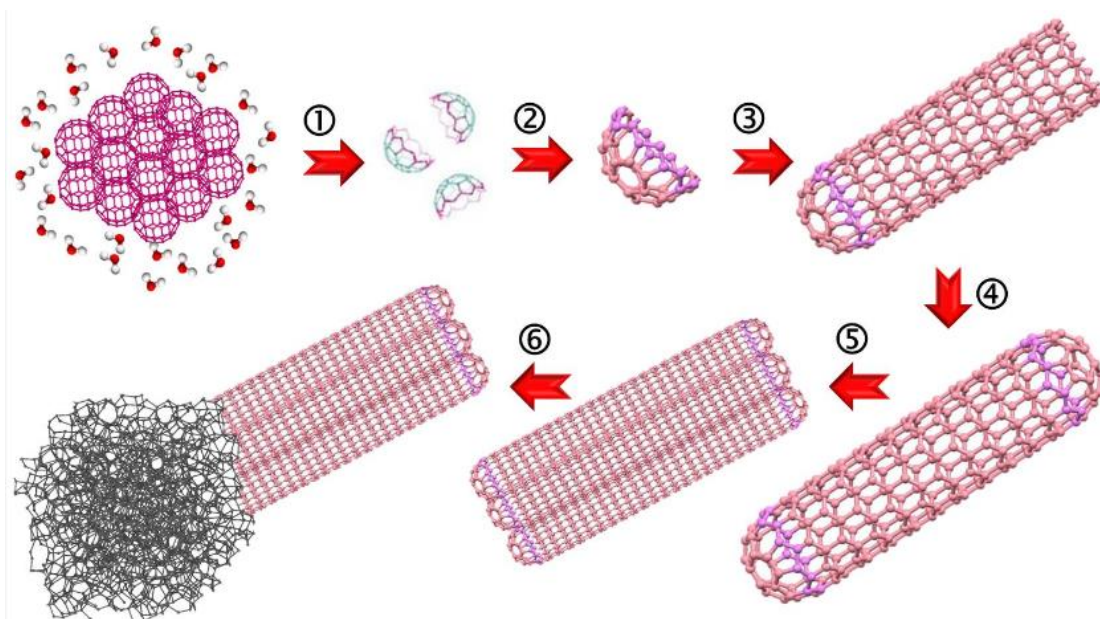
Figure 13. The schematic of potential growth mechanism of SWCNTs from aqueous colloidal C_{60} solution. ① C_{60} caps formation; ② The coalescence of cap structures into a larger one due to the thermal oxidation; ③ The growth of SWCNT; ④ The reaction between the open-end SWCNT and cap to form the close-end tube; ⑤ The formation of bundles because of the spontaneous charging; ⑥ C_{60} roots was covered with amorphous carbon and other kind of carbon material.
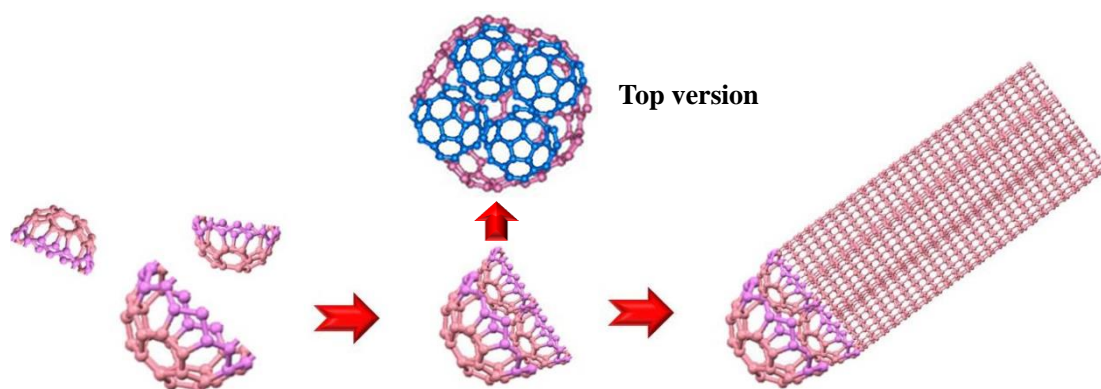

Figure 14. The scheme of the growth of bundles from a fragmentary cap.

fabricating C_{60} aqueous colloidal solution) to synthesize CNTs with mist flow CVD at the same optimum reaction condition. Figure 15a is the optical absorption spectra of C_{60}

and C_{70} colloidal solution, respectively. It is explicit that the absorption peaks of C_{70} colloidal solution are much lower than that of C_{60} due to the low solubility of C_{70} in the same amount of toluene compared to C_{60}, which can lead to the reduction of aqueous water-fullerene molecules in the colloidal solution. In addition, the position and shape of each absorption peaks between C_{60} and C_{70} colloidal solution are totally different, which means the structure of each water-fullerene molecule within the corresponding colloidal solution might be different [37]. Figure 15b is the Raman spectra of as-grown products synthesized from C_{70} aqueous colloidal solution as the different flow rate. However, unfortunately there are no CNTs synthesized at 300 sccm (the same optimum reaction condition of C_{60}) because no RBM peaks have been detected because of the low solubility of C_{70} in toluene compared with C_{60} leading to the inadequate C_{70} seeds during CVD process. Therefore, I have increased the flow rate up to 600 sccm in order to increase the amount the C_{70} molecules within the same residence time. As a result, a tiny RBM peak has been found. Compared to the Raman spectrum of the pristine C_{70}, it
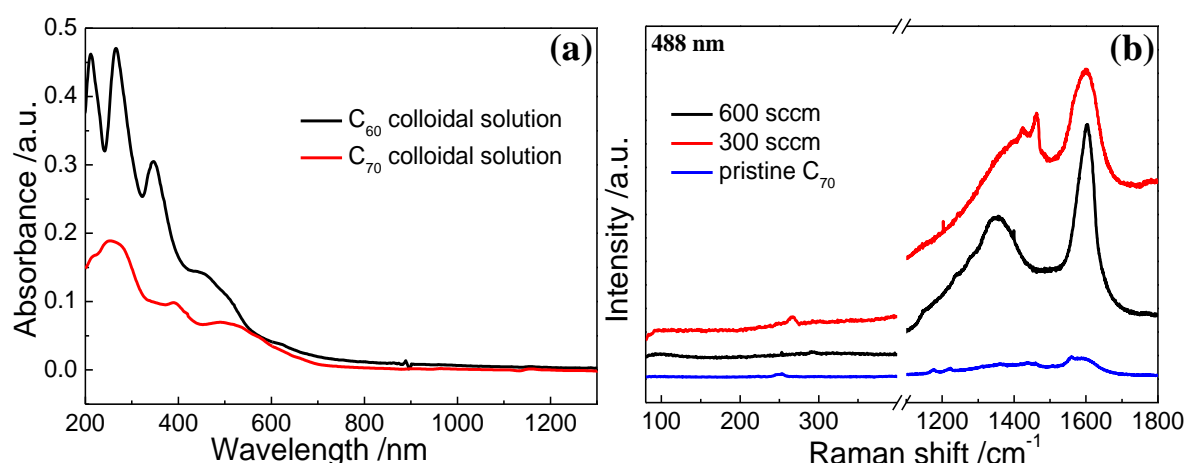

Figure 15. (a) UV-vis-NIR spectrum of C_{60} and C_{70} colloidal solution in water; (b) Raman spectra of as-grown products synthesized from C70 aqueous colloidal solution at different flow rate and pristine C_{70}.
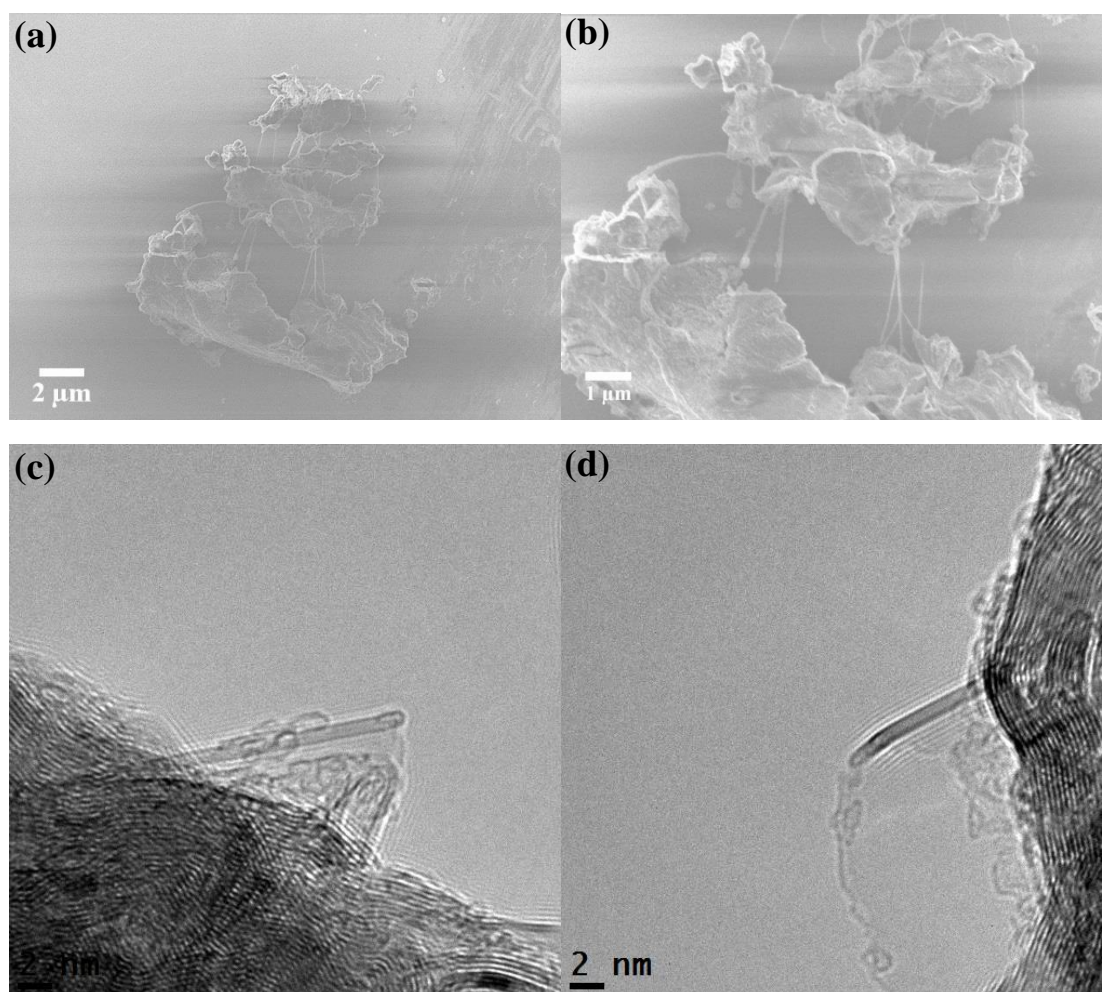
Figure 16. (a-b) SEM (c-d) HRTEM images of as-grown products synthesized at the flow rate of 600 sccm from C_{70} aqueous colloidal solution.

is not from C_{70} and there is a possibility that it comes from CNT or some other carbon material with the tubular structure due to the strange G band, which can be also proved with the SEM images of the same sample. As shown in Figure 16a-b, we can fine some nanotube-like materials clearly. To confirm what they are exactly, TEM observation has been applied. From the corresponding HRTEM images (Figure 16c-d), even though several nanotubes have been observed with a diameter around 0.8 nm, the evidences are inadequate due to the extremely low yield. In addition to the unnatural Raman spectra of

as-grown products, it is too difficult to prove the growth of CNTs from C_{70} aqueous colloidal solution. Much more efforts need to be contributed in the future.

3.4 Conclusions

In summary, a one-step catalyst-free mist flow CVD growth of SWCNTs with C_{60} fullerenes has been investigated with the help of an aqueous colloidal C_{60} solution consisting of the water and C_{60} fullerenes. Thanks to the water, opening cap, activation, nucleation and growing uniform SWCNTs can happen simultaneously in the CVD chamber using C_{60} as the seed, which could simplify the experimental steps and decrease the loss of C_{60} opened-caps compared with CCVD technique. Plenty of close-end individual SWCNTs with cap structures have been found proving the existence of open-cap-mediate growth. C_{60} fullerenes can be considered as the seed for providing the caps and the water should contribute to etching C_{60} into caps and supplying the oxygen, which could lead to the coalescence of C_{60} caps into a larger one for the growth of larger diameter SWCNTs. This can also explain why the diameter of as-grown SWCNTs (1.0 ~ 1.8 nm) is bigger than that of an individual C_{60}. Meanwhile, due to the spontaneous charging in a gas-phase CVD synthesis, some close-end SWCNTs would like to aggregate to form bundles covered with some amorphous carbon and other kinds of carbon materials, which are formed accompanied with the formation of active C_{60} caps during CVD process, leading to a kind of unknown carbon object. Furthermore, we realize that perhaps the diameter of as-grown SWCNTs can be controlled via tuning the amount of water, which would have pointed out an inspirational direction for the one-step controllable growth of SWCNTs in a floating CVD system in the future. In addition, we also contribute to attempting C_{70} aqueous

colloidal solution to synthesize CNTs. Nevertheless, although C_{70} fullerenes possess the similar diameter and structure with C_{60}, we cannot obtain the adequate positive evidences to prove the growth of CNTs possibly due to the low solubility of C_{70} in the same amount of toluene compared to C_{60} leading to the reduction of aqueous C_{70} clusters in the colloidal solution and the formation of different structures.

References

1. Hayamizu, Y.; Yamada, T.; Mizuno, K.; Davis. R. C.; Futaba, D. N.; Yumura, M. Nat. Nanotechnol. 2000, 3, 289-294.

2. Kong, J.; Franklin, N. R.; Zhou, C.; Chapline, M. G.; Peng, S.; Cho, K. Science 2000, 287, 622-625.

3. Zhang, D.; Ryu, K.; Liu, X.; Polikarpov, E.; Ly, J.; Tompson, M. E. Nano Lett. 2006, 6, 1880-1886.

4. Artukovic, E.; Kaempgen, M.; Hecht, D. S.; Roth, S.; Grüner, G. Nano Lett. 2005, 5, 757-760.

5. Futaba, D. N.; Hata, K.; Yamada, T.; Hiraoka, T.; Hayamizu, Y.; Kakudate, Y. Nat. Mater. 2006, 5, 987-994.

6. Ebbesen, T. W.; Ajayan, P. M. Nature 1992, 358, 220-222.

7. Thess, A.; Lee, R.; Nikolaev, P.; Dai, H.; Petit, P.; Robert, J. Science 1996, 273, 483-487.

8. Li, W. Z.; Xie, S. S.; Qian, L. X.; Chang, B. H.; Zou, B. S.; Zhou, W. Y. Science 1996, 274, 1701-1703.

9. Brukh, R.; Sae-Khow, O.; Mitra, S. Chem. Phys. Lett. 2008, 459, 149-152.

10. Nel, A.; Xia, T.; Mädler, L.; Li, N. Science 2006, 311, 622-627.

11. Liu, H. P.; Takagi, D.; Ohno, H.; Chiashi, S.; Chokan, T.; Homma, Y. Appl. Phys. Express 2008, 1:014001.

12. Liu, B.; Ren, W.; Gao, L.; Li, S.; Pei, S.; Liu, C. J. Am. Chem. Soc. 2009, 31, 2082-2083.

13. Huang, S.; Cai, Q.; Chen, J.; Qian, Y.; Zhang, L. J. Am. Chem. Soc. 2009, 131, 2094-2095.

14. Derycke, V.; Martel, R.; Radosavljević, M.; Ross, F. M.; Avouris, P. H. Nano Lett. 2002, 2, 1043-106.

15. Koshio, A.; Yudasaka, M.; Iijima, S. Chem. Phys. Lett. 2002, 356, 595-600.

16. Jin, C. H.; Suenaga, K.; Iijima, S. ACS Nano 2008, 2, 1275-1279.

17. Liu, H. P.; Takagi, D.; Chiashi, S.; Homma, Y. Carbon 2010, 48, 114-122.

18. Rao, F.; Li, T.; Wang, Y. L. Carbon 2009, 47, 3574-3584.

19. Yao, Y. G.; Feng, C. Q.; Zhang, J.; Liu, Z. F. Nano Lett. 2009, 9, 1673-1677.

20. Liu, J.; Wang, C.; Tu, X. M.; Liu, B. L.; Chen, L.; Zheng, M.; Zhou. C. W. Nat. Commun. 2012, 3, 1-7.

21. Yu, X. C.; Zhang, J.; Choi, W. M.; Choi, Jae-Y.; Kim, J. M.; Gan, L. B.; Liu, Z. F. Nano Lett. 2010, 10, 3343-3349.

22. Ibahim, I.; Bachmatiuk, A.; Grimm, D.; Popov, A.; Makharza, S.; Knupfer, M.;

Büchner, B.; Cuniberti, G.; Rümmeli, M. H. ACS Nano 2012, 6, 10825-10834.

23. T. Hiraoka, S. Bandow, H. Shinohara and S. Iijima, Carbon 44, 1853 (2006).

24. G. Hong, Y. B. Chen, P. Li and J. Zhang, Carbon 50, 2067 (2012).

25. Y. Tian, M. Y. Timmermans, M. Partanen, A. G. Nasibulin, H. Jiang, Z. Zhu and E. I. Kauppinen, Carbon 49, 4636 (2011).

26. Y. Tian, A. G. Nasibulin, B. Aitchison, T. Nikitin, J. Pfaler, H. Jiang, Z. Zhu, L. Khriachtchev, D. P. Brown and E. I. Kauppinen, J. Phys. Chem. C 115, 7309 (2011).

27. Andrievsky, G. V.; Klochkov, V. K.; Karyakina, E. L.; M-Petrossyan, N. O. Chem. Phys. Lett. 1999, 300, 392-396.

28. Andrievsky, G. V.; Kosevich, M. V.; Vovk, O. M.; Shelkovsky, V. S.; Vashchenko, L.A. J. Chem. Soc., Chem. Commun. 1995, 12, 1281.

29. Sun. Y.; Kitaura, R.; Nakayama, T.; Miyata, Y.; Shinohara, H. NANO 2012, 7, 1250045-1 (10).

30. Lin, J. H.; Chen, C. S.; Rümmeli, M. H.; Zeng, Z. Y. Nanoscale 2010, 2, 2835-2840.

31. Lin, J. H.; Chen, C. S.; Rümmeli, M. R.; Bachmatiuk, A.; Zeng, Z. Y.; Ma, H. L.; Büchner, B.; Chen, C. W. Chem. Mater. 2011, 23, 1637-1639.

32. Rümmeli, M. H.; Borowiak-Palen, E.; Gemming, T.; Pichler, T.; Knupfer, M.; Kalbac, M.; Dunsch, L.; Jost, O.; Silva, S. R. P.; Pompe, W.; et al. Nano Lett. 2005, 5, 1209-1215.

33. Rümmeli, M. H.; Schäffel, F.; Kramberger, C.; Gemming, T.; Bachmatiuk, A.; Kalenczuk, R. J.; Rellinghaus, B.; Büchner, B.; Pichler, T. J. Am. Chem Soc. 2007, 129, 15772-15773.

34. Kumar, M.; Ando, Y. J. Nanosci. Nanotechnol. 2010, 10, 3739-3758.

35. Adelene Nisha, J.; Sridharan, V.; Janaki, J.; Hariharan, Y.; Sastry, V. S.; Sundar, C. S.; Radhakrishnan, T. S. J. Phys. Chem. 1996, 100, 4503-4506.

36. Gonzalez, D.; Nasibulin, A. G.; Shandakov, S. D.; Jiang, H.; Queipo, P.; Anisimov, A. S.; Tsuneta, T.; Kauppinen, E. I. Chem. Mater. 2006, 18, 5052-5057.

37. Deguchi, S.; Alargova, R. G.; Tsujii, K. Langmuir 2001, 17, 6013-6017.

Chapter 4

The Fabrication of Thin Single-Wall Carbon Nanotubes from Fe_{18} Clusters using Mist Flow CVD

4.1 Introduction

The extraordinary electronic, thermal and mechanical properties of carbon nanotubes (CNTs), especially single-walled carbon nanotubes (SWCNTs), are closely bound up with their diameter and chirality. The seeking for thin SWCNTs is significant for taking advantage of the size influence that is predicted to lead to the different properties from those for larger nanotubes [1-2]. An important property of a thin (semiconducting) SWCNT, used for electronic devices [3-4], is its band gap energy, which also determines the electrical properties of the device. A semiconducting carbon nanotube's band gap energy is typically on the order of 0.5ev, which is low compared to over 1ev band gap of common semiconductors. Thus, due to inverse proportionality of semiconducting nanotubes' band gap to their diameter, synthesis of thin diameter SWCNTs is desired for many nanoelectronic applications such as carbon nanotube field effect transistors (CNTFETs) [5-6]. Some studies have been reported about the synthesis of thin SWCNTs [7-9]. Some of them concentrated on the innermost cylinder of a MWCNT [7-8] and the other one [9] left a margin for argument [10-11]. In particular, the zeolite-supported CVD and HiPco process are well-known for their ability to fabricate thin SWCNTs [12-18]. However, the procedure of zeolite-supported CVD is

complicated and trivial including the mixture of zeolite templates and catalyst particles as well as the pretreatment in the air. Due to the discontinuity, it's too hard to synthesize thin SWCNTs in mass. Although HiPco process is continuous for producing thin SWCNTs, the high pressure is necessary resulting in the increase of danger and difficulty. Therefore, a simple, convenient and effective technique for the fabrication of thin SWCNTs under the atmosphere is desirable at present.

In contrast to the catalysts-supported CVD, the floating catalyst CVD is capable of continuously synthesizing SWCNTs from the gas phase onto a substrate by simultaneously supplying the catalyst precursor and carbon source [19-28]. The mist flow CVD has been proved to be available for the low-cost, facile and scalable production of SWCNTs under the atmosphere [29]. Here an investigation about the fabrication and characterization of thin SWCNTs from Fe_{18} clusters by means of mist flow CVD has been proposed. Because Fe_{18} cluster is a novel catalyst precursor, an investigation about what is its favorite solvent has been also carried out. As a result, we find that choosing the right solvent can lead to the growth of very thin SWCNTs (the mean diameter is 0.8 nm). And this could have pointed out a new direction for the fabrication of thin SWCNTs in a floating CVD system.

4.2 Experimental section

4.2.1 Preparation of $Fe_{18}C_{114}H_{206}N_{12}O_{106}$ crystals [30]

As shown in Figure 1, $Fe(NO_3)_3$ $9H_2O$ (0.081g) was added to a stirred solution of sodium benzoate $(Na(C_6H_5)CO_2$, 0.029 g) in pdH_2 (1,3 propanediol) / MeCN (3 mL/20 mL). The yellow solution was stirred for 10 min further and filtered; subsequently, the filtrate was layered with Et_2O (ethyl ether). After one day or longer, some yellow

crystals had precipitated and were collected by filtration, washed with MeCN and dried

in vacuum at 200℃ for 30 min. According to P. King *et al*. [30], the dried material is so

hygroscopic and was analyzed as $[Fe_{18}(O_2CPh)_6(pd)_{12}(pdH)_{12}(NO_3)_6]\cdot 10H_2O$
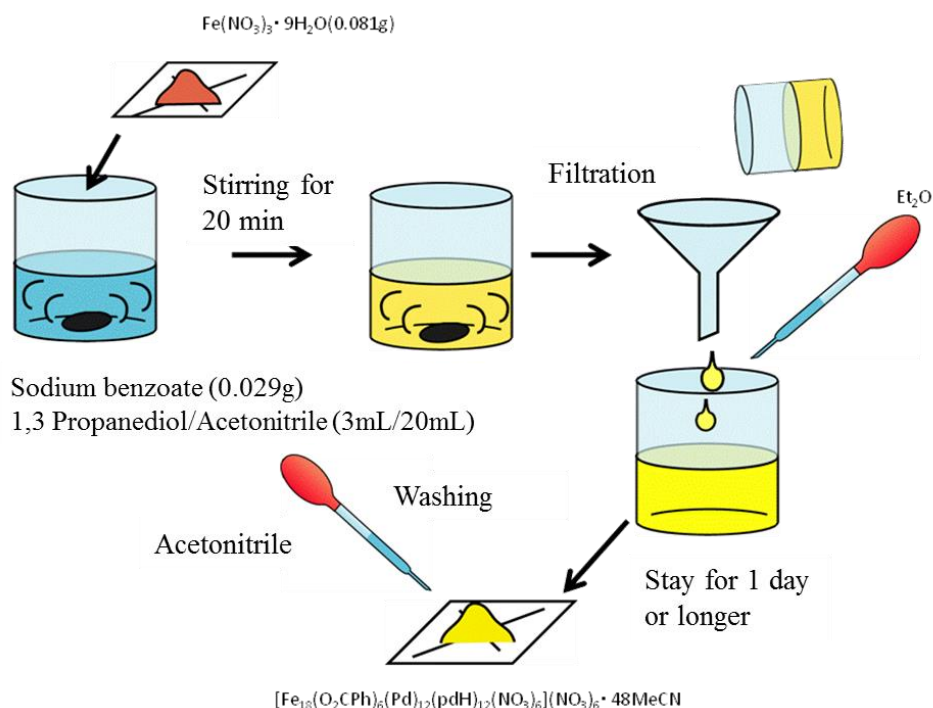
$(Fe_{18}C_{114}H_{206}N_{12}O_{106})$.

Figure 1. The scheme of the procedure of how to prepare Fe_{18} clusters.

4.2.2 Catalyst-supported CVD (CCVD) method

A spot of Fe_{18} solution was dropped onto the surface of silicon substrate (1 cm × 1

cm) followed by spin-coating under 4000 rpm for 1 min in order to generate the

equidistribution as much as possible. Subsequently, the substrate was annealed in the air

for 30 min and ready for the CVD reaction. After CVD, the surface of the substrate

would be measured by Raman spectroscopy and SEM to confirm whether there are

CNTs synthesized.

4.2.3 Mist flow CVD growth of SWCNTs using Fe_{18} clusters

At first, 15 ml mixed solution was transferred into a container attached with a mist generator and used for each CVD experiment. Prior to CVD, pure Ar of 1000 sccm was introduced into the CVD system for 15 min to eliminate all the air. After the anticipated temperature was stable, the mist generator was switched on and CVD reaction lasted for 15 min. The as-grown products collected by the substrate and transition electron microscopy (TEM) grid loaded at the bottom of the chamber were characterized by various measurements (Raman spectroscopy, TEM, SEM, etc.). More details about the mist flow CVD synthesis of SWCNTs has been described previously.

4.3 Results and Discussion

4.3.1 The particle size distribution of each mixed solution

In order to figure out which solvent is the favorite of Fe_{18} clusters, methanol, ethanol and MeCN have been investigated and used for dissolving the precipitated crystals, respectively. The atomic force microscopy (AFM) is one of the foremost tools for imaging, measuring, and manipulating matter at the nanoscale. According to Section 4.2.2, three Si substrates were spin-coated with methanol, ethanol and MeCN dissolved with Fe_{18} clusters, respectively. From the AFM images of the surface of each substrate (without annealing in the air) (Figure 2), it is explicit that the particle size is the best-distributed of choosing methanol as the carbon source, smallest of choosing MeCN as the carbon source and worst of choosing ethanol as the carbon source. This should give us a clue that perhaps the methanol is the favorite solvent for Fe_{18} clusters but not the most suitable due to the large particle size; whereas depending on the smallest particle size, MeCN could be the best one for the synthesis of thin SWCNTs from Fe_{18}
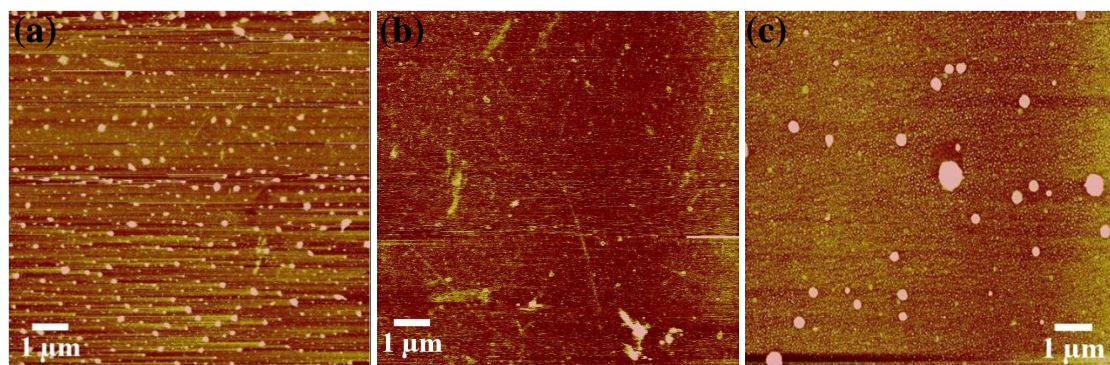
clusters by means of mist flow CVD.

Figure 2. AFM images of the surface of each substrate spin-coated with (a) methanol, (b) MeCN and (c) ethanol dissolved with Fe_{18} cluster, respectively.

4.3.2 Catalyst-supported CVD

Because of the smallest particle size as shown in Figure 2b, the substrate coated with Fe_{18} clusters dissolved in MeCN has been used for the synthesis of CNTs with CCVD technique. Table 1 is the four kinds of pretreatment and CVD reaction conditions applied for each CVD. According to the Raman spectra of as-grown products synthesized under condition ① (Figure 3a), it is explicit that there are typical characteristic G band and RBM peaks of CNTs with inhomogeneous diameter distribution, which can be also proved in the corresponding SEM images for the CNTs synthesized but with low yield (Figure 4a-b).

Table 1. Pretreatment and CCVD reaction conditions

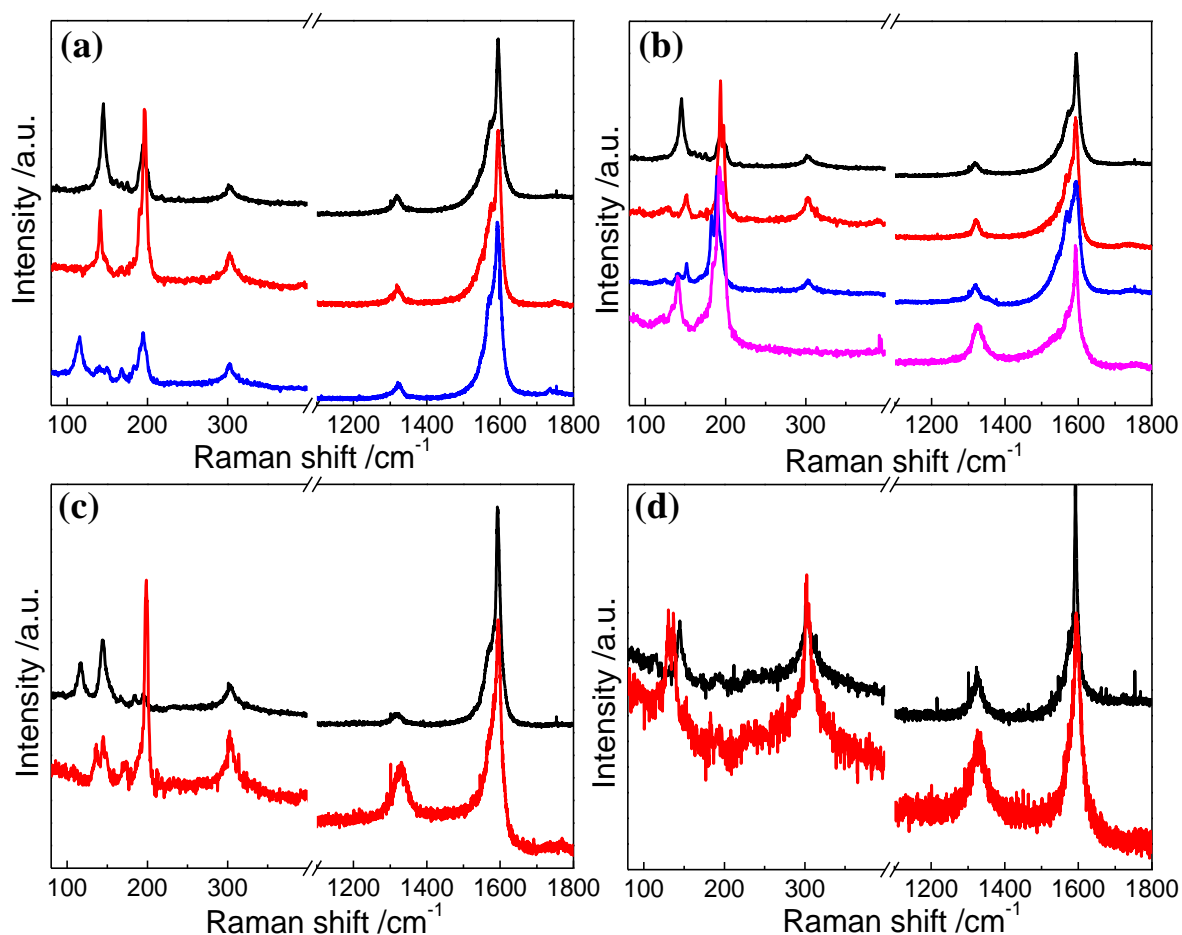| Pretreatment		Reaction temperature	Vacuum	Carrier gas	Flow rate	Reaction time
Temperature	Time					
① 500℃	30 min	900℃	√	Ar/H$_2$	100 sccm	30 min
② 500℃	30 min	950℃	√	Ar/H$_2$	100 sccm	30 min
③ 550℃	30 min	900℃	√	Ar/H$_2$	100 sccm	30 min
④ 550℃	30 min	950℃	√	Ar/H$_2$	100 sccm	30 min

Figure 3. Raman spectra of as-grown products synthesized under (a) condition ①, (b) condition ②, (c) condition ③ and (d) condition ④ measured by 633 laser excitation wavelength, respectively.

The explanations of these phenomena could be elaborated clearly through the corresponding HRTEM images. As shown in Figure 4c-d, although there are actually a few thin SWCNTs synthesized with the diameter around 1.0 nm, several MWCNTs have also been found within the products with a catalyst particle of larger size on the edge of an individual MWCNT. This should be because during the pretreatment procedure, the temperature may be too low (weak oxidation) to remove all the functional groups except Fe_{18} clusters, which could lead to the decrease of the amount and lifetime of catalyst particles as well as the low yield. In addition, the catalyst

particles can aggregate easily to form a larger one during the pretreatment and CVD process. As a result, MWCNTs are synthesized resulting in the inhomogeneous diameter distribution of as-grown products.
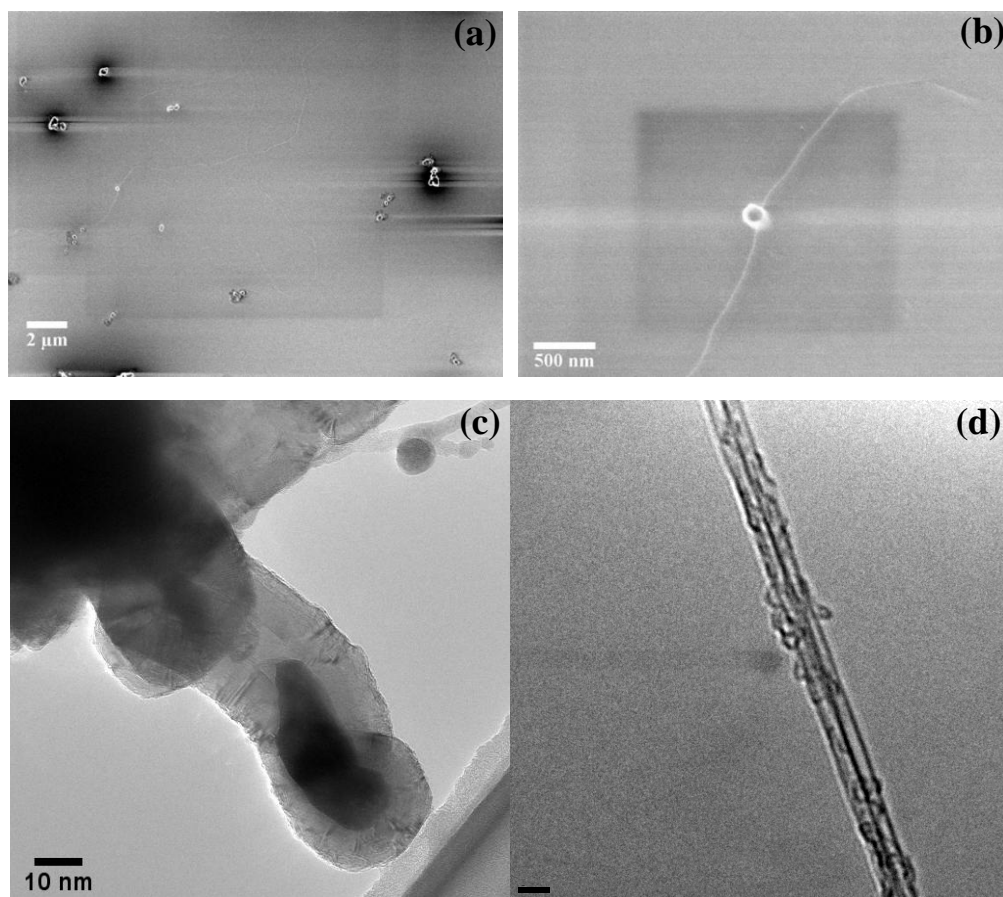

Figure 4. Corresponding (a-b) SEM and (c-d) HRTEM images of as-grown products synthesized under condition ①.

Secondly, as described in condition ②, the CVD reaction temperature has been raised to 950℃ while keeping the pretreatment temperature constant (500℃). As a result, there is no big difference about the diameter distribution of as-grown products compared with that synthesized at 900℃ according to the Raman spectra (Figure 3b) because of the as-synthesized MWCNTs (Figure 5c). However, from the corresponding

SEM (Figure 5a-b) and HRTEM images (Figure 5d) of as-grown products, it looks like the yield has been increased. So it seems that the CVD reaction temperature would have no big influence on the diameter of as-grown products using CCVD technique. So the pretreatment temperature has been studied then. Under condition ③, the pretreatment temperature has been raised to 550℃. As a result, from the SEM images (Figure 6a-b) we can see that the yield of as-grown products has been increased drastically, but there are still no obvious changes distinguished from the RBM peaks within Raman spectra (Figure 3c).
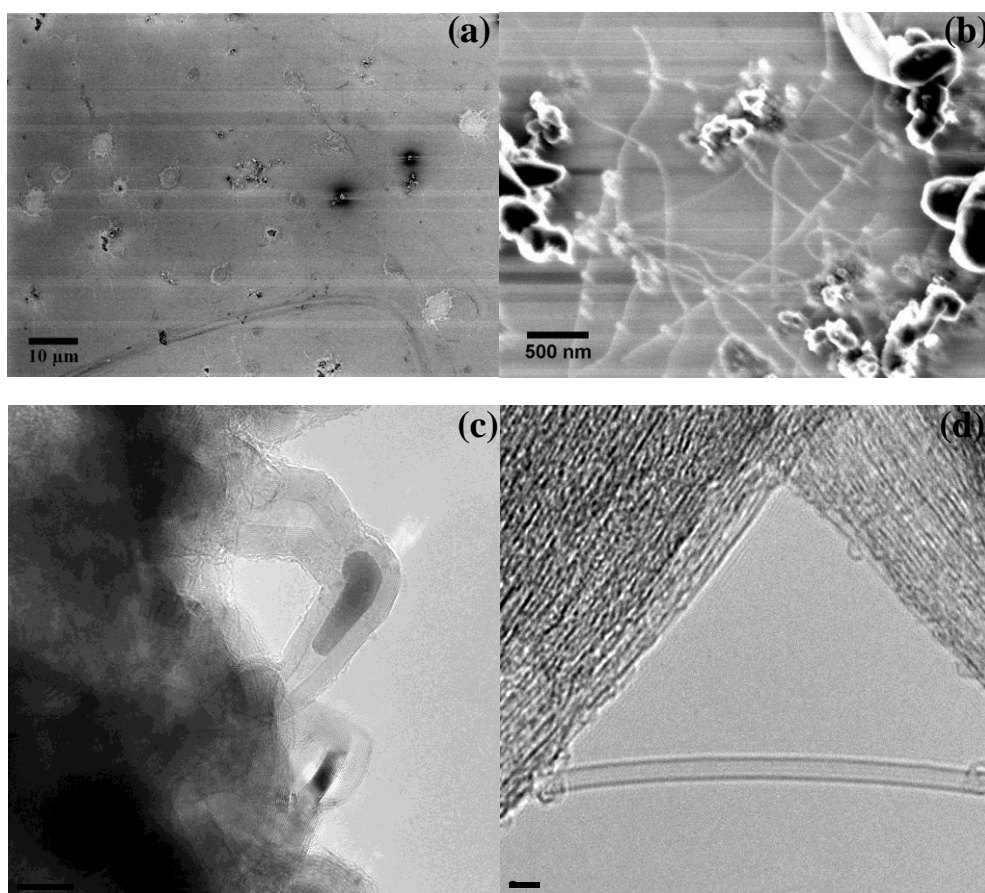

Figure 5. Corresponding (a-b) SEM and (c-d) HRTEM images of as-grown products synthesized under condition ②.

The reason why the yield has been increase should be that perhaps 550℃ is quite available to remove all the functional groups to form "naked" Fe_{18} clusters. Therefore, during CVD process, large amount of Fe_{18} clusters can contribute to the catalysts leading to the increase of the yield of as-grown CNTs. However, the aggregation of catalyst particles is still serious during either pretreatment or CVD process so that many larger size catalyst particles are formed resulting in the formation of not only SWCNTs, but also DWCNTs and MWCNTs, which is demonstrated clearly in the HRTEM images (Figure 6c-d).
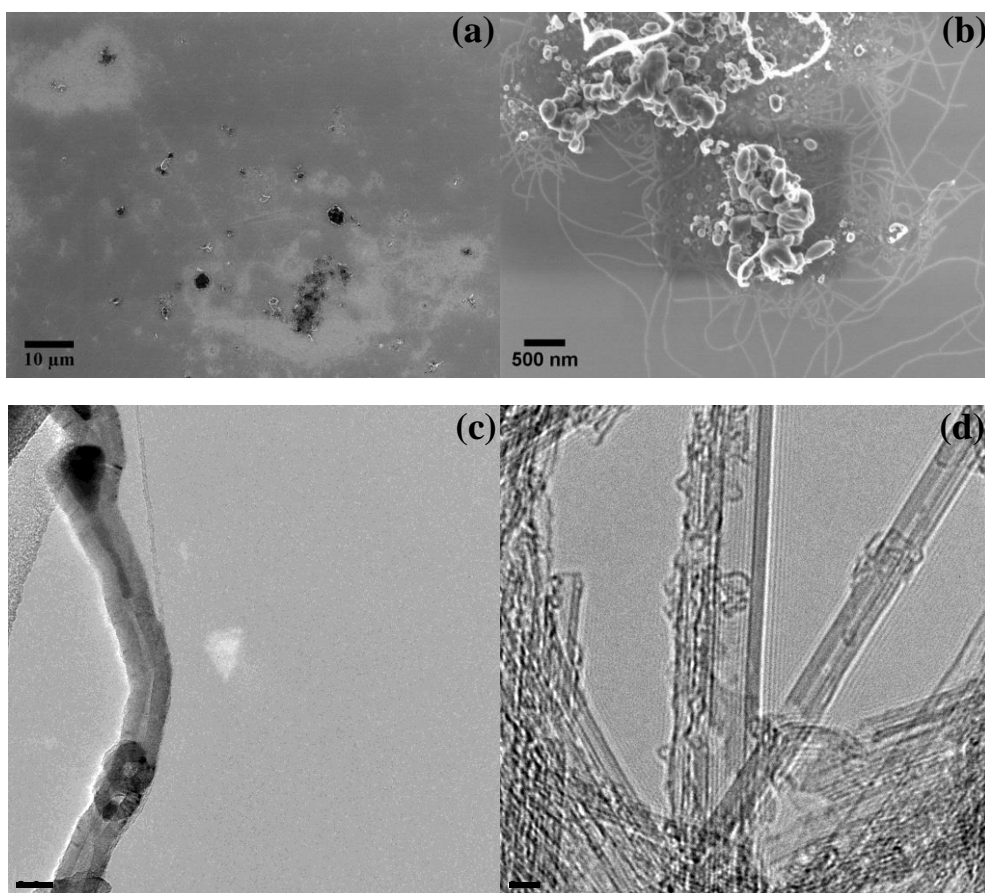

Figure 6. Corresponding (a-b) SEM and (c-d) HRTEM images of as-grown products synthesized under condition ③.
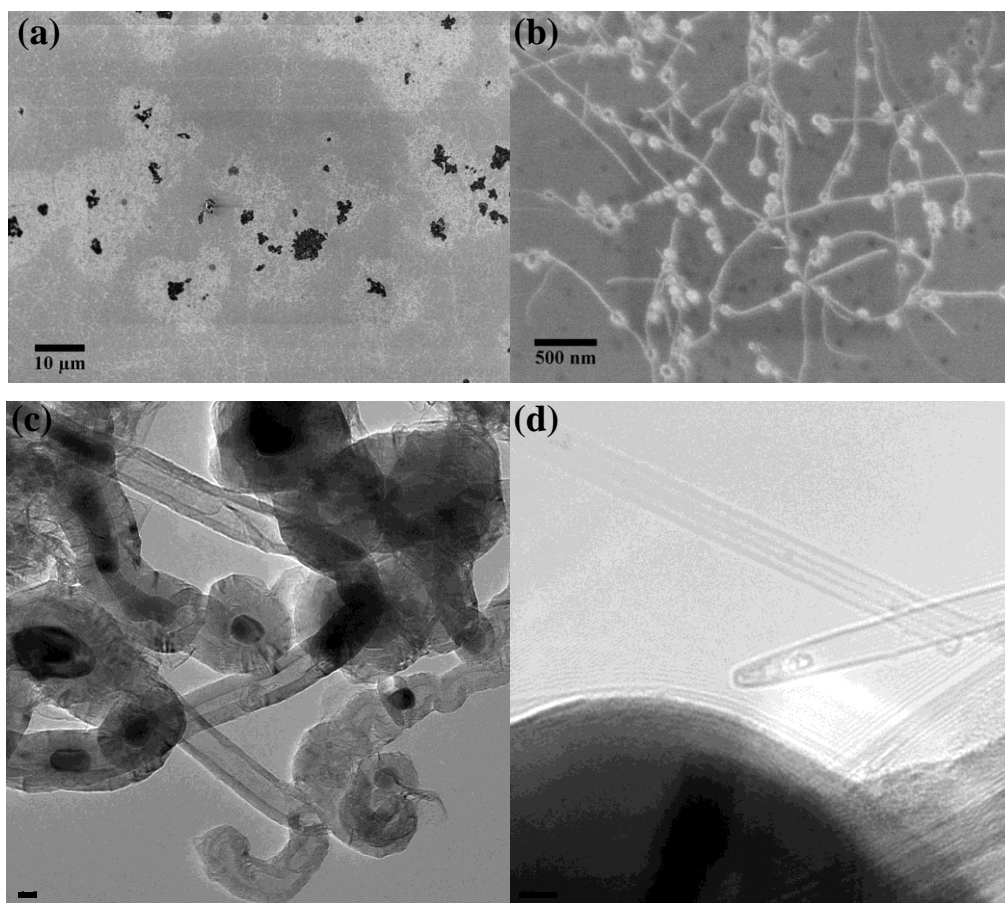
Figure 7. Corresponding (a-b) SEM and (c-d) HRTEM images of as-grown products synthesized under condition ④.

In the end, the CVD reaction temperature has also been raised to 950℃ while maintaining the pretreatment temperature 550℃ described as condition ④ in Table 1. Compared with condition ③, it seems that there is no obvious change about the yield judging from the SEM images of as-grown products (Figure 7a). However, according to the corresponding HRTEM images (Figure 7c-d), there are so many MWCNTs synthesized due to the aggregation of catalyst particles under higher temperature. In addition, we can see clearly from the higher magnification SEM image that there are so many particles within or on the tip of as-grown CNTs (Figure 7b) leading to the formation of different walled carbon nanotubes.

In conclusion, CCVD technique is not available for the synthesis of thin diameter SWCNTs with Fe_{18} clusters because of the inevitable aggregation of catalyst particles under high temperature during the pretreatment and CVD process. Although the pretreatment is very helpful and useful for the removal of functional groups to expose Fe_{18} clusters in order to increase the yield of CNTs, the amount of MWCNTs are so abundant within as-grown products leading to the inhomogeneous diameter distribution of as-grown CNTs. Therefore, mist flow CVD has been introduced.

4.3.3 Mist flow CVD

The mist flow CVD has been proved to be feasible and effective for the controllable growth of SWCNTs. In the case of choosing ethanol as the carbon source to dissolve Fe_{18} cluster, no matter what the CVD reaction is, there are no CNTs synthesized because we cannot detect any signals of CNTs on the substrate with Raman spectroscopy and find any CNTs under the TEM observation due to the large particle size measured in AFM images, which is unsuitable for the growth of CNTs. Nevertheless, it seems that methanol could be a favorite solvent for Fe_{18} cluster according to the relatively uniform particle size in AFM image. Therefore, several samples have been synthesized under the different CVD reaction conditions at first as shown in Table 2. This time, we put a copper TEM grid together with the Si substrate to collect the as-grown products directly for TEM observation. As a result, under 950℃ with the Ar/H_2 flow rate of 300 sccm (condition ①), for example, the as-grown products nearly consist of short MWCNTs according to the HRTEM images. Even though there is an individual SWCNT found with a thin diameter (0.7 nm), its quality is too bad and it is not typical (Figure 8). After that, no matter how to alter either the flow rate (down

to 100 sccm / up to 500 sccm) or the reaction temperature (down to 900℃ / up to 1000℃), the similar results have been obtained: short MWCNTs and atypical SWCNTs (Figure 9-12).

Table 2. Mist flow CVD conditions choosing methanol as the carbon source

Carrier gas	Temperature	Flow rate	Time
① Ar/H$_2$	950℃	300 sccm	15 min
② Ar/H$_2$	950℃	100 sccm	15 min
③ Ar/H$_2$	950℃	500 sccm	15 min
④ Ar/H$_2$	900℃	300 sccm	15 min
⑤ Ar/H$_2$	1000℃	300 sccm	15 min

The reason should be because of the larger particle size in methanol, it seems that the various combinations of experimental parameters cannot make the aggregated catalyst particles decomposed effectively and completely so that there are no suitable size of particles formed for the growth of SWCNTs, but MWCNTs. At the same time, the reason for the short length of as-grown MWCNTs is the lifetime of the involved catalyst particles is too short. Unlike the pretreatment process in CCVD technique, to expose the Fe$_{18}$ clusters and grow the CNTs occur simultaneously in the chamber during very short residence time so that it is insufficient to remove all the redundant functional groups to activate more catalyst particles.

Due to the smallest particle size, choosing MeCN as the carbon source has been investigated secondly. Because we want to elongate the time that the mist passed through the chamber (in order to remove the redundant functional groups) as much as possible, very low flow rate (50 sccm) has been tried at first (condition ① shown in Table 3), but unfortunately there are no CNTs synthesized. Then the flow rate has been raised to 100 sccm (condition ②). According to the lower magnification TEM image of

as-grown products shown in Figure 13 (a copper TEM grid is also put together with the Si substrate to collect the as-grown products directly for TEM observation), although the yield looks like not so high, SWCNTs have been synthesized successfully indeed.
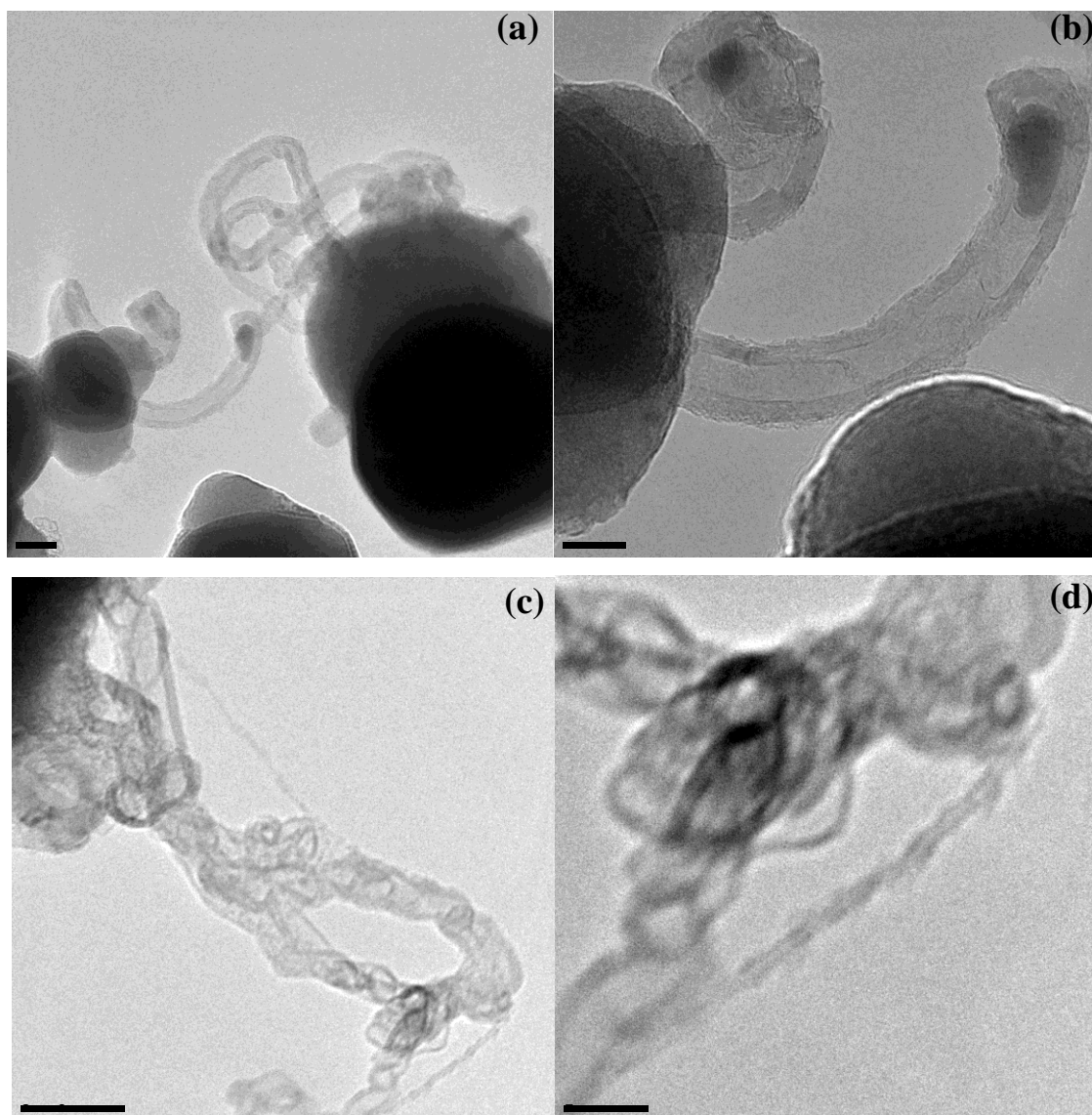

Figure 8. HRTEM images of (a-b) MWCNTs and (c-d) atypical SWCNTs of the sample synthesized under condition ①.

As shown in Figure 15, according to the measured diameter distribution of as-grown SWCNTs from at least 90 individual SWCNTs (Figure 14), it is explicit that

the mean diameter is just 0.81 nm, so close to the diameter of a single Fe_{18} cluster (0.65 nm) [31]. Perhaps thanks to the original solution to prepare Fe_{18} clusters, MeCN can display a good compatibility with Fe_{18} clusters, which could result in a better decomposition under the CVD reaction temperature.
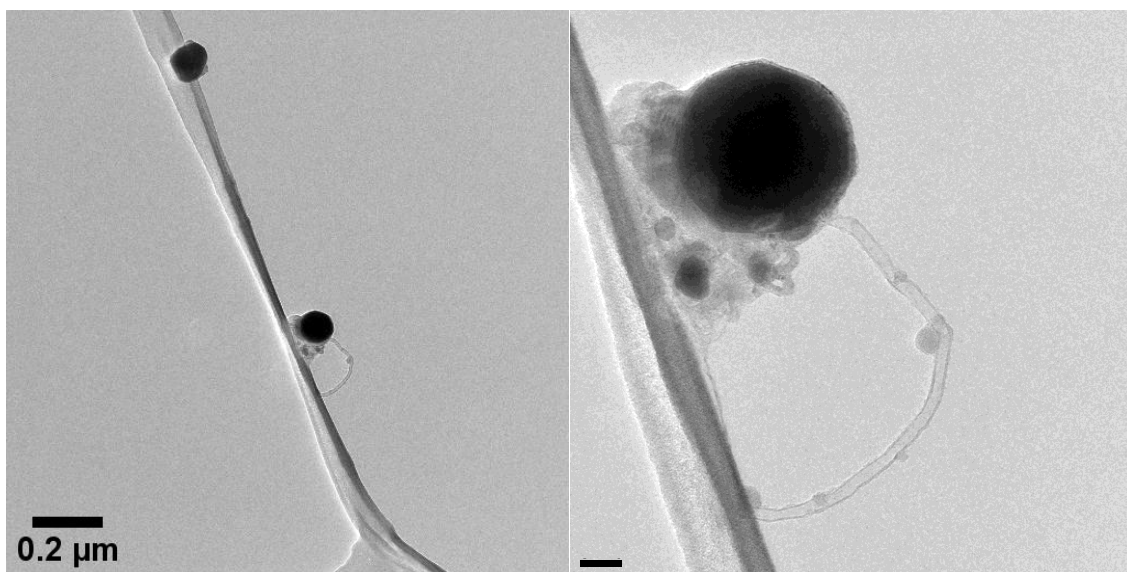

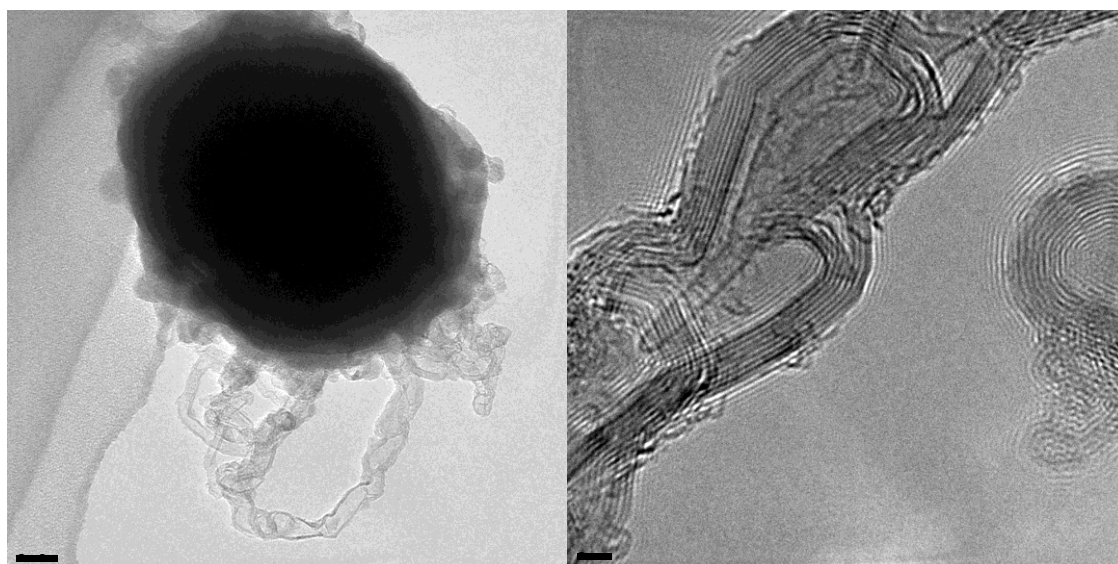Figure 9. HRTEM images of MWCNTs of the sample synthesized under condition ②.

Figure 10. HRTEM images of MWCNTs and there is an atypical SWCNT inside a MWCNT of the sample synthesized under condition ③.
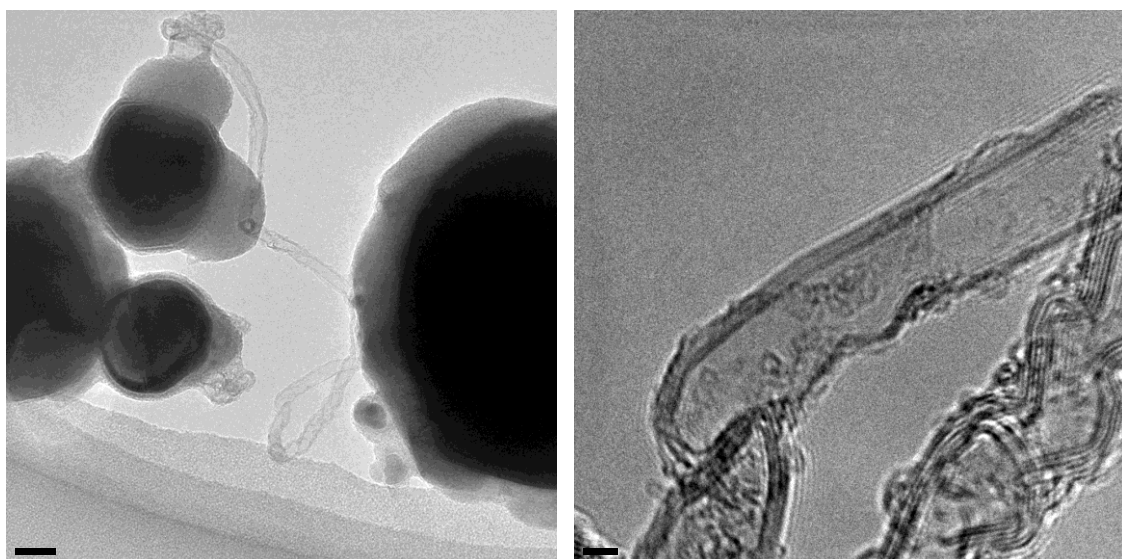
Figure 11. HRTEM images of MWCNTs of the sample synthesized under condition ④.
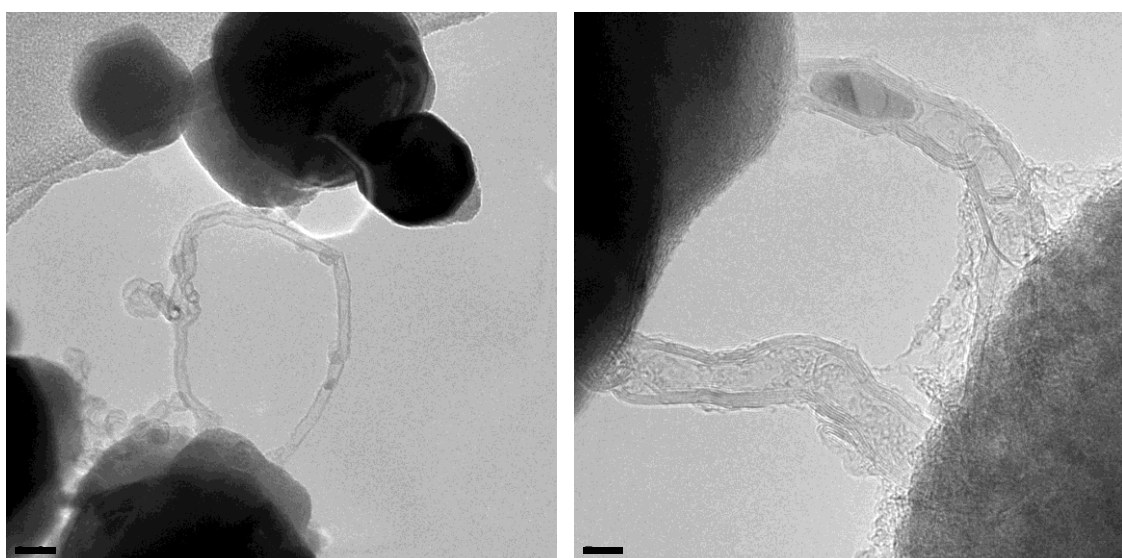

Figure 12. HRTEM images of MWCNTs of the sample synthesized under condition ⑤.

In addition, there could be a relationship between the particle size and the diameter of as-grown SWCNTs. As shown in Figure 16, on the tip of each individual SWCNT, a larger catalyst particle can lead to a bigger diameter tube; a single Fe_{18} cluster can lead to the growth of an individual SWCNT with diameter of 0.7 nm. Subsequently, the flow

rate has been raised to 150 sccm continuously (condition ③). As a result, according to the HRTEM images of the as-grown products (Figure 17a), it seems that there are no big differences of the diameter distribution compared with condition ②, but the mean diameter of as-grown SWCNTs has been decreased a little bit (0.77 nm in Figure 17b). However, when the flow rate is a little higher (300 sccm, condtion ④), there are no CNTs synthesized.

Table 3. Mist flow CVD conditions choosing MeCN as the carbon source

Carrier gas	Temperature	Flow rate	Time	CNTs Grown
①　Ar/H_2	950℃	50 sccm	15 min	
②　Ar/H_2	950℃	100 sccm	15 min	√
③　Ar/H_2	950℃	150 sccm	15 min	√
④　Ar/H_2	950℃	300 sccm	15 min	
⑤　Ar/H_2	900℃	100 sccm	15 min	√
⑥　Ar/H_2	1000℃	100 sccm	15 min	

As for the CVD reaction temperature, when it is decreased (900℃, condition ⑤), the mean diameter of as-grown SWCNTs is just a little bigger than that of 950℃ (0.91 nm) (Figure 18c). Indeed, there are several individual SWCNTs grown from a very larger particle (Figure 18a). According to T. Hayashi *et al*. [2], that is also the root of the tubes (top). DWCNTs have also been observed due to the aggregation of catalyst particles (Figure 18b). If we continue to increase the CVD reaction temperature to a higher one (1000℃, condition ⑥), there are no CNTs synthesized because the higher temperature can aggregate the Fe_{18} clusters to a larger one again, which are not available for the growth of CNTs.

As aforementioned in Chapter 1, PL is an important tool for the characterization of SWCNTs. Through scanning both the excitation and emission energies, thereby a PL
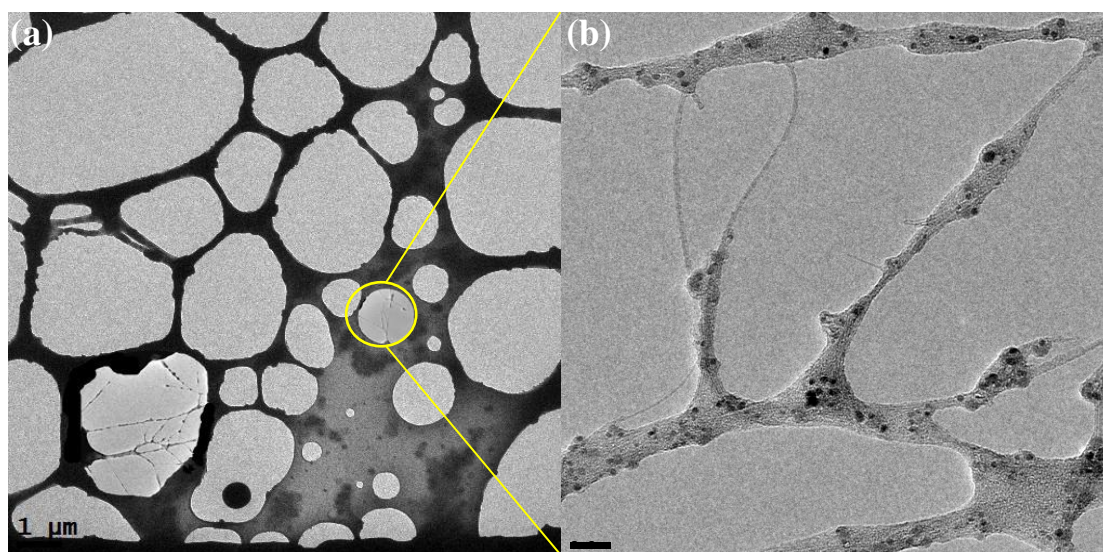
Figure 13. (a) Low magnification TEM image and (b) corresponding amplified one indicate the successful growth of SWCNTs.
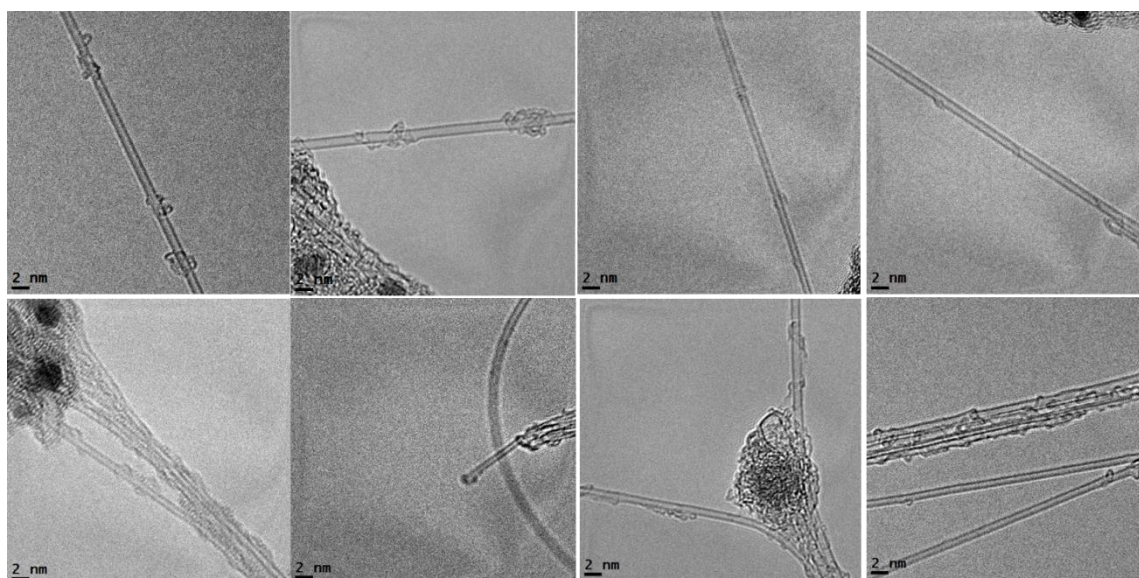

Figure 14. HRTEM images of several individual SWCNTs used for the measured diameter distribution synthesized under condition ②. The diameter is almost around 0.8 nm.

map is produced, from which the chiralities of SWCNTs in the sample can be deduced

as well as the diameter distribution. Figure 19 is the PL map of the as-grown products synthesized under condition ②. We can see that signals of (7, 5), (7, 6) and (8, 4) SWCNTs are the strongest indicating that the amount of SWCNTs with these three chiralities is abundant within the as-grown products. According to the Kataura plot, the
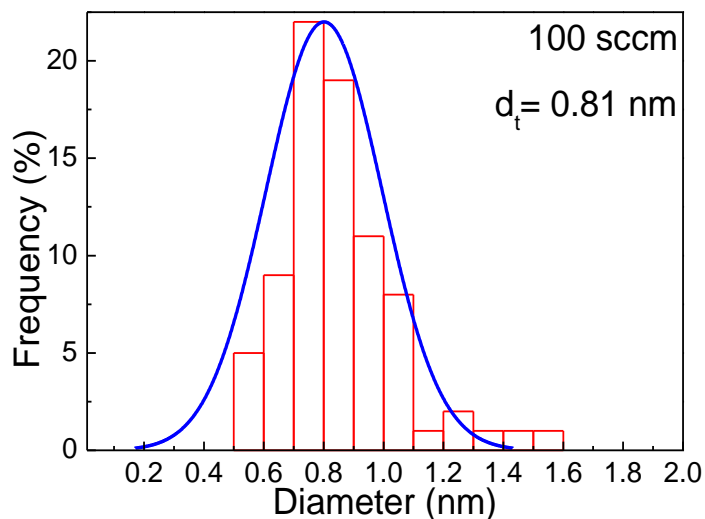

Figure 15. Corresponding measured diameter distribution of as-grown individual SWCNTs as shown in Figure 16.
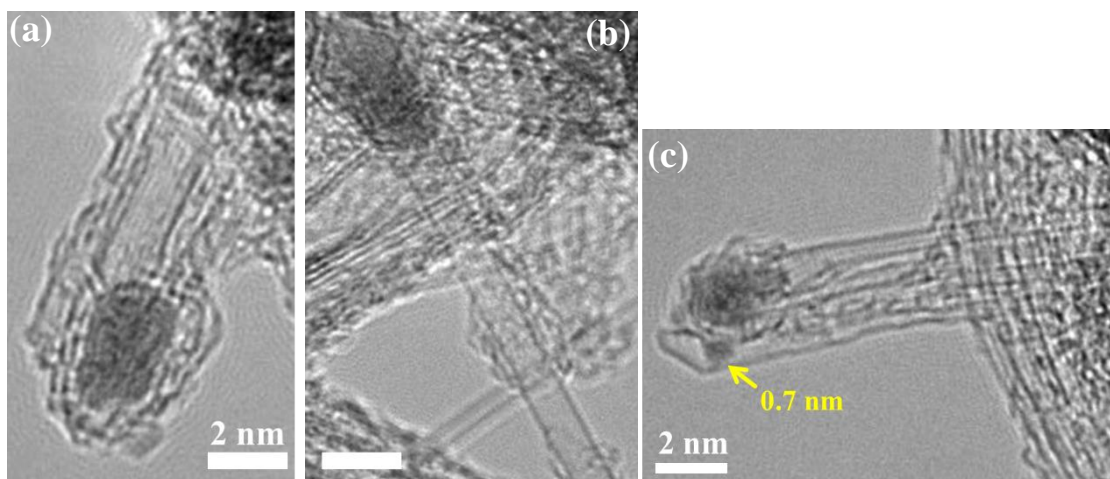

Figure 16. Several HRTEM images of the tip section of as-grown SWCNTs indicate there is a relationship between the particle size and the diameter of as-grown SWCNTs: (a-b) aggregated larger catalyst particles and (c) a single Fe_{18} particle lead to the growth of larger diameter and thin SWCNTs (0.7 nm), respectively.
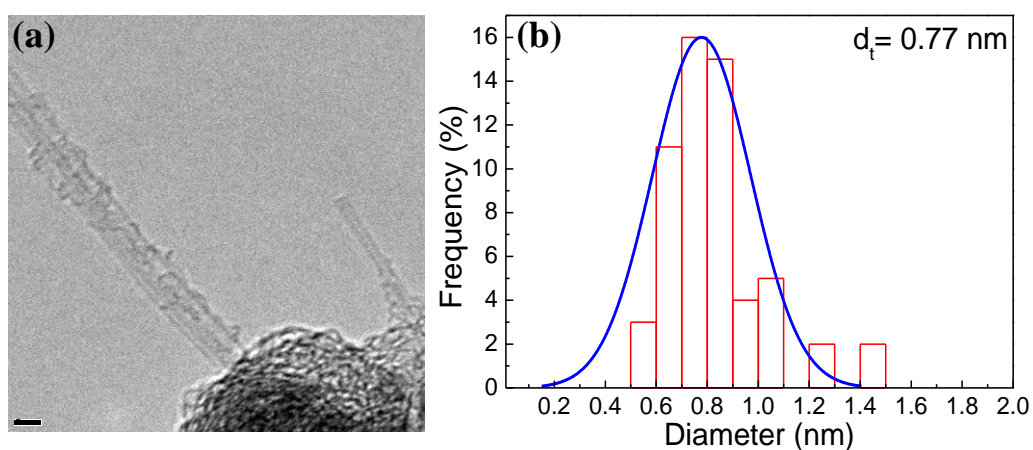
Figure 17. (a-b) HRTEM images and (c) the corresponding diameter distribution of as-grown products.
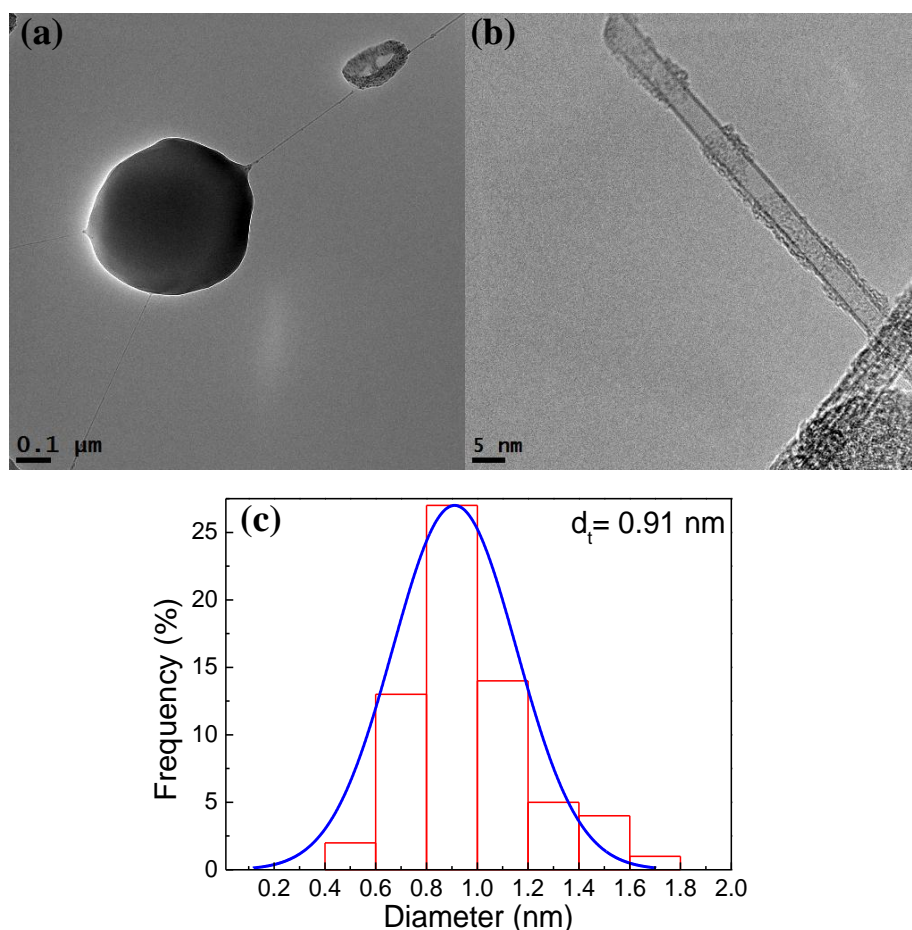

Figure 18. TEM images of as-grown products synthesized under condition ⑤: (a) several individual SWCNTs with a conjunct catalyst particle at the root; (b) HRTEM images of as-grown DWCNT; (c) corresponding diameter distribution of as-grown SWCNTs.

diameter of SWCNTs with these three chiralities is 0.83, 0.89 and 0.84 nm, respectively

so that the mean diameter of as-grown SWCNTs could be around 0.85 nm, which is

nearly consistent with the value from the measured diameter distribution in Figure 15

(the mean diameter is 0.81 nm) and prove the fact of the growth of thin SWCNTs.
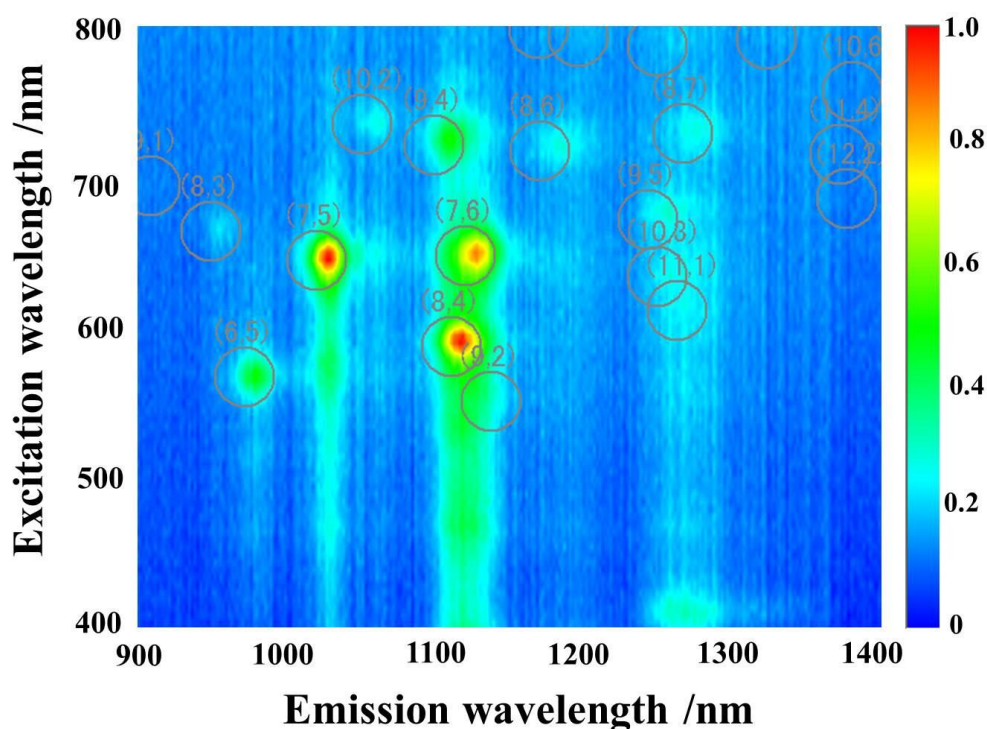
Figure 19. PL mapping of as-grown products synthesized under condition ②.

In my opinion, there could be another possibility about the reason why choosing

MeCN as the carbon source can lead to the growth of thin SWCNTs except the smallest

particle size. That should be the existence of N element. According to some studies [32],

nitrogen can mediate the growth of SWCNTs by acting as a surfactant leading to the

systems favoring smaller diameters. And as the N content increases, the diameter of

SWCNTs decreases and only narrow diameter tubes are formed because N tends to

prefer substitution into smaller tubes, independent of the tube chirality [33-35]. During

the mist flow CVD, nitrogen comes from the decomposition of MeCN. And this can also explain why the mean diameter of as-grown SWCNTs synthesized at the flow rate of 150 sccm is a little smaller (0.77 nm) than that synthesized at the flow rate of 100 sccm (0.81 nm). When the flow rate increased, the content of N will increases due to the increased amount of MeCN within the same residence time.

4.4 Conclusion

An investigation about the fabrication of thin SWCNTs from Fe_{18} clusters by means of mist flow CVD has been carried out. Due to its novelty, an endeavor to find out the favorite solvent (carbon source) for Fe_{18} cluster has been also implemented. As a result, in the case of the methanol selected as the carbon source to dissolve precipitated Fe_{18} crystals, only multi-walled carbon nanotubes (MWCNTs) are synthesized because of the larger particle size measured by atomic force microscopy (AFM). Alternatively, choosing the acetonitrile (MeCN), the original solvent for preparing Fe_{18} crystals, as the carbon source can lead to the mean diameter of as-grown SWCNTs (0.81 nm) considerably closed to the theoretical size of an individual Fe_{18} cluster (0.65 nm) because of the smallest particle size and the existence of N. At the same time, through the comparison with the catalysts-supported CVD (CCVD), we find that under the same reaction condition, the as-grown products consist of both MWCNTs and SWCNTs because of the serious aggregation during CVD, which prove that mist flow CVD is more effective for the synthesis of thin SWCNTs from Fe_{18} cluster providing another option for the fabrication of thin SWCNTs in a floating CVD system.

References

1. L. M. Peng *et al.*, Phys. ReV. Lett. 85, 3249 (2000).

2. T. Hayashi, Y. A. Kim, T. Matoba, M. Esaka, K. Nishimura, T. Tsukada, M. Endo, M. S. Dresselhaus, Nano Lett. 3, 887 (2003).

3. D. M. Sun, M. Y. Timmermans Y. Tian, A. G. Nasibulin, E. I. Kauppinen, S. Kishimoto, T. Mizutani, Y. Ohno, Nature Nanotechnol. 10, 1038 (2011).

4. Y. Miyata, K. Shiozawa, Y. Asada, Y. Ohno, R. Kitaura, T. Mizutani, H. Shinohara, Nano Res. 4, 963 (2011).

5. C. Dekker, S. J. Tans, A. R. M. Verschueren, Nature 393, 49 (1998).

6. K. Suzuki, Y. Ohno, S. Kishimoto, T. Mizutani, Appl. Phys. Express 6, 024002 (2013).

7. L. C. Qin et al., Nature (London) 408, 50 (2000).

8. A. Koshio, M. Yudasaka, S. Iijima, Chem. Phys. Lett. 356, 595 (2002).

9. N. Wang, Z. K. Tang, G. D. Li, J. S. Chen, Nature (London) 408, 50 (2000).

10. L. C. Qin, X. Zhao, K. Hirahara, Y. Ando, S. Iijima, Chem. Phys. Lett. 349, 389 (2001).

11. Y. F. Chan, H. Y. Peng, Z. K. Tang, N. Wang, Chem. Phys. Lett. 369, 541 (2003).

12. K. Hernadi et al., Zeolite 17, 416 (1996).

13. A. Fonseca et al., Appl. Phys. A 67, 11 (1998).

14. K. Mukhopadhyay, A. Koshio, N. Tanaka, H. Shinohara, Jpn. J. Appl. Phys. 37, 1257 (1998).

15. J. Kong, H. T. Soh, A. M. Cassell, C. F. Quate, H. Dai, Nature (London) 395, 878 (1998).

16. P. Ramesh, N. Kishi, T. Sugai, H. Shinohara, J. Phys. Chem. B 110, 130 (2006).

17. N. Kishi, S. Kikuchi, P. Ramesh, T. Sugai, Y. Watanabe, H. Shinohara, J. Phys. Chem. B 110, 24816 (2006).

18. P. Nikolaev, M. J. Bronikowski, R. K. Bradley, F. Rohmund, D. T. Colbert, K. A. Smith, R. E. Smalley, Chem. Phys. Lett. 313, 91 (1999).

19. H. M. Cheng, F. Li, G. Su, H. Y. Pan, L. L. He, X. Sun and M. S. Dresselhaus, Appl. Phys. Lett. 72, 3282 (1998).

20. H. Ago, S. Ohshima, K. Uchida and M. Yumura, J. Phys. Chem. B 105, 10453 (2001)

21. T. Saito, W. C. Xu, S. Ohshima, H. Ago, M. Yumura and S. Iijima, J. Phys. Chem. B 110, 5849 (2006).

22. T. Saito, S. Ohshima, W. C. Xu, H. Ago, M. Yumura and S. Iijima, J. Phys. Chem. B 109, 10647 (2005).

23. P. Nikolaev, M. J. Bronikowski, K. Bradley, F. Rohmund, D. T. Colbert, K. A. Smith and R. E. Smalley, Chem. Phys. Lett. 313, 91 (1999).

24. A. Moisala, A. G. Nasibulin, S. D. Shandakov, H. Jiang, L. Khriachtchev and E. I. Kauppinen, Chem. Eng. Sci. 61, 4393 (2006).

25. A. Moisala, A. G. Nasibulin, D. P. Brown, H. Jiang, L. Khriachtchev and E. I. Kauppinen, Carbon 43, 2006 (2005).

26. T. Hiraoka, S. Bandow, H. Shinohara and S. Iijima, Carbon 44, 1853 (2006).

27. G. Hong, Y. B. Chen, P. Li and J. Zhang, Carbon 50, 2067 (2012).

28. Y. Tian, M. Y. Timmermans, M. Partanen, A. G. Nasibulin, H. Jiang, Z. Zhu and E. I. Kauppinen, Carbon 49, 4636 (2011).

29. Y. Sun, R. Kitaura, T. Nakayama, Y. Miyata, H. Shinohara, NANO 7, 1250045 (2012).

30. P. King, T. C. Stamatatos, K. A. Abboud, G. Christou, Angew. Chem. Int. Ed. 45, 7379 (2006).

31. M. Böyükata, E. Borges, J. P. Braga, J. C. Belchior, J. Alloys. Comp. 403, 349 (2005).

32. B. G. Sumpter, V. Meunier, J. M. Romo-Herrera, E. Cruz-Silva, D. A. Cullen, H. Terrones, D. J. Smith, M. Terrones, ACS Nano 1, 369 (2007).

33. F. Villalpando-Paez, A. Zamudio, A. L. Elias, H. Son, E. B. Barros, S. G. Chou, Y. A. Kim, H. Mauramatsu, T. Hayashi, J. Kong *et al.*, Chem. Phys. Lett. 424, 345 (2006).

34. S. Trasobares, C. Stephan, C. Colliex, W. K. Hsu, H. W. Kroto, D. R. W. Walton, J. Chem. Phys. 116, 8966 (2002).

35. H. S. Ahn, S. C. Lee, S. Han, K. R. Lee, D. Y. Kim, Nanotechnology 17, 909 (2006).

Acknowledgement

I would like to express my gratitude to all those who helped me during the writing this thesis. First of all, my deepest and sincere gratitude would go foremost to Professor Hisanori Shinohara, my supervisor, for his guiding me into the field of nano science and continuous encouragement during my PhD career. I have been enveloped by his concern not only in my research work but also in my daily life, especially when I'm in trouble. I'll appreciate it so much. In addition, he has almost walked me through all the stages of the completing this thesis and the supervision of my PhD career. Without his consistent and illuminating instruction, I cannot complete my PhD career favorably and this thesis could not have reached its present form.

Secondly, I would also like to express my heartfelt gratitude to Associate Professor Ryo Kitaura (Nagoya University), another excellent scientist in our laboratory who had given me numerous valuable comments and academic guidance within these four years. After the each routine discussion with him, I can benefit a lot from his knowledge and experiences as a scientist. He is so patient for improving the level of my academic paper again and again. Thanks for your contribution and consideration to me.

Also I would like to thank Associate Professor Yasumitsu Miyata (Tokyo Metropolitan University, previously at Shinohara Lab of Nagoya University) for his help and instruction on Raman spectroscopy and absorption measurement. My gratitude also wants to be passed to Associate Professor Jinying Zhang (Xi'an Jiaotong University, previously at Shinohara Lab of Nagoya University) for her supplement of an aqueous

colloidal C_{60} solution.

In the end, my appreciations would go to my beloved family, my wife in particular, for their loving considerations, continuous encouragement and great confidence to me all through these years. I also owe my sincere gratitude to my friends and my fellow members in our laboratory who gave me their help and patience for helping me figure out my problems of both the research work and daily life within these four years.

Anyway, thank all of you so much!

List of Publications

I. Main Publications

1. "Controllable Chemical Vapor Deposition Growth of Single-Wall Carbon Nanotubes using Mist Flow Method"
<u>Yun Sun</u>, Ryo Kitaura, Takuya Nakayama, Yasumitsu Miyata, Hisanori Shinohara
NANO **7**, 1250045 (2012).

2. "Metal-Catalyst-Free Mist Flow Chemical Vapor Deposition Growth of Single-wall Carbon Nanotubes using C_{60} colloidal solutions"
<u>Yun Sun</u>, Ryo Kitaura, Jinying Zhang, Yasumitsu Miyata, Hisanori Shinohara
Carbon, revision submitted.

II. International Conferences

1. "A Novel Chemical Vapor Deposition Production of Carbon Nanotubes using Mist Flow Method" (**poster presentation**)
<u>Yun Sun</u>, Ryo Kitaura, Takuya Nakayama, Yasumitsu, Hisanori Shinohara
The 9th Joint Seminar between Münster University and Nagoya University, Nagoya, Japan (May 24-25, 2010)

2. "Selective Chemical Vapor Deposition Growth of Single-walled Carbon Nanotubes using C_{60} as the template by Mist Flow Method" (**poster presentation**)
<u>Yun Sun</u>, Ryo Kitaura, Jinying Zhang, Yasumitsu Miyata, Hisanori Shinohara
The 12th Joint Seminar between Münster University and Nagoya University, Nagoya, Japan (October 3-4, 2011)

3. "Controllable Chemical Vapor Deposition Growth of Single-Wall Carbon Nanotubes using Mist Flow Method" (**oral presentation**)
<u>Yun Sun</u>, Ryo Kitaura, Jinying Zhang, Yasumitsu Miyata, Hisanori Shinohara
Thirteenth International Conference on the Science and Application of Nanotubes (NT12), Brisbane, Australia (June 24-29, 2012)